Collective excitations of massive Dirac particles in a hot and dense medium

O. K. Kalashnikov[a) b)]
High-Energy Physics, ICTP, 34100 Trieste, Italy

(Submitted 13 October 1997; resubmitted 2 December 1997)
Pis'ma Zh. Éksp. Teor. Fiz. **67**, No. 1, 3–8 (10 January 1998)

The one-loop dispersion relation which defines the collective excitations of massive Dirac particles in a hot and dense quark–gluon medium is obtained in the high-temperature limit for the case $m \ll gT$ and is solved explicitly for all $|\mathbf{q}|$ when $\mu = 0$. Four well-separated spectrum branches (quasi-particle and quasi-hole excitations) are found, and their behaviors for small and large $|\mathbf{q}|$ are investigated. All calculations are performed using the temperature Green function technique and fixing the Feynman gauge. The gauge dependence of the spectra found is briefly discussed. © *1998 American Institute of Physics.*
[S0021-3640(98)00101-7]

PACS numbers: 12.38.Mh, 11.55.Fv, 02.30.Ks

INTRODUCTION

The study of collective excitations in a hot and dense medium is a topical problem in present-day physics, especially for chromodynamics. In a medium all the particles (fermions, as well as bosons) lose their individual properties, and, due to the multi-interaction with the heat bath and one another, collective excitations arise, which (unlike the ordinary vacuum physics at $T, \mu = 0$) have many new peculiarities: a gap of the order of gT at zero momentum, and a split spectrum at finite momentum.[1–5] These collective excitations determine the bulk of the kinetic and thermodynamic properties of the hot and dense medium and are very important for many processes taking place, for example, inside a hot quark–gluon plasma. Moreover, the quark–gluon medium (when μ and/or T are nonzero) generates new collective excitations of fermions: quasi-holes,[2,4] which are different from the quasi-particle excitations; their peculiarities (e.g., the minimum of the quasi-hole branches at finite momentum and the ''wrong'' relation between chirality and helicity) can produce new physical consequences. All these collective modes have nonzero effective masses, which arise dynamically independently of the bare masses and are not small for large parameters T, μ. In particular, for initially massive Dirac particles it has been established that there is a set of four effective masses,[6–8] which, in the general case, are well-separated and are always nonzero in the medium.

The goal of this paper is to present the one-loop dispersion relation which determines the collective excitations of massive Dirac particles in a hot and dense quark–gluon plasma in the high-temperature limit for the case $m \ll gT$, and to solve it explicitly for all $|\mathbf{q}|$ when $\mu = 0$. We use the standard temperature Green function technique and fix the Feynman gauge for explicit calculations. Only the case of zero damping is consid-

ered, and additional problems connected with the damping[5,9] are not discussed. Four well-separated spectrum branches are established, and their behavior for small and large $|\mathbf{q}|$ is investigated. The gauge dependence of the spectra found is briefly discussed. To start, we choose hot and dense QCD, although many results are model independent.

QCD LAGRANGIAN AND QUARK SELF-ENERGY

The QCD Lagrangian in covariant gauges has the form

$$\mathcal{L}=-\frac{1}{4}G^a_{\mu\nu}{}^2+N_f\bar{\psi}\left[\gamma_\mu\left(\partial_\mu-\frac{1}{2}ig\lambda^aV^a_\mu\right)+m\right]\psi-\mu N_f\bar{\psi}\gamma_4\psi+\frac{1}{2\alpha}(\partial_\mu V^a_\mu)^2$$
$$+\bar{C}^a(\partial_\mu\delta^{ab}+gf^{abc}V^c_\mu)\partial_\mu C^b, \tag{1}$$

where $G^a_{\mu\nu}=\partial_\mu V^a_\nu-\partial_\nu V^a_\mu+gf^{abc}V^b_\mu V^c_\nu$ is the Yang–Mills field strength; V_μ is a non-Abelian gauge field; ψ(and $\bar{\psi}$) are the quark fields in the SU(N) fundamental representation ($\frac{1}{2}\lambda^a$ are its generators and f^{abc} are the SU(N) structure constants), and C^a (and $\bar{C}^a$) are the ghost Fermi fields. In Eq. (1) μ and m are the quark chemical potential and the bare quark mass, respectively, N_f is the number of quark flavors, and α is the gauge-fixing parameter ($\alpha=1$ for the Feynman gauge). The metric is chosen to be Euclidean, and $\gamma^2_\mu=1$.

To find a non-perturbational representation for the temperature quark Green function, we start from the exact Schwinger–Dyson equation

$$G^{-1}(q)=G_0^{-1}(q)+\Sigma(q) \tag{2}$$

and calculate the quark self-energy, which in any gauge has the simple, well-known representation[10]

$$\Sigma(q)=\frac{N^2-1}{2N}\frac{g^2}{\beta}\sum_{p_4}^{F}\int\frac{d^3p}{(2\pi)^3}\mathcal{D}_{\mu\nu}(p-q)\gamma_\mu G(p)\Gamma_\nu(p,q|p-q). \tag{3}$$

In what follows we calculate $\Sigma(q)$ only in the one-loop approximation, using the bare Green functions in Eq. (3) and fixing the Feynman gauge (i.e., taking the appropriate $\mathcal{D}$ function). All ultraviolet divergences are renormalized as usual, but the infrared ones (which also arise in the high-temperature expansion when $m\ll gT$) will be eliminated phenomenologically.

At first the summation over the spinor indices is performed in Eq. (3) using the standard γ-matrix algebra

$$\Sigma(q)=\frac{N^2-1}{N}\frac{g^2}{\beta}\sum_{p_4}^{F}\int\frac{d^3p}{(2\pi)^3}\frac{i\gamma_\mu\hat{p}_\mu+2m}{(\hat{p}^2+m^2)(p-q)^2}, \tag{4}$$

and then the summation is performed over the Fermi frequencies $p_4=2\pi T(n+1/2)$ using the well-known prescription.[10] Here $\hat{p}=\{(p_4+i\mu),\mathbf{p}\}$ is a convenient abbreviation for vectors containing μ. All terms found are collected in a convenient form using simple algebraic transformations, and the final result is given by

$$\Sigma(q)=-\frac{g^2(N^2-1)}{N}\int\frac{d^3p}{2(2\pi)^3}\left\{\left[\frac{1}{\epsilon_{\mathbf{p}}}\frac{n^+_{\mathbf{p}}[\gamma_4\epsilon_{\mathbf{p}}+(i\boldsymbol{\gamma}\mathbf{p}+2m)]}{[q_4+i(\mu+\epsilon_{\mathbf{p}})]^2+(\mathbf{q}-\mathbf{p})^2}\right.\right.$$
$$\left.\left.+\frac{n^B_{\mathbf{p}}}{|\mathbf{p}|}\frac{(|\mathbf{p}|+\mu-iq_4)\gamma_4-[i\boldsymbol{\gamma}(\mathbf{q}-\mathbf{p})+2m]}{[q_4+i(\mu+|\mathbf{p}|)]^2+\epsilon^2_{\mathbf{p}-\mathbf{q}}}\right]-[\text{h.c.}(m,\mu)\rightarrow-(m,\mu)]\right\}, \tag{5}$$

where $\epsilon_{\mathbf{p}}=\sqrt{\mathbf{p}^2+m^2}$ is the bare quark self-energy; $n^B_{\mathbf{p}}=\{\exp\beta|\mathbf{p}|-1\}^{-1}$ and $n^{\pm}_{\mathbf{p}}=\{\exp\beta(\epsilon_{\mathbf{p}}\pm\mu)+1\}^{-1}$ are the Bose and Fermi occupation numbers, respectively.

Further, it is convenient to introduce two new functions and to rewrite Eq. (5) as

$$\Sigma(q)=i\gamma_\mu K_\mu(q)+mZ(q), \tag{6}$$

where $K_\mu(q)=q_\mu a(q)+iu_\mu b(q)$, and $u_\mu=\{1,0\}$ is the unit medium vector. All functions separately depend on q_4 and $|\mathbf{q}|$, as is usual in the medium case. Equation (6) presents the one-loop decomposition of $\Sigma(q)$, which, however, is not the most general here (see Ref. 11 for details), since a number of other functions are generated only in the multi-loop calculations. Using the decomposition (6), we transform Eq. (2) to the form

$$G(q)=\frac{-i\gamma_\mu(\hat{q}_\mu+K_\mu)+m(1+Z)}{(\hat{q}_\mu+K_\mu)^2+m^2(1+Z)^2}, \tag{7}$$

which gives the correct nonperturbational structure for this function. Setting the determinant of Eq. (7) to zero, we find the dispersion relation

$$(\hat{q}_\mu+K_\mu)^2+m^2(1+Z)^2=0, \tag{8}$$

which determines the collective excitation spectra after the analytical continuation.

COLLECTIVE EXCITATIONS IN THE HIGH-TEMPERATURE LIMIT

Here we use Eq. (8) to find the dispersion relation for the collective excitations of massive Dirac particles in a hot and dense quark–gluon plasma when $m\ll gT$. Different limits of this equation are discussed, and it is solved exactly for the massive fermion case with $\mu=0$. The spectrum branches are found for all $|\mathbf{q}|$ and their limits for small and large momenta are presented explicitly. Only the case of zero damping is considered, and for this reason our analytical continuation is trivial.

Our starting point is the dispersion relation (8)

$$[(iq_4-\mu)-\overline{K_4}]^2=\mathbf{q}^2(1+K)^2+m^2(1+Z)^2 \tag{9}$$

with $m\neq0$, and we use Eq. (5) to find its high-temperature expansion when $m\ll gT$. Here $K_4=i\overline{K_4}$, and we take into account only the leading terms in T^2, with the μ/T corrections according to Eq. (9). In this case all the functions which appear in Eq. (9) can be simplified as follows:

$$K(q_4,\mathbf{q})=\frac{I_K}{\mathbf{q}^2}\left(1+\frac{\xi}{2}\ln\frac{\xi-1}{\xi+1}\right)+I_B\left(\xi-\frac{1}{2}(1-\xi^2)\ln\frac{\xi-1}{\xi+1}\right), \tag{10}$$

$$-\overline{K}_4(q_4,\mathbf{q})=\frac{I_K}{2|\mathbf{q}|}\ln\frac{\xi-1}{\xi+1}+I_B,\quad -Z(q_4,\mathbf{q})=2I_Z+\frac{2I_B}{|\mathbf{q}|}\ln\frac{\xi-1}{\xi+1},\tag{11}$$

making it possible to solve Eq. (9) explicitly. Here $\xi=\omega/|\mathbf{q}|$ is a convenient variable, and the integrals are

$$I_K=\frac{g^2(N^2-1)}{N}\int_0^\infty\frac{d|\mathbf{p}|}{4\pi^2}|\mathbf{p}|\left[\frac{n_\mathbf{p}^+ + n_\mathbf{p}^-}{2}+n_\mathbf{p}^B\right],\tag{12}$$

$$I_B=-\frac{g^2(N^2-1)}{N}\int_0^\infty\frac{d|\mathbf{p}|}{8\pi^2}\frac{n_\mathbf{p}^+ - n_\mathbf{p}^-}{2},\tag{13}$$

$$I_Z=\frac{g^2(N^2-1)}{N}\int_0^\infty\frac{d|\mathbf{p}|}{8\pi^2}\frac{n_\mathbf{p}^+ + n_\mathbf{p}^-}{2\epsilon_\mathbf{p}}.\tag{14}$$

The integral I_Z, however, has been redefined to avoid the infrared divergences which arise after the high-temperature expansion is performed for $Z(q_4,|\mathbf{q}|)$:

$$Z(q)=-\frac{g^2(N^2-1)}{N}\int\frac{d^3p}{(2\pi)^3}\left\{\left[\frac{1}{\epsilon_\mathbf{p}}\frac{n_\mathbf{p}^+}{[q_4+i(\mu+\epsilon_\mathbf{p})]^2+(\mathbf{q}-\mathbf{p})^2}\right.\right.$$
$$\left.\left.-\frac{n_\mathbf{p}^B}{|\mathbf{p}|}\frac{1}{[q_4+i(\mu+|\mathbf{p}|)]^2+\epsilon_{\mathbf{p}-\mathbf{q}}^2}\right]+[\text{h.c.}(\mu\to-\mu)]\right\}.\tag{15}$$

The last expression is extracted from Eq. (5).

Now one should plug the expressions found above into Eq. (9) and perform a number of algebraic transformations to find $\omega=\xi|\mathbf{q}|$. Here $\omega=(iq_4-\mu)$. The result is an equation of the fourth degree with respect to $\omega(\xi)$:

$$\omega^4[\xi^2-(1+b(\xi)I_B)^2]+2\omega^3\xi^2I_B+\omega^2\xi^2[I_B^2-m_R^2+2d(\xi)I_K-2(1+b(\xi)I_B)$$
$$\times(1+d(\xi))I_K]+2\omega\xi^2d(\xi)I_B[I_K+4m_R^2]+I_K^2\xi^2[d(\xi)^2-\xi^2(1+d(\xi))^2]$$
$$-16m^2\xi^2d(\xi)^2I_B^2=0,\tag{16}$$

where $m_R=m(1-2I_Z)$ is the renormalized fermionic mass, and the functions $d(\xi)$ and $b(\xi)$ are given by

$$d(\xi)=\frac{\xi}{2}\ln\frac{\xi-1}{\xi+1};\quad b(\xi)=\xi-\frac{1}{2}(1-\xi^2)\ln\frac{\xi-1}{\xi+1}.\tag{17}$$

Since the dispersion relation obtained is very complicated, it is not solved exactly. However, in the long wavelength limit (when $\xi\to\infty$) it can be simplified as

$$[\omega^2+\omega(I_B-\eta m_R)-(I_K+4\eta mI_B)][\omega^2+\omega(I_B+\eta m_R)-(I_K-4\eta mI_B)]=0,\tag{18}$$

and one finds the rather simple solution[8]

$$\omega(0)=\frac{1}{2}(\eta m_R-I_B)\pm\sqrt{\frac{(\eta\, m_R-I_B)^2}{4}+(I_K+4\eta mI_B)},\tag{19}$$

which demonstrates four well-separated effective masses: two of them pertain to quasi-particle excitations and the other two to quasi-holes. Here $\eta=\pm 1$, and the parameters m and μ are nonzero.

The solutions for all $|\mathbf{q}|$ can be found within the framework of Eq. (16) if either m or μ is equal to zero. The case $m=0$ with $\mu\neq 0$ has been recently considered in detail, and the result has the form[8]

$$E(\xi)=\mu-\frac{\xi\, I_B}{2(\xi-\eta)}\pm\sqrt{\frac{\xi^2 I_B^2}{4(\xi-\eta)^2}+I_K\xi^2\left(\frac{\eta}{\xi-\eta}+\frac{\eta}{2}\ln\frac{\xi-1}{\xi+1}\right)}, \tag{20}$$

which extends the well-known result found in Refs. 2 and 3 to the case $\mu\neq 0$. Here we have restored the physical variable $E=ip_4$. The variable ξ runs over the range $1<\xi<\infty$, and the long-wavelength limit corresponds to $\xi\to\infty$. For this limit one finds the very simple result

$$E(0)=\mu-\frac{I_B}{2}\pm\sqrt{\frac{I_B^2}{4}+I_K}, \tag{21}$$

which can be compared with the interpolation formula in Ref. 12.

Another case in which Eq. (16) can be solved exactly for all $|\mathbf{q}|$ is for $m\neq 0$ but $\mu=0$. This case is the subject of the present paper and will be discussed below for $m\ll gT$. Now $I_B=0$, and within the adopted accuracy of the calculations the solution of Eq. (16) is found to be

$$\omega_{\pm}(\xi)^2=\frac{\xi^2(2I_K+m_R^2)}{2(\xi^2-1)}\pm\sqrt{\frac{\xi^4}{(\xi^2-1)^2}[(b(\xi)I_K)^2+m_R^2(I_K+m_R^2/4)]}. \tag{22}$$

These spectra are our main result. They present the collective excitations of massive Dirac particles in a hot medium for all $|\mathbf{q}|$ when $m\ll gT$. Two branches of the spectrum (when the plus sign is taken in Eq. (22)) correspond to quasi-particle excitations and the other two (when the minus sign is taken) to quasi-hole excitations. These spectrum branches differ in their asymptotic behavior and in many other properties.

The long-wavelength behavior of these spectra (when $\xi\to\infty$) has the form

$$\omega_{\pm}(|\mathbf{q}|)^2=M_{\pm}^2+\left(M_{\pm}^2\pm\frac{4}{9}\frac{I_K^2}{\sqrt{m_R^2(m_R^2+4I_K)}}\right)\frac{|\mathbf{q}|^2}{M_{\pm}^2}+O(|\mathbf{q}|^4) \tag{23}$$

where the squares of the effective masses are given by

$$M_{\pm}^2=\frac{m_R^2}{2}+I_K\pm\sqrt{m_R^2\left(\frac{m_R^2}{4}+I_K\right)}. \tag{24}$$

These masses are different for the four spectrum branches $M_{\pm}=\frac{1}{2}(\eta m_R\pm\sqrt{m_R^2+4I_K})$ and are in agreement with the results of Refs. 6 and 7. Here $\eta=\pm 1$.

However, this is not the case when the second term in Eq. (23) is taken into account. This term is not in agreement with the one obtained in Refs. 6 and 7. Although it agrees qualitatively with the result presented in Ref. 7, there is an essential difference with

Ref. 6, where a linear term was mistakenly found. It is also important that the quasi-hole spectra $\omega_-(|\mathbf{q}|)^2$ are very sensitive to the choice of the parameters m, T. In many cases these spectra are monotonic functions for small $|\mathbf{q}|^2$, and the well-known minimum[2] disappears. Although this minimum always exists for massless particles, special conditions are necessary to generate it when $m \neq 0$. In the high-momentum region the asymptotic behaviors found for the quasi-particle and quasi-hole excitations are completely different. The quasi-particle branches of the spectrum are approximated as

$$\omega_+(|\mathbf{q}|)^2 = |\mathbf{q}|^2 + (2I_K + m_R^2) - \frac{I_K^2}{|\mathbf{q}|^2} \ln \frac{4|\mathbf{q}|^2}{2I_K + m_R^2}, \tag{25}$$

where the nonanalytic term is not essential. The situation is different for the quasi-hole excitations, which do not exist in the vacuum (when T and μ are equal to zero). They disappear very rapidly, and their asymptotic behavior is found to be

$$\omega_-(|\mathbf{q}|)^2 = |\mathbf{q}|^2 + 4|\mathbf{q}|^2 \exp(-|\mathbf{q}|^2(2I_K + m_R^2)/I_K^2). \tag{26}$$

In the high-momentum region these spectrum branches approach the line $\omega^2 = |\mathbf{q}|^2$ more quickly than do the branches (25).

CONCLUSION

To summarize, we have obtained and solved the one-loop dispersion relation for massive fermions at finite temperature. Our solution gives the collective Fermi excitations for all $|\mathbf{q}|$, and we have established that they have four well-separated branches: two of them represent quasi-particle excitations, and the other two correspond to quasi-holes. The splitting found in the calculations demonstrates that the effective masses for all branches are different when $m \neq 0$, and these masses are always nonzero in the medium. The asymptotic behavior found for small $|\mathbf{q}|$ shows that the difference between the initially massive and massless fermions remains, although a dynamic mass is always generated and all their collective excitations are massive. For the massless fermions one finds that a spectral minimum always exists away from the point $|\mathbf{q}| = 0$, and the leading asymptotic term for small $|\mathbf{q}|$ is linear. However, this is not the case for initially massive fermions. When $m \neq 0$ the spectral minimum, as a rule, disappears as well as the linear term, and the term $|\mathbf{q}|^2$ gives the leading asymptotic behavior for small $|\mathbf{q}|$. The gauge invariance of the results found, unfortunately, is not proved, and there is no guarantee that this is indeed true. Here the situation is completely unclear, and the only known fact is that the dynamical mass for the case $m, \mu = 0$ is a gauge invariant object. All other quantities are gauge dependent, at least, within the one-loop calculations. Of course it is not ruled out that the Braaten–Pisarski resummation is necessary to improve the situation, but this question is not so evident as it is for the usual damping rate calculations.

I am grateful to S. Randjbar-Daemi for inviting me to the International Center for Theoretical Physics in Trieste, and I also thank the entire staff of this center for their kind hospitality.

[a)]e-mail: kalash@td.lpi.ac.ru
[b)]Permanent address: P. N. Lebedev Physics Institute, Russian Academy of Sciences, 117924 Moscow, Russia

[1] O. K. Kalashnikov and V. V. Klimov, Yad. Fiz. **31**, 1357 (1980) [Sov. J. Nucl. Phys. **31**, 699 (1980)].
[2] V. V. Klimov, Yad. Fiz. **33**, 1734 (1981) [Sov. J. Nucl. Phys. **33**, 934 (1981)];Zh. Eksp. Teor. Fiz. **82**, 336 (1982) [Sov. Phys. JETP **55**, 199 (1982)].
[3] H. A. Weldon, Phys. Rev. D **26**, 2789 (1982).
[4] O. K. Kalashnikov, Fortschr. Phys. **32**, 525 (1984).
[5] V. V. Lebedev and A. V. Smilga, Ann. Phys. (N.Y.) **202**, 229 (1990).
[6] R. D. Pisarski, Nucl. Phys. A **498**, 423 (1989).
[7] C. Quimbay and S. Vargas-Castrillon, Nucl. Phys. B **451**, 265 (1995).
[8] O. K. Kalashnikov, Mod. Phys. Lett. A **12**, 347 (1997).
[9] Jean-Paul Blaizot and E. Iancu, Phys. Rev. D **55**, 973 (1997).
[10] E. S. Fradkin, Tr. Fiz. Inst. Akad. Nauk SSSR **29**, 1 (1967).
[11] O. K. Kalashnikov, JETP Lett. **41**, 582 (1985).
[12] K. Kajantie and P. V. Ruuskaven, Phys. Lett. B **121**, 352 (1983).

Published in English in the original Russian journal. Edited by Steve Torstveit.

On the intrinsic quadrupole electric field of a centrosymmetric dielectric

D. N. Astrov, N. B. Ermakov, and S. V. Korostin
All-Russia Scientific-Research Institute of Physicotechnical and Radio Engineering Measurements, 141570 Mendeleevo, Moscow Region, Russia

(Submitted 14 November 1997)
Pis'ma Zh. Éksp. Teor. Fiz. **67**, No. 1, 15–20 (10 January 1998)

In agreement with a prediction of the theory, we have observed experimentally the intrinsic quadrupole electric field of a centrosymmetric crystal. © *1998 American Institute of Physics.*
[S0021-3640(98)00301-6]

PACS numbers: 77.84.Bw, 77.22.−d, 75.80.+q

We reported earlier the experimental observation[1] and study[2] of the intrinsic external quadrupole field of antiferromagnetic chromic oxide. These investigations were based on the theoretical work of Dzyaloshinskiĭ,[3] who showed that in order for a quadrupole magnetic moment to exist the magnetic symmetry of the crystal must be the same as that required for the existence of the magnetoelectric effect, which Cr_2O_3 exhibits. The decisive circumstance for the appearance of both properties was that the symmetry class of the crystal contain a symmetry element consisting of space inversion together with the time reversal operation.

If one is considering the purely electrical properties of crystals, specifically, the possibility of the existence of an intrinsic external quadrupole electric field, then the existence of a center of symmetry is sufficient for this, since time reversal does not affect the position of ions in a unit cell. Correspondingly, Dzyaloshinskiĭ noted in the same work[3] that noncubic crystals possessing a center of symmetry should possess an intrinsic external quadrupole electric field. According to his preliminary estimate, the intensity of this field is of the order of 1 V/cm.

We performed the investigations described below for the purpose of obtaining experimental proof of the existence of an intrinsic quadrupole electric field for a centrosymmetric crystal.

The main difficulty of observing the intrinsic electric field of a dielectric is due to the existence of free electric charges, which are always present both in the atmosphere surrounding the sample and on the surface of the sample and its holder. Under the influence of the intrinsic field of the sample the free charges will move so as to compensate this field, and the ultimate result of the process will be complete screening of the field. It is well known that the weak external electric fields of dielectrics can be observed only immediately after the crystal is brought through the phase transition point to a state with electrical polarization. After some time, the above-described process of screening of the field by the free charges makes it impossible to observe the polarization that arises.

Correspondingly, the requirement that a phase transition to a state with a center of

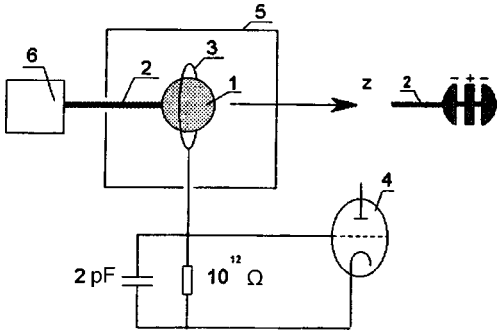

FIG. 1. Diagram of the apparatus.

symmetry be present must be imposed on the sample for our investigations. Furthermore, the chemical activity of the sample must be minimal in order to avoid ''attachment'' of free charges to the cleaned sample surface. Finally, the sample should not be too small.

We were not able to find a crystal satisfying all of the requirements listed above, the most important of which being the presence of a phase transition. However, there was still the hope that the quadrupole field in question can be observed if a nonequilibrium state is produced in the crystal and the external field of the crystal is followed during the relaxation to equilibrium. In this state, some unit cells located near vacancies, dislocations, and other distortions of the lattice of the nonequilibrium crystal will lose the center of symmetry and will not contribute to the quadrupole field of the sample. At the same time, these cells must possess a dipole polarization, but since they are distributed chaotically throughout the crystal, a macroscopic dipole field should not be observed. As the crystal relaxes to equilibrium, the number of distorted cells should decrease, the quadrupole field will increase, and there will not be enough time for the free charges to screen the increasing field completely. It is obvious that in this approach the observable part of the field of the sample will be several orders of magnitude weaker than the total field. Correspondingly, the instrumental sensitivity required to observe the unscreened part of the external field of the sample manifested during relaxation will increase sharply. The experimental difficulties that arise can be compensated to some degree by weakening the requirements on the lattice distortions in the sample as compared with the equilibrium case and by the possibility of using a chemically very stable sample with a large volume.

We knew from experience in fabricating and using low-pressure meters with a flexible sapphire element[4] that after being heated to 600–900 °C the elastic element of the device relaxes over many hundreds of hours. In the process, its geometry changes by as much as 0.01%. These data provided hope that we would be able to observe the quadrupole electric field of sapphire during its relaxation, as described above.

Figure 1 shows a diagram of the apparatus which we assembled for the purpose of observing the configuration of weak external fields of crystals. The experimental sample *1*, secured to the holder *2*, can move in the z direction and pass through a ring electrode *3*, which is 19 mm in diameter. The electrode is attached to the grid of an electrometric tube *4* of a U5-6 amplifier. The apparatus is surrounded by a grounded electrostatic shield

5. The holder *2* is secured to an electromagnetic vibrator *6* and oscillates in the z direction with a frequency of 10 Hz and an amplitude of ~ 0.5 mm.

The potential φ of the sample *1* periodically recharges the electrode *3* through a capacitance of the order of 0.02 pF between the sample and this electrode. Correspondingly, the voltage on the grid of the tube is proportional to $\partial\varphi/\partial z$, i.e., to the desired quantity, i.e., the field that is generated by the sample along the z axis. The signal at the output of the electrometric cascade was fed through an RC circuit to a selective amplifier and then to a synchronous detector that made it possible to determine the sign of the detected field.

The noise level on the electrode *3* ordinarily was equal to 20–40 μV, which corresponded to a current sensitivity of 3×10^{-17} A. The electrometer was calibrated together with the ac output amplifiers by applying a known voltage from a generator to the electrode *3* through a 50 pF capacitor with a leakage resistance of 10^{16} Ω.

We can see the advantage of this apparatus in that the data obtained describe the most characteristic features of the electric field of the sample. Specifically, the configuration of the field of a quadrupole whose axis is directed along the z direction will differ sharply from that of the field of an isolated charge or the field of a dipole.

The capability of the apparatus to detect an electric field with a configuration characteristic for a quadrupole was checked by means of a model inserted in the place of the sample *1*. The model is shown in the same Fig. 1 and consists of a set of metallic electrodes glued onto a ceramic holder. The dimensions of the model are virtually identical to those of our crystal samples whose intrinsic field we endeavored to detect. A small constant voltage was applied to the electrodes.

The apparatus was calibrated in a uniform electric field. The accuracy of the calibration is of the order of 5%. The sensitivity of the apparatus makes it possible to detect confidently an electric field of intensity less than 0.005 V/cm.

For the investigations we employed single-crystal sapphire samples possessing a rhombohedral structure with a center of symmetry. Dzyaloshinskiĭ estimates[a)] the quadrupole moment of sapphire to be positive and equal to 11.3 $\mathrm{V}\cdot\mathrm{cm}^3$ for a 1 cm^3 sample.

We had at our disposal three single-crystal samples: a cylinder 13 mm in diameter and 15 mm long, prepared from a high-quality crystal with no indications of block structure, and with the C_3 axis oriented along the axis of the cylinder; a sphere 13.5 mm in diameter; a tube 25 mm long and having an outer diameter of 10 mm and an inner diameter of 6 mm; it had clearly visible defects and its C_3 axis made an angle of 30° with the axis of the tube.

It was found that the results described below can be obtained only after the surface of the samples are carefully cleaned. The best method was found to be etching in carbon dioxide gas at 1700 °C for 0.5 h. This removed a layer several microns thick; in the process, the crystallographic reflection planes became clearly visible and the sample (sphere) could be oriented without difficulty with the C_3 axis along the z direction in the apparatus.

Samples with a cleaned surface were secured by means of prestressed fiberglass-reinforced cement to a holder — a ceramic tube 3 mm in diameter, consisting of sintered

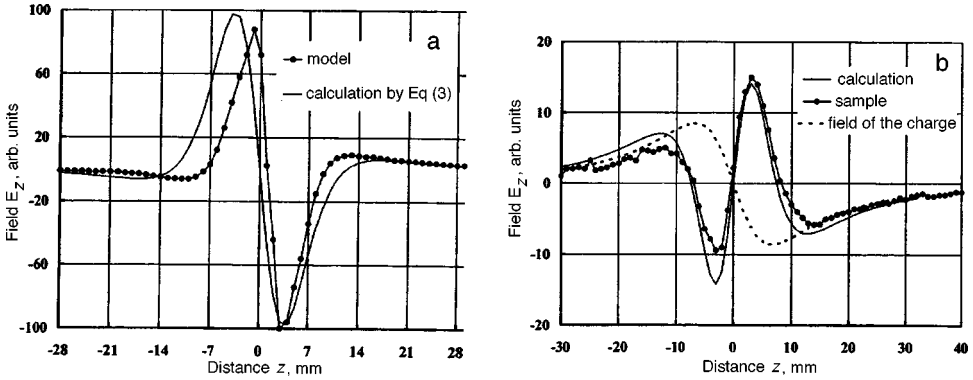

FIG. 2. Results of experiments with the model quadrupole (a) and the samples (b). See text for explanations.

Al_2O_3, whose thermal expansion coefficient is equal to that of sapphire and which crystallizes in air at 510 °C. Next, the holder with the sample was secured to the vibrator, and the sample was covered with a screen and brought into contact with the electrometric electrode.

It was found that after this procedure the sample always had the same (as a rule positive) charge, whose field reached an intensity of 10 V/cm. This charge vanished with a characteristic time of the order of 5 h, which, judging from the capacitance of the sample, corresponded to a reasonable leakage resistance $\sim 10^{16}$ Ω along the surface of the holder and through the surrounding air on account of its conductivity. The characteristic discharge time could vary by approximately a factor of 1.5 depending on the room humidity. The signal of interest to us could be observed after two days at the earliest.

We also determined that the characteristic time indicated above refers to the surface charge on the sample and is equal to the time associated with the flow onto the sample of the free charge that screens the electric field. For this purpose a model dipole consisting of two metal disks was introduced and secured inside the tubular sample. When a low dc voltage was applied to these disks, the characteristic dipole curve, with a field peak between the disks, arose immediately. During the next 5 h the amplitude of this peak dropped approximately by a factor of 3, and after 24 h the free charges that had flowed onto the sample had reduced the amplitude of the peak to the noise level of the experimental apparatus. After this, the voltage on the model dipole was switched off and the free charges which had flowed onto the sample were immediately manifested in the form of a peak with the same amplitude but with opposite sign as at the moment when the voltage was switched on. Once again this peak vanished over a characteristic time of about 5 h.

Figure 2b shows one of many characteristic experimental curves of the quadrupole field of the spherical sample. The left side of the curve is somewhat distorted by the holder. The quadrupole is positive, and this sign was always observed on all samples and at all stages of relaxation of the signal to zero.

The amplitude of the quadrupole field shown in Fig. 2b and measured three days after annealing equals about 0.1 V/cm and decreases in time, decaying by a factor of 3

over 50 h. This characteristic signal decay time for the spherical sample is approximately 2.5 times longer than for the cylindrical sample but approximately 4 times shorter than for the tubular sample. This ratio of the relaxation times for samples of different purity qualitatively corresponds to the proposed model, according to which the lattice cells that are distorted by neighboring defects re-establish the centrosymmetric structure, generating the quadrupole field, as the sample relaxes to equilibrium and the defects vanish. It is obvious that in a contaminated sample the number and height of energy barriers that must be overcome along the path to equilibrium are greater and correspondingly the relaxation time is also longer.

The dependence of the amplitude of the observed quadrupole field on the purity of the experimental samples also supports the proposed model. The amplitude is smallest for a high-purity cylindrical sample which relaxed more quickly and was closer to a state of equilibrium at the moment when observations were started. For the contaminated tubular sample the amplitude is approximately four times larger.

It should be noted that the source of the external quadrupole electric field of the sample is not only of volume origin. In principle, a surface layer of the sample, where the unit cells are distorted as a result of the proximity of the boundary, could be the source. In this layer the force fields acting on a cell are extremely asymmetric and the distortion of cell structure is also very large. Such cells lose their center of symmetry and should possess a substantial intrinsic dipole moment. It is obvious that these dipoles should be oppositely oriented relative to the C_3 axis, which is parallel to the z axis of the apparatus, at opposite ends of the sample.

As a result, an intrinsic quadrupole field of surface origin, and not volume origin, will arise in the sample, as should happen in the case analyzed by Dzyaloshinskiĭ. The number of distorted cells contributing to the quadrupole of surface origin is approximately 10^5 times smaller than the number of cells in a sample with a volume of the order of 1 cm^3, but their dipole moments are very large, especially for cells located in direct proximity to the surface. It is very difficult to estimate the strength of the quadrupole field of surface origin, even to within an order of magnitude, and it cannot be distinguished from a quadrupole of volume origin on the basis of symmetry considerations.

However, the field relaxation which we observed in all samples permits making the required choice. It is very likely that the experimentally observed quadrupole fields arise as a result of a relaxation of the crystal lattice to equilibrium, accompanied by a decrease in the number of lattice defects, together with a gradual screening of these fields by free charges. The quadrupole field of surface origin is also related with a lattice ''defect,'' which the surface itself is. It is obvious that this ''defect'' will always be present, and the effect of relaxation on the near-surface cells is all the weaker the stronger the distortion of these cells. For this reason, the quadrupole of surface origin cannot change appreciably in time and will be completely screened by surface charges.

For the reason indicated, we assume that the observed relaxing quadrupole field can be only of volume origin.

An additional confirmation of the fact that the field arising on the sample is of a purely quadrupole character was obtained by comparing with the well-known formula[5] for the potential of a quadrupole

$$\varphi = \frac{D}{4R^3}(3\cos^2\theta - 1), \tag{1}$$

where D is the quadrupole moment, R is the distance to the point of observation, and θ is the angle measured from the axis of the quadrupole. In the coordinates z and r, where z is the distance along the z axis from the center of the sample to the ring electrode of radius r, which are convenient for comparing with experiment, we have

$$\varphi = \frac{D}{4}(2z^2 - r^2)(z^2 + r^2)^{-5/2}. \tag{2}$$

Hence the component of the field along the z axis is

$$E_z = -\frac{\partial \varphi}{\partial z} = \frac{3}{4}Dz(2z^2 - 3r^2)(z^2 + r^2)^{-7/2}. \tag{3}$$

Figure 2a shows that this formula describes well the experimental curve for the quadrupole model at large distances. Hence it follows that, despite the small dimensions of the screens, our apparatus does not appreciably distort the observed field. A direct comparison of this formula with the experimental curves showed only qualitative agreement. Specifically, the measured amplitudes of the end peaks were much larger than implied by the formula, and the field decays away from the sample more slowly.

However, if one adheres to the same picture of the process, according to which the quadrupole field generated as the sample relaxes to equilibrium is screened with some delay by the free charges flowing onto the sample and the field of the charge is taken into account (Fig. 2b), then the agreement between the theoretical curve and the experimental data falls within the limits of the experimental accuracy. This is shown in Fig. 2b, which displays the experimentally measured field of the spherical sample and the computed curve obtained by superposing the field of a point quadrupole (3) and the field of the charge carried by the spherical sample. The arbitrary unit on the plot corresponds to 1 arb. unit $= -6.25\times10^{-3}$ V/cm, whence we obtain 0.22 $\mathrm{V}\cdot\mathrm{cm}^3$ for the quadrupole moment of our sample, which is 100 times smaller than the theoretical value. It is necessary to take into account the fact that the left sides of the experimental curves are distorted by the sample holder. It is interesting to note that even near the surface of the sample the experimental curve is described well by expression (3) for a point dipole.

We thank I. E. Dzyaloshinskiĭ for suggestions and a discussion of the results and E. A. Smirnov and Z. A. Magomedov for providing the samples for the investigations.

This work was supported by the Russian Fund for Fundamental Research (Grant 96-02-17264).

[a)]I. E. Dzyaloshinskiĭ, private communication (1997).

[1]D. N. Astrov and N. B. Ermakov, JETP Lett. **59**, 297 (1994).
[2]D. N. Astrov, A. S. Borovik-Romanov, N. B. Ermakov *et al.*, JETP Lett. **63**, 745 (1996).
[3]I. E. Dzyaloshinskii, Solid State Commun. **82**, 579 (1992).

[4] D. N. Astrov, L. B. Belyansky, Y. A. Dedikov *et al.*, Metrologia **26**, 151 (1989).
[5] L. D. Landau and E. M. Lifshitz, *The Classical Theory of Fields*, Pergamon Press, New York, 1975 [cited Russian original, Nauka, Moscow, 1988, Sec. 41].

Translated by M. E. Alferieff

Field theory of mesoscopic fluctuations in superconductor/normal-metal systems

A. Altland, B. D. Simons, and D. Taras-Semchuk
Cavendish Laboratory, Cambridge CB3 OHE, UK

(Submitted 20 November 1997)
Pis'ma Zh. Éksp. Teor. Fiz. **67**, No. 1, 21–26 (10 January 1998)

The thermodynamic and transport properties of normal disordered conductors are strongly influenced by the proximity of a superconductor. A cooperation between mesoscopic coherence and Andreev scattering of particles from the superconductor generates new types of interference phenomena. A field theoretic approach is introduced which is capable of exploring both the averaged properties and mesoscopic fluctuations of superconductor/normal-metal systems. As an example the method is applied to the study of the level statistics of a SNS junction. © *1998 American Institute of Physics.* [S0021-3640(98)00401-0]

PACS numbers: 74.50.+r, 74.25.Fy, 74.80.Fp, 73.23.−b

The physical properties of both superconductors and mesoscopic normal metals are governed by mechanisms of macroscopic quantum coherence. Their interplay in hybrid systems consisting of a superconductor adjacent to a normal metal gives rise to qualitatively new phenomena (see Ref. 1 for a review): aspects of the superconducting characteristics are imparted to the behavior of electrons in the normal region. This phenomenon, known as the ''proximity effect,'' manifests itself in: a) the *mean* (disorder-averaged) properties of SN systems being substantially different from those of normal metals, and b) various types of mesoscopic *fluctuations* which not only tend to be larger than in the pure N case but also can be of qualitatively different physical origin. Although powerful quasi-classical methods, based largely on the pioneering work of Eilenberger[2] and Usadel,[3] have been developed to analyze the manifestations of the proximity effect in average characteristics of SN systems, far less is known about the physics of mesoscopic fluctuations: while the quasi-classical approach is not tailored to an analysis of fluctuations, standard diagrammatic techniques[4] used in the study of N-mesoscopic fluctuations can often *not* be applied due to the essentially nonperturbative influence of the fully established proximity effect. Important progress was made recently by extending the scattering formulation of transport in N-mesoscopic systems to the SN case.[1] This approach has proven powerful in the study of various transport fluctuation phenomena but is not applicable to the study of fluctuations on a local and truly microscopic level.

In the present letter we introduce a general framework that combines key elements of the quasi-classical approach with more recent methods developed in N-mesoscopic physics into a unified approach. As a result we obtain a formalism that can be applied to the general analysis of mesoscopic fluctuations superimposed on a mean background influenced by the proximity effect. In order to demonstrate the practical use of the approach we will consider the example of *spectral fluctuations* as a typical representative

of a mesoscopic phenomenon. The density of states (DoS) of N-mesoscopic systems exhibits quantum fluctuations around its disorder-averaged mean value which can be described in terms of various types of universal statistics. The analogous question in the SN case — what types of statistics govern the disorder-induced fluctuation behavior of the *proximity-effect-influenced* DoS? — has not been answered so far. Our main result, the emergence of some kind of modified Wigner–Dyson statistics,[5] will be derived below.

To be specific we consider the geometry of a quasi-1D SNS junction, where the N region is of length L and the complex order parameters of the adjacent S regions differ in phase by φ. It is well known[6] that even the mean DoS of the SNS system exhibits nontrivial behavior which is difficult to describe within standard perturbation schemes: states which fall within the superconducting gap, Δ, are confined to the normal metal. The proximity effect then further induces a minigap in the DoS of the *normal* region around the Fermi energy, ϵ_F, whose size of $O(E_c = D_n/L^2)$ depends sensitively on φ (D_n is the diffusion constant, and $\hbar = 1$ throughout). To analyze the fluctuation behavior of the DoS, $\nu(\epsilon)$, around its disorder-averaged background, $\langle \nu(\epsilon) \rangle$, we will consider the two-point correlation function,[7] $R_2(\epsilon, \omega) = \langle \nu(\epsilon) \rangle^{-2} \langle \nu(\epsilon + \omega/2)\, \nu(\epsilon - \omega/2) \rangle_c$. The starting point of our analysis is the Gor'kov equation for the matrix advanced/retarded (a/r) Green function[2]

$$\mathcal{G}^{r,a}_{\epsilon} = \begin{pmatrix} G^{r,a}_{\epsilon} & F^{r,a}_{\epsilon} \\ F^{\dagger r,a}_{\epsilon} & G^{\dagger r,a}_{\epsilon} \end{pmatrix}, \tag{1}$$

where

$$\left[\epsilon_F - \frac{1}{2m} \left(\hat{p} - \frac{e}{c} \mathbf{A} \sigma_3^{ph} \right)^2 - V(\mathbf{r}) + (\hat{\Delta}(\mathbf{r}) + \epsilon_{\pm})\, \sigma_3^{ph} \right] \mathcal{G}^{r,a}_{\epsilon}(\mathbf{r}, \mathbf{r}') = \delta^d(\mathbf{r} - \mathbf{r}'), \tag{2}$$

$\epsilon_{\pm} \equiv \epsilon \pm i0$, $\mathbf{A}$ is the vector potential of an external magnetic field, $\hat{\Delta} = \Delta \sigma_1^{ph} \exp(-i\varphi \sigma_3^{ph})$ represents the (spatially dependent) complex order parameter with phase φ, and the Pauli matrices $\vec{\sigma}^{ph}$ operate in the Nambu or particle/hole (ph) space. The impurity potential in the N region is taken to be Gaussian δ-correlated with zero mean and correlation $\langle V(\mathbf{r}) V(\mathbf{r}') \rangle = \delta^d(\mathbf{r} - \mathbf{r}')/2\pi\nu\tau$, where ν denotes the DoS of the bulk normal metal at ϵ_F, and τ represents the mean free scattering time. In the following the complex order parameter in the S region is *imposed* and not obtained self-consistently.[8] Where the S and N regions are distinct (as in the SNS junction), the bulk DoS $\nu_{n,s}$ and scattering time $\tau_{n,s}$ will be chosen independently.

Traditionally the *impurity-averaged* Green function (1) is computed within a quasi-classical approximation, i.e., the Schrödinger equation (2) is reduced to an effective transport equation, the Eilenberger equation,[2] which in the dirty limit simplifies further to the diffusive Usadel equation.[3] Here we develop a field theoretic formulation that integrates concepts of the quasi-classical formalism into a more general framework allowing for the computation of disorder-averaged *products* of Green functions, a necessary requirement for the calculation of correlation functions such as R_2. The basic strategy will be to start from a (microscopically derived) generating functional whose points of sta-

tionary phase obey the Usadel equation. By investigating fluctuations around this quasiclassical limit, correlations between the different Green functions will be explored. In the following we formulate this program in more detail.

As in the pure N case, ensemble-averaged products of advanced and retarded Gor'kov Green functions can be described in terms of generating functionals of the nonlinear σ-model type[9] (see Ref. 10 for a review on the σ-model analysis of Green functions in N-mesoscopic physics). In the dirty limit, $(\epsilon,\Delta)<\tau^{-1}\ll\epsilon_F$, the generalization of the supersymmetric N-type σ model[10] reads

$$\int_{Q^2=} DQ(\cdots)e^{-S[Q]},$$

$$S[Q]=-\frac{\pi\nu}{8}\int \mathrm{str}\left[D(\tilde{\partial}Q)^2+4iQ\left(\tilde{\Delta}+\epsilon+\frac{\omega_+}{2}\sigma_3^{ar}\right)\sigma_3^{ph}\right], \tag{3}$$

where $\tilde{\partial}=\partial-i(e/c)[\mathbf{A}_{\phi}\sigma_3^{tr}\otimes\sigma_3^{ph},\cdot]$ represents a covariant derivative, $\mathbf{A}_{\phi}=\mathbf{A}+c/(2e)\partial\phi$ accounts for both the external field and the phase of the order parameter, $\tilde{\Delta}=\Delta\sigma_2^{ph}$, the Pauli matrices $\vec{\sigma}^{fb}$, $\vec{\sigma}^{tr}$, and $\vec{\sigma}^{ar}$ operate in fermion/boson, time-reversal, and ar-blocks respectively.[10] The symbol D stands for a space-dependent diffusion constant which may take separate values, denoted as $D_{n,s}$, in the N and S regions. Although specific pre-exponential source terms (denoted by ellipses in Eq. (3)) must be chosen according to some given correlation function (such as R_2), their precise form does not influence the analysis below and we therefore refer to Ref. 10 for their detailed structure. The integration in (3) extends over a 16×16-dimensional matrix field $Q=T^{-1}\sigma_3^{ph}\otimes\sigma_3^{ar}T$, whose symmetries are identical with those of the conventional σ model.[10]

The expression (3) differs in two respects from the σ model for N systems: i) the appearance of a ph-space associated with the 2×2-matrix structure of the Gor'kov Green function, and ii) the presence of the order parameter $\tilde{\Delta}$. Whereas i) can be accounted for by a doubling of the matrix dimension of the field Q, ii) calls for more substantial modifications: for $\Delta\neq0$ standard perturbation schemes for the evaluation of the functional (3) fail,[11] an indication of the fact that the superconductor influences the properties of the normal metal heavily. Under these conditions a more efficient approach is first to subject the action to a mean field analysis and then to consider fluctuations around a newly defined — and generally space-dependent — stationary field configuration. A variation of the action (3) with respect to Q, subject to the constraint $Q^2=$, generates a nonlinear equation for the saddle point,

$$D\tilde{\partial}_i(\overline{Q}\tilde{\partial}_i\overline{Q})+[\overline{Q},\Delta\sigma_1^{ph}-i(\epsilon+\omega_+\sigma_3^{ar})\sigma_3^{ph}]=0. \tag{4}$$

Current conservation implies the boundary condition,[12] $\sigma_n Q\partial_x|_{x_n}Q=\sigma_s Q\partial_x|_{x_s}Q$, where $\sigma_{n,s}=e^2\nu_{n,s}D_{n,s}$ denotes the conductivity and $\partial_x|_{x_{n(s)}}$ is a normal derivative at the N(S) side of the interface.

An inspection of (4) shows that only the particle/hole components of the matrix field $\overline{Q}$ are coupled by the saddle-point equation. It is thus sensible to make a block diagonal ansatz $\overline{Q}=\mathrm{bdiag}\,(q_+,q_-)$, where the eight dimensional retarded (q_+) and advanced

(q_-) subblocks are diagonal in both time-reversal and boson/fermion space. Noting that the saddle-point configuration $-i\pi\nu q_\pm$ of the nonlinear σ model is associated with the impurity-averaged retarded/advanced Green function,[10] we identify Eq. (4) as the Usadel equation. The general connection between the σ-model formalism and the quasi-classical approach was first noted in Ref. 13.

Equation (4), in its interpretation as the Usadel equation, has been discussed at length in the literature.[6,14,15] Although in general complex, the solutions have a simple qualitative geometric interpretation: with the explicit parametrization $q_\pm = \mathbf{q}_\pm \cdot \vec{\sigma}^{ph}$, Eq. (4) describes the gradual rotation of the three dimensional vector $\mathbf{q}$ from a direction almost parallel to $\hat{e}_1$ in the bulk superconductor to a direction aligned with $\hat{e}_3$ deep in the normal metal.

So far our analysis has been for SN systems of a general geometry. Specializing the discussion to the SNS junction, we set $\Delta(\mathbf{r}) \equiv \Delta\Theta(|x| - L/2)$ constant inside the superconductor ($\Delta \gg E_c$), and zero in the normal region, with a phase $\pi/2 + \mathrm{sgn}(x)\varphi/2$. The saddle-point equation depends sensitively on both the presence or absence of an external magnetic field and the phase difference between the order parameters. Taking the external field to be zero, it is convenient to focus on two extreme cases: (i) $\varphi = 0$ (orthogonal symmetry), and (ii) $\varphi \gg 1/\sqrt{g}$ (unitary symmetry). Here $g = E_c/\overline{d} \gg 1$ denotes the dimensionless conductance and $\overline{d}$ represents the bulk single-particle level spacing of the normal metal.

The *disorder-averaged local DoS* can be obtained from the analytical solution of the Usadel-saddle-point equation[6,14–17] as $\nu(\mathbf{r}) = \nu \mathrm{Re}[q_+(\mathbf{r})]_3$. The most striking feature of the average DoS is the appearance of a spatially constant minigap in the N region. The gap attains its maximum width E_c at $\varphi = 0$ and shrinks to 0 as φ approaches π (Ref. 15).

We next turn to the main subject of this letter, the issue of *fluctuations about the Usadel saddle point*. Employing the parametrization $Q = T^{-1}\overline{Q}T$, $T \neq$, one can identify three qualitatively different types of fluctuations: (a) fields T which are diagonal in the space of advanced and retarded components, (b) T's which commute with all matrices σ_i^{ph} but mix advanced and retarded components, and (c) T's fulfilling neither of the conditions (a) and (b). Fluctuations of the (a) type preserve the ar-diagonal structure of the saddle point. These fluctuations do not give rise to correlations between advanced and retarded Green functions. Nonetheless, they are of physical significance: Quantum corrections to the Usadel solution, most importantly the renormalization of the minigap by weak localization effects and the existence of rare prelocalized states[13,18] below the gap, are described by fluctuations of this type. We postpone further discussion of these results to a separate paper[17] and, instead, turn to a discussion of the second type of fluctuations, (b).

Consider the saddle-point equation (4) in the simple case $\omega = \varphi = 0$. Obviously, as it commutes with all matrices σ_i^{ph}, any spatially constant rotation T of type (b) gives rise to another solution. In other words, the (b) fluctuations represent Goldstone modes with an action that vanishes in the limit of spatial constancy and $\omega \to 0$. Since any T diagonal in ph-space inevitably has to couple between advanced and retarded indices,[10] these modes lead to *correlations between advanced and retarded Green functions* (and thereby

to mesoscopic fluctuations), which become progressively more pronounced as ω approaches zero.

In the limit of small frequencies $\omega < E_c$, the *ergodic regime*, the global zero mode $Q_0 = T_0^{-1} q T_0$, $[T_0, \vec{\sigma}^{ph}] = 0$, $T_0(\mathbf{r}) = \text{const}$, plays a unique role: whereas fluctuations with nonvanishing spatial dependence give rise to contributions to the action of $O(g \gg 1)$ (Ref. 10), this mode couples *only* to the frequency difference ω. Restricting attention to the pure zero-mode contribution, we obtain the effective action

$$S_0[Q_0] = -i \frac{\pi}{2} \frac{\omega_+}{\overline{d}(\epsilon)} \mathrm{str}[Q_0 \sigma_3^{ar}], \tag{5}$$

where $\overline{d}(\epsilon) = (\int \nu(\epsilon))^{-1}$ denotes the average level spacing and the ph-degrees of freedom have been traced out. From this result it follows[10] that, in the ergodic regime, the spectral statistics of an SNS system is governed by Wigner–Dyson fluctuations[5,19] of (i) orthogonal or (ii) unitary symmetry superimposed upon an energetically nonuniform mean DoS. Furthermore, a comparison of Eq. (5) with the analogous action for N systems[10] shows the correlations to depend on an average level spacing that is effectively *halved*. This reflects the strong ''hybridization'' of levels at energies $\sim \epsilon_F \pm \epsilon$ induced by Andreev scattering at the SN interface.

In further contrast to N systems, the range over which Wigner–Dyson statistics apply turns out to be greatly diminished by nonuniversal fluctuations Refs. 20 and 21. This is a consequence of the presence of fluctuations of type (c), coupling between advanced/retarded *and* particle/hole components. The detailed analysis of the (c)-type fluctuations is cumbersome and will be deferred to a forthcoming publication.[17] Here we only report that a perturbational integration over these modes leads to an exponential suppression of the DoS fluctuations already for energy separations $\omega/\overline{d}(\epsilon) \sim \sqrt{g}$. This is in contrast to the pure N case where the Wigner–Dyson regime (prevailing up to frequencies $\omega \simeq E_c$) is succeeded by other forms of *algebraically* decaying spectral statistics in the high-frequency domain $\omega > E_c$ (Ref. 22).

In conclusion, a general framework has been developed in which the interplay of mesoscopic quantum coherence phenomena and the proximity effect can be explored. An investigation of the spectral statistics of an SNS geometry revealed that level correlations are Wigner–Dyson distributed with strong nonuniversal corrections at large energy scales. Finally, we remark that for quantum structures in which transport is not diffusive but ballistic and boundary scattering is irregular, a ballistic σ model involving the classical Poisson bracket can be derived.[23] In this case, the saddle-point condition recovers the Eilenberger equation of transport.[2]

We are indebted to Anton Andreev, Dima Khmel'nitskii, and Martin Zirnbauer for helpful discussions. One of us (DT-S) acknowledges the financial support of the EPSRC. The hospitality of the ITP in Santa Barbara and the Lorentz Center in Leiden are gratefully acknowledged. This research was supported in part by the National Science Foundation under Grant PHY94-07194.

[1] C. W. J. Beenakker, Rev. Mod. Phys. **69**, 731 (1997).
[2] G. Eilenberger, Z. Phys. **182**, 427 (1965); *ibid*. **214**, 195 (1968).
[3] K. D. Usadel, Phys. Rev. Lett. **25**, 507 (1970).
[4] B. L. Altshuler and B. Z. Spivak, Zh. Éksp. Teor Fiz. **92**, 609 (1987) [Sov. Phys. JETP **65**, 343 (1987)].
[5] M. L. Mehta, *Random Matrices*, New York: Academic Press, 1991.
[6] For a review, see *Nonequilibrium Superconductivity*, Ed. V. L. Ginzburg, Nova Science Publications, 1988.
[7] $R_2(\epsilon,\omega)$ for the particular gapless ($\varphi=\pi$), zero-dimensional ($\omega<E_c$) case has been analyzed previously in A. Altland and M. R. Zirnbauer, Phys. Rev. Lett. **76**, 3420 (1996); K. M. Frahm, P. W. Brouwer, J. A. Melsen, and C. W. J. Beenakker, Phys. Rev. Lett. **76**, 2981 (1996).
[8] In general, the proximity of an N metal leads to a renormalization of the superconducting order parameter in the boundary region. However, we do not expect this phenomenon to have an essential impact on our results.
[9] R. Oppermann, Nucl. Phys. B **280**, 753 (1987).
[10] K. B. Efetov, *Supersymmetry in Disorder and Chaos*, New York: Cambridge University Press, 1997.
[11] For finite Δ, a perturbation expansion of $T=e^W$ in powers of W leads to contributions that are *linear* in W. These linear vertices generally have to be summed up to infinite order, which is difficult if not impossible.
[12] M. Yu. Kupriyanov and V. F. Lukichev, Zh. Éksp. Teor. Fiz. **94**, 139 (1988) [Sov. Phys. JETP **67**, 1163 (1988)].
[13] B. A. Muzykantskii and D. E. Khmel'nitskii, Phys. Rev. B **51**, 5840 (1995).
[14] W. Belzig, C. Bruder, and G. Schoen, Phys. Rev. B **54**, 9443 (1996).
[15] F. Zhou, P. Charlat, B. Spivak, and B. Pannetier, http://xxx.lanl.gov/abs/cond-mat/9707056.
[16] Note that the solution of Eq. (4) does not in general belong to the standard saddle-point manifold of the σ model. It can, however, be accessed by a deformation of the integration contour.[17]
[17] A. Altland, B. D. Simons, and D. Taras-Semchuk, to be published.
[18] V. I. Fal'ko and K. B. Efetov, Europhys. Lett. **32**, 627 (1995); A. D. Mirlin, Phys. Rev. B **53**, 1186 (1996).
[19] With reference to the specific correlation function R_2, we remark that only massive fluctuations in the ph-sector contribute to connected correlators of the form $\langle \mathcal{G}^A_{\epsilon_1}\mathcal{G}^A_{\epsilon_2}\rangle$, allowing such terms to be neglected.
[20] V. E. Kravtsov and A. D. Mirlin, JETP Lett. **60**, 656 (1994).
[21] B. D. Simons and B. L. Altshuler, Phys. Rev. Lett. **70**, 4063 (1993).
[22] B. L. Altshuler and B. I. Shklovskii, Zh. Éksp. Teor. Fiz. **91**, 220 (1986) [Sov. Phys. JETP **64**, 127 (1986)].
[23] B. A. Muzykantskii and D. E. Khmel'nitskii, JETP Lett. **62**, 76 (1995); A. V. Andreev, O. Agam, B. D. Simons, and B. L. Altshuler, Phys. Rev. Lett. **76**, 3947 (1996).

Published in English in the original Russian journal. Edited by Steve Torstveit.

Quantum tunneling in ferromagnetic nanoparticles interacting with a spin thermostat: effective Hamiltonian

I. S. Tupitsyn
Kurchatov Institute Russian Science Center, 123182 Moscow, Russia

(Submitted 25 November 1997)
Pis'ma Zh. Éksp. Teor. Fiz. **67**, No. 1, 27–32 (10 January 1998)

An effective Hamiltonian is obtained which describes quantum tunneling in ferromagnetic nanoparticles in the presence of a hyperfine interaction of the electron spins in the nanoparticle with the microscopic spins in the environment (such as paramagnetic impurities or nuclear spins). A criterion of transition between ferromagnetic and antiferromagnetic tunneling regimes is found. The validity of the equations obtained is checked by the method of exact diagonalization. © *1998 American Institute of Physics.* [S0021-3640(98)00501-5]

PACS numbers: 61.46.+w, 75.50.Tt, 75.10.Jm

1. The phenomenon of quantum tunneling of magnetization (or the Néel vector) in nanoparticles has been attracting increasing attention in recent years from both the experimental and theoretical viewpoints, since this purely quantum effect appears on macroscopic scales of the total number of spins of the order of 10^4 and more. The electronic spins of the nanoparticles are exchange-paired with one another, forming either a ''giant central spin'' — in the ferromagnetic case — or a ''giant Néel vector'' — in the antiferromagnetic case, and they can tunnel coherently between two degenerate states separated by a barrier due to the presence of magnetic anisotropy. The theory of coherent tunneling of the magnetization vector is expounded in a number of papers[1] (for a more complete review see Ref. 2 and the literature cited therein). The tunneling effect in antiferromagnetic particles should be even stronger than in ferromagnetic particles[3] (for a review of the current status of the theory and experiment see, respectively, Refs. 3–9 and Ref. 10). It is found that in both cases the hyperfine interaction of the electronic spins of the particles with a spin thermostat, consisting of nuclear spins or paramagnetic impurities, plays an extremely role in both cases.[11,12] This interaction is so strong that it can suppress quantum coherence completely.[13] Coherence suppression in the process of tunneling can be analyzed theoretically by introducing an *effective Hamiltonian* describing the *low-energy* dynamics of the system ''giant spin'' (or ''giant Néel vector'') + the spin thermostat. This means that the experimental energy range is limited to the region $\ll\Omega_0$, where Ω_0 characterizes the gap between the bottom doublet and the excited energy levels, and the Hilbert space of the problem is bounded by the bottom doublet, corresponding to the opposite spatial orientations of the order parameter. Such an effective Hamiltonian for the ''giant spin'' was obtained with the aid of the instanton technique in my previous work.[14] In the present letter a similar effective Hamiltonian will be obtained for the case of a *ferrimagnetic/antiferromagnetic nanoparticle.* The validity of the analytical expression obtained will be checked by exact diagonalization.

2. Using the well-known fact that the Heisenberg model with antiferromagnetic ordering can be reduced in the long-wavelength limit to the nonlinear $O(3)$ σ model (in both the one- and two-dimensional cases),[4,5,7,9,15] we introduce an effective two-sublattice model with a strong exchange interaction between the magnetizations of the sublattices. The Lagrangian of the model will be similar to the Lagrangian of the $O(3)$ σ model (see, for example, Refs. 3, 4, and 8). But, in contrast to the papers mentioned, we shall add the hyperfine interaction of the sublattice spins $\mathbf{S}_1$ and $\mathbf{S}_2$ with the spins in the environment ($|\vec{\sigma}_i|=\frac{1}{2}$) in a weak magnetic field $\mathbf{H}_0$ (We neglect the interaction of the spins in the environment with one another). Since the spins in the environment can be located either inside the particle itself or near it (on the substrate), without loss of generality we shall assume that only one paramagnetic impurity is present and that it is located in the first sublattice. Then, assuming the magnetic anisotropy to be of the *easy axis/easy plane* type, we write the starting Hamiltonian in the form

$$\hat{H}=J\mathbf{S}_1\cdot\mathbf{S}_2+U(\mathbf{S}_1)+U(\mathbf{S}_2)+\frac{\omega_0}{2S_1}\mathbf{S}_1\cdot\vec{\sigma},\quad U(\mathbf{S})=-K_{\|}S_z^2+K_{\perp}S_y^2-\gamma_e\mathbf{H}_0\cdot\mathbf{S},\quad (1)$$

where ω_0 is the hyperfine interaction constant, $K_{\|}>0$ and $K_{\perp}>0$ are the magnetic anisotropy constants, $J\gg K_{\|}$, $K_{\perp}\gg K_{\|}$, $\gamma_e S_{1,2}|\mathbf{H}_0|\ll 2K_{\|}S_{1,2}^2$, and $\omega_0\ll 2K_{\|}S_{1,2}^2$. Assuming $S_1+S_2\gg 1$, we choose the *quasiclassical* description for the solution.

In accordance with the fact that we are interested only in the low-energy dynamics of the system, only trajectories with *almost antiparallel* (i.e., weakly fluctuating in direction relative to one another) $\mathbf{S}_1$ and $\mathbf{S}_2$ will contribute to the transition amplitude between the two lower energy levels. This means that an *almost* constant Néel vector $\mathbf{N}=\mathbf{S}_1-\mathbf{S}_2$ will tunnel. In addition, since we assume that $S_1\neq S_2$ in the general case, the uncompensated spin $S=S_1-S_2$ will tunnel in a correlated fashion with the Néel vector.

We now introduce the spherical angles θ_1, θ_2, ϕ_1, and ϕ_2, which fix the directions of $\mathbf{S}_1$ and $\mathbf{S}_2$. In accordance with what has been said above, we set $\theta_2=\pi-\theta_1-\epsilon_\theta$ and $\phi_2=\pi+\phi_1+\epsilon_\phi$ (for $|\epsilon_\theta|$, $|\epsilon_\phi|\ll 1$) (see Ref. 3). We choose as a basis the states characterized by opposite directions of the Néel vector (along the easy axis **z**) $|\Downarrow\rangle$ and $|\Uparrow\rangle$. Then the transition amplitude can be written as an integral over trajectories:

$$\Gamma_{\alpha\beta}(t)=\int_\beta^\alpha \mathcal{D}\{\theta_1,\theta_2,\phi_1,\phi_2\}\exp\left\{-\int_0^t d\tau[\mathcal{L}_0(\tau)+\delta\mathcal{L}_H(\tau)+\delta\mathcal{L}_\sigma(\tau)]\right\},\quad (2)$$

where $\mathcal{L}_0(\tau)$, $\delta\mathcal{L}_H(\tau)$, and $\delta\mathcal{L}_\sigma(\tau)$ are taken in the Euclidean form and α, $\beta=|\Downarrow\rangle,|\Uparrow\rangle$.

3. Let us now find the extremal trajectory for $\theta_1(\tau)$ and $\phi_1(\tau)$ with no field and no interaction with an impurity (this is the trajectory that will be needed below, since we shall assume that $|\mathbf{H}_0|$ and ω_0 are small). The Lagrangian $\mathcal{L}_0$ has the following form:

$$\mathcal{L}_0=JS_1S_2(\sin\theta_1\sin\theta_2\cos(\phi_1-\phi_2)+\cos\theta_1\cos\theta_2+1)+\mathcal{L}_{\mathbf{S}_1}^0+\mathcal{L}_{\mathbf{S}_2}^0,$$

$$\mathcal{L}_{\mathbf{S}}^0=-iS\phi\dot{\theta}\sin\theta+K_{\|}S^2\sin^2\theta+K_{\perp}S^2\sin^2\theta\sin^2\phi.\quad (3)$$

Since the **y** axis is the ''heavy'' axis, ϕ will fluctuate weakly around $\phi=0$ or $\phi=\pi$. These values of ϕ correspond to two possible trajectories — clockwise or counterclockwise — connecting two quasiclassical minima. The result of the Gaussian integration

over the three fast variables (ϵ_θ, ϵ_ϕ, ϕ) is (all terms that do not contribute to the equation of motion are dropped and the indices for θ and ϕ are dropped)

$$\mathcal{L}_0(\theta)=\frac{\mathcal{M}}{2}\,\dot\theta^2+\frac{S_2^2}{2\widetilde{J}}\,\dot\phi^2\,\sin^2\,\theta+\widetilde{K}_\parallel\sin^2\,\theta,\quad \widetilde{z}=\widetilde{K}_\perp-\frac{2K_\perp^2S_2^4}{\widetilde{J}+2K_\perp S_2^2},$$

$$\mathcal{M}=\frac{S^2}{2\widetilde{z}}+\frac{2SS_2^3K_\perp}{\widetilde{z}(\widetilde{J}+2K_\perp S_2^2)}+\frac{S_2^2}{\widetilde{J}+2K_\perp S_2^2}+\frac{2S_2^6K_\perp^2}{\widetilde{z}(\widetilde{J}+2K_\perp S_2^2)^2},\tag{4}$$

where $\widetilde{K}_{\perp,\parallel}=K_{\perp,\parallel}(S_1^2+S_2^2)$ and $\widetilde{J}=JS_1S_2$. This Lagrangian gives the quasiclassical equations of motion: $\dot\phi=0$ and $\dot\theta=\Omega_0\sin\theta$. Their solution is

$$\phi=\text{const},\quad \sin\,\theta(\tau)=1/\cosh(\Omega_0\tau),\quad \Omega_0=(2\widetilde{K}_\parallel/\mathcal{M})^{1/2}.\tag{5}$$

Substituting the extremal trajectory into $\mathcal{L}_0$ and integrating over τ gives for the Euclidean action

$$A_0^\eta=A_0+i\,\eta\pi S,\quad A_0=4\widetilde{K}_\parallel/\Omega_0,\tag{6}$$

where $\eta=\pm$ correspond to clockwise and counterclockwise motion between the quasiclassical minima and $\eta\pi S$ is the Kramers–Haldane phase.

4. We now introduce a weak magnetic field ($\gamma_e=1$):

$$\delta\mathcal{L}_H=\delta\mathcal{L}_{\mathbf{S}_1}^H+\delta\mathcal{L}_{\mathbf{S}_2}^H,\quad \delta\mathcal{L}_{\mathbf{S}}^H=-S(H_0^x\sin\,\theta\cos\,\phi+H_0^y\sin\,\theta\sin\,\phi+H_0^z\cos\,\theta).\tag{7}$$

Integrating $\mathcal{L}_0+\delta\mathcal{L}_H$ over ϵ_θ and ϵ_ϕ, setting $S_1=S_2$, and passing to the limit $J\gg K_\perp$ yield the well-known expression for the Andreev–Marchenko Lagrangian[16] without a gradient term and the term describing weak Dzyaloshinskiĭ ferromagnetism. But now we continue in general form. Having integrated (7) over all three fast variables (retaining only the terms linear in the field), we substitute the extremal trajectory (5) and after integrating over τ, we obtain a correction to the action (6)

$$\delta A_H^\eta=-i\,\frac{\eta\pi S_2^2H_y}{\widetilde{J}+2K_\perp S_2^2}\left\{1+\frac{2K_\perp^2S_2^4}{\widetilde{z}(\widetilde{J}+2K_\perp S_2^2)}\right\}-\frac{\eta\pi H_x}{\Omega_0}\left\{\frac{K_\parallel S_2^3}{\widetilde{J}}+\frac{K_\perp S_2^5\Omega_0^2}{\widetilde{z}(\widetilde{J}+2K_\perp S_2^2)^2}\right\}$$
$$-\frac{\eta\pi S}{\Omega_0}\left\{H_x+i\,\frac{S\Omega_0}{2\widetilde{z}}H_y\right\}-\frac{\eta\pi S\Omega_0S_2^2}{2\widetilde{z}(\widetilde{J}+2K_\perp S_2^2)}\left\{H_x+i\,\frac{4K_\perp S_2}{\Omega_0}H_y\right\}.\tag{8}$$

5. The correction to the Lagrangian $\mathcal{L}_0$ as a result of the hyperfine interaction with nuclear spin can be represented in the form

$$\delta\mathcal{L}_\sigma=\frac{\omega_0}{2}(\hat\sigma_x\sin\,\theta_1\cos\,\phi_1+\hat\sigma_y\sin\,\theta_1\sin\,\phi_1+\hat\sigma_z\cos\,\theta_1),\tag{9}$$

where $\hat\sigma_i$ ($i=x,\,y,\,z$) are the Pauli matrices. The same calculations as in the case of a magnetic field yield for the correction to the action

$$\delta A_\sigma^\eta=\frac{\eta\pi\omega_0}{2\Omega_0}\left(\hat\sigma_x+i\,\frac{S_2^3\Omega_0K_\perp}{\widetilde{z}(\widetilde{J}+2K_\perp S_2^2)}\hat\sigma_y\right)+i\,\frac{\eta\pi\omega_0S}{4\widetilde{z}}\hat\sigma_y.\tag{10}$$

6. There are two characteristic time scales in the problem: Ω_0^{-1} corresponds to the tunneling time through the barrier and the second time scale is determined by the tunneling splitting $2\Delta_0$ (see also Ref. 17):

$$2\Delta_0=\Omega_0\sqrt{\frac{6}{\pi}A_0}\,\exp\{-A_0\};\tag{11}$$

and Δ_0^{-1} corresponds to the time during which the system occupies one of the minima. If $\Omega_0^{-1}\ll t\ll\Delta_0^{-1}$, the relation between the transition amplitude (2) and the off-diagonal part of the effective Hamiltonian can be represented in the form (we have returned to the real time axis)

$$H_{\rm eff}^{\rm OD}=\frac{i}{t}\{\hat\tau_-\hat\Gamma_{\Downarrow\Uparrow}(t)+\text{ h.c.}\},\quad \Gamma_{\Downarrow\Uparrow}(t)=it\Delta_0\sum_{\eta=\pm}\exp\{-A^\eta\},\tag{12}$$

where $\hat\tau_-$ is a lowering operator in the space of Pauli matrices. Then, in the antiferromagnetic (when $S_1=S_2$ and the Néel vector tunnels), retaining only the leading terms in the corrections to the action (and setting for simplicity $H_x=0$), we obtain

$$A^\eta(0)=A_0(0)-i\eta\psi(0)+\eta\alpha(0)(\hat\sigma_x+i\lambda(0)\hat\sigma_y),\quad \Omega_0(0)=2S_2\sqrt{K_\parallel(J+K_\perp)},$$

$$A_0(0)=4S_2\lambda(0),\quad \psi(0)=\frac{\pi H_y}{J+K_\perp},\quad \alpha(0)=\frac{\pi\omega_0}{2\Omega_0(0)},\quad \lambda(0)=\sqrt{K_\parallel/(J+K_\perp)}.\tag{13}$$

Substituting expressions (13) into Eq. (12) gives the off-diagonal (i.e., corresponding to tunneling) part of the effective Hamiltonian

$$H_{\rm eff}^{\rm OD}(0)=2\Delta_0(0)\hat\tau_-\cos[\psi(0)+\alpha(0)(i\hat\sigma_x-\lambda(0)\hat\sigma_y)]+\text{h.c.}\tag{14}$$

(the diagonal (static) part will not be given here; a general method of calculating it is given in Ref. 14.) We note that in the case $S_1\gg S_2$ an effective Hamiltonian is obtained which describes tunneling of magnetization in a ferromagnetic granule.[14]

In the case of arbitrary S (ferrimagnet), however, the Néel vector tunnels *together* with the excess spin. In the limit $\tilde J\gg 2K_\perp S_2^2$ the effective Hamiltonian has the form (once again we set $H_x=0$)

$$H_{\rm eff}^{\rm OD}(S)=2\Delta_0(S)\hat\tau_-\cos[\pi S-\psi(S)-\alpha(S)(i\hat\sigma_x-\lambda(S)\hat\sigma_y)]+\text{h.c.},$$

$$A_0(S)=\sqrt{4\frac{K_\parallel}{K_\perp}\left(S^2+S_2^2\frac{2\tilde K_\perp}{\tilde J}+SS_2^3\frac{4K_\perp}{\tilde J}\right)},\quad \lambda(S)=\frac{\Omega_0(S)}{\tilde K_\perp}\left(\frac{S}{2}+\frac{K_\perp S_2^3}{\tilde J}\right),$$

$$\psi(S)=\frac{\pi A_0(S)H_y}{2\Omega_0(S)},\quad \alpha(S)=\frac{\pi\omega_0}{2\Omega_0(S)},\quad \Omega_0(S)=\sqrt{\frac{4\tilde K_\parallel\tilde K_\perp\tilde J}{S^2\tilde J+2\tilde K_\perp S_2^2+4SS_2^3K_\perp}}.\tag{15}$$

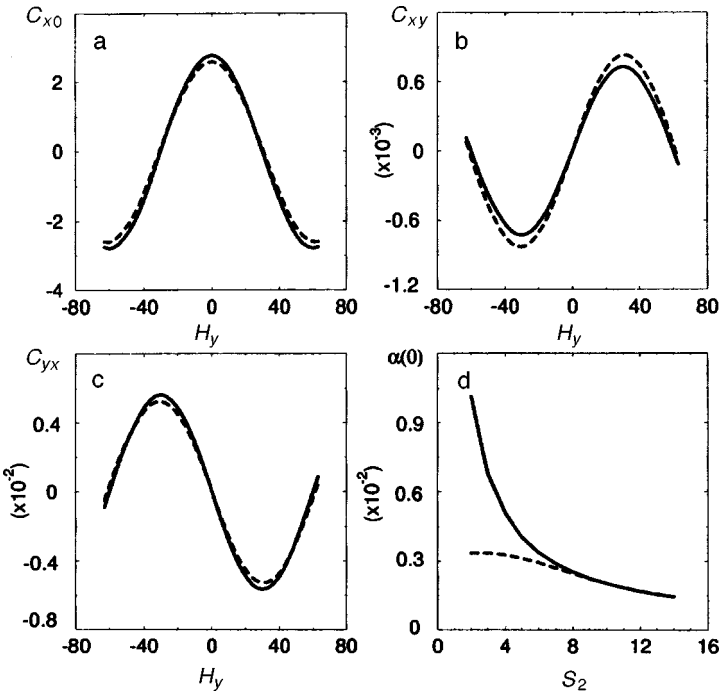

FIG. 1. a) – c). Numerical coefficients C_{ij} (dashed curves) compared with the analytical expressions from Eq. (16) (solid curves) as a function of the magnetic field H_y with $J=40$, $K_\perp=20$, $K_\parallel=1$, $\omega_0=0.2$, $S_1=S_2=10$, and $\sigma=1/2$. d) Numerical (dashed curve) and analytical (16) (solid curve) dependences of the coefficient α on the magnitude of the sublattice spin with $J=40$, $K_\perp=20$, $K_\parallel=1$, $\omega_0=0.2$, and $\sigma=1/2$.

A natural criterion arises for the magnitude of the excess spin according to which switching occurs from a ferromagnetic to an antiferromagnetic regime: $S \gg S_2(2\tilde{K}_\perp/(\tilde{J}+2K_\perp S_2^2))^{1/2}$ — *ferromagnetic regime;* $S \ll S_2(2\tilde{K}_\perp/(\tilde{J}+2K_\perp S_2^2))^{1/2}$ — *antiferromagnetic regime.*

7. We now use the method of exact diagonalization applied to the initial Hamiltonian (1) with $H_x=0$ to check the formulas obtained. For lack of space, here the computational results are presented only for the antiferromagnetic case ($S_1=S_2$). The exact diagonalization procedure is described in detail in Ref. 14. For this reason, here we shall determine only the quantities subject to analysis. Expanding expression (14) in a series up to terms linear in ω_0 gives

$$H_{\text{eff}}^{\text{OD}} \approx 2\Delta_0(0)(\cos\psi(0)\cdot\hat{\tau}_x\hat{\sigma}_0 - \alpha(0)\sin\psi\cdot\hat{\tau}_y\hat{\sigma}_x + \alpha(0)\lambda(0)\sin\psi\cdot\hat{\tau}_x\hat{\sigma}_y). \qquad (16)$$

The dynamic part of the effective Hamiltonian obtained by exact diagonalization has the form

$$H_{\text{ED}}^{\text{OD}} = C_{x0}\cdot\hat{\tau}_x\hat{\sigma}_0 + C_{xy}\cdot\hat{\tau}_x\hat{\sigma}_y + C_{yx}\cdot\hat{\tau}_y\hat{\sigma}_x, \qquad (17)$$

where these coefficients C_{ij} are shown in Figs. 1a, b, and c (dashed lines) together with the corresponding analytical quantities from Eq. (16) (solid lines) as a function of the

applied magnetic field with $J=40$, $K_{\perp}=20$, $K_{\|}=1$, $\omega_0=0.2$, $S_1=S_2=10$, and $\sigma=1/2$. The coefficient $\alpha(0)$, developed from C_{yx} (dashed line), together with its analytical analog from Eq. (13) (solid line) is plotted in Fig. 1d as a function of the sublattice spin with $J=60$, $K_{\perp}=20$, $K_{\|}=1$, $\omega_0=0.2$, and $\sigma=1/2$. This coefficient describes the interaction with the spin thermostat and correspondingly it is of greatest interest in the present work. As one can see from all figures, the agreement between the analytical and the computer calculations is satisfactory. The discrepancy between the two values for α for small S_2 has an obvious explanation: The quasiclassical description is still not valid at such values of the spin.

8. My objective in the present work was not to make a *detailed* analysis of all factors influencing the tunneling process but some obvious qualitative conclusions can be drawn even without practical calculations (with the obtained Hamiltonians) according to the spin dynamics of the systems studied: (i) Tunneling in antiferromagnetic systems is indeed manifested much more strongly than in ferromagnetic systems, since $A_0(AFM)<A_0(FM)$; (ii) the presence of an excess spin has a strong effect on the tunneling process, at least because of the fact that it renormalizes A_0 and Ω_0, which together determine the magnitude of the tunneling splitting and the tunneling frequency; (iii) the interaction with the spins in the environment is extremely important because it can radically change the tunneling picture, right up to complete suppression of tunneling, just as in the case of tunneling of half-integer excess spin or half-integer ''giant spin.''

I thank N. Prokof'ev, F. Stamp, and B. Barbara for numerous helpful discussions and the L. Néel Laboratory (Grenoble, France), where part of this work was performed, for hospitality. This work was supported by the Russian Fund for Fundamental Research (Project 97-02-16548).

[1] J. L. Van Hammen and A. Suto, Europhys. Lett. **1**, 481 (1986); E. M. Chudnovsky and L. Gunter, Phys. Rev. Lett. **60**, 661 (1988); P. C. E. Stamp, E. M. Chudnovsky, and B. Barbara, Int. J. Mod. Phys. **6**, 1355 (1992).
[2] L. Gunter and B. Barbara (eds.), *Quantum Tunneling of Magnetization*, QTM'94 (1995).
[3] B. Barbara and E. M. Chudnovsky, Phys. Lett. A **145**, 205 (1990); E. M. Chudnovsky, in Ref. 2, p. 76.
[4] I. V. Krive and O. B. Zaslavskii, J. Phys.: Condens. Matter **2**, 9457 (1990).
[5] E. N. Bogachek and I. V. Krive, Phys. Rev. B **46**, 14559 (1992).
[6] G. Levine and J. Howard, Phys. Rev. Lett. **75**, 4142 (1995).
[7] B. A. Ivanov and A. K. Kolezhuk, http://xxx.lanl.gov/abs/cond-mat/9706292
[8] S. E. Barnes, R. Ballou, B. Barbara, and J. Strelen, Phys. Rev. Lett. **79**, 289 (1997).
[9] A. Chiolero and D. Loss, http://xxx.lanl.gov/abs/cond-mat/9708042.
[10] W. Wernsdorfer, K. Hasselbach, E. Bonet Oronzo, Phys. Rev. Lett. **79**, 4014 (1997); J. Tejada, X. X. Zhang, E. del Barco, Phys. Rev. Lett. **79**, 1754 (1997).
[11] P. C. E. Stamp, Nature **359**, 365 (1992); Physica B **197**, 133 (1994).
[12] D. D. Awshalom, J. F. Smyth, G. Grinstein, Phys. Rev. Lett. **68**, 3092 (1992).
[13] N. V. Prokof'ev and P. C. E. Stamp, J. Phys. CM Lett. **5**, L663 (1993); N. V. Prokof'ev and P. C. E. Stamp, J. Low Temp. Phys. **104**, 143 (1996); A. Garg, Phys. Rev. Lett. **71**, 4249 (1993).
[14] I. S. Tupitsyn, N. V. Prokof'ev, and P. C. E. Stamp, Int. J. Mod. Phys. B **11**, 2901 (1997).
[15] E. Fradkin, *Field Theories of Condensed Matter Systems*, Frontiers in Physics, No. 82, 1991.
[16] A. F. Andreev and V. I. Marchenko, Usp. Fiz. Nauk **130**, 39 (1980) [Sov. Phys. Usp. **21**, 23 (1980)].
[17] S. N. Burmistrov and L. B. Dubovksiĭ, Preprint IAÉ-3881/1 [in Russian], Kurchatov Institute of Atomic Energy, Moscow (1984).

Translated by M. E. Alferieff

Magnetic and magnetooptical properties of Au/Cu-wedge/15-Å-NiFe sandwiches

E. E. Shalygina, A. V. Vedyaev, O. A. Shalygina, and I. A. Pogrebnaya
Department of Physics, M. V. Lomonosov Moscow State University, 119899 Moscow, Russia

A. Marty and B. Gilles
CEA. DRFMC. CEN G / SP2M / PM, 38054 Grenoble, CEDEX 9, France

(Submitted 26 November 1997)
Pis'ma Zh. Éksp. Teor. Fiz. **67**, No. 1, 33–36 (10 January 1998)

The results of an investigation of the magnetic and magnetooptical properties of Au/Cu-wedge/15-Å-NiFe sandwiches are reported. Oscillations of the equatorial Kerr effect as a function of the copper wedge thickness are observed. The period of these oscillations is found to be of the order of 5–6 Å. The experimentally observed oscillations of the equatorial Kerr effect are attributed to a quantum size effect. [S0021-3640(98)00601-X]

PACS numbers: 78.20.Ls, 75.70.Cn

The problem of theoretical and experimental investigation of the quantum size effect has become popular in recent years. This was promoted by the development of technologies making it possible to obtain samples where the specific atomic layers are localized with a high degree of accuracy. The quantum size effect is due to the small thicknesses of the film samples or individual layers in multilayer structures. It is manifested in the dependence of the physical properties of a sample on its thickness t. It is known[1] that when t becomes small the motion of charge carriers between the surfaces of the sample can manifest a quantum character. The discrete electronic states appearing in the process in a direction perpendicular to the surface of the sample are ordinarily called quantum well states (QWS). QWS in ultrathin (of the order of several monolayers) samples can be observed directly by the method of photoemission spectroscopy. Investigations performed in recent years by this method have confirmed the existence of QWS in (100) and (111) ultrathin paramagnetic Ag, Au, and Cu layers on ferromagnetic substrates (Fe, Co)[2–6] and in ultrathin magnetic films on paramagnets.[2,7,8] It was now been proved that QWS make it possible to explain the experimentally observable values of the period of the oscillations of the exchange interaction between ferromagnetic layers through a nonmagnetic layer[9,10] as well as oscillations in the values of the magnetoresistance in multilayer structures (see, for example, Ref. 11) and the magnetooptical Kerr effect in ultrathin films of iron[12–14] and cobalt.[14–16] At the same time, analysis of the existing data shows that the effect of QWS on the magnetic and magnetooptical properties of paramagnetic layer/magnetic film sandwiches has not been adequately studied. Actually, the only work where the results of a magnetooptical investigation of Au-wedge/Co(0001) samples are presented is Ref. 6.

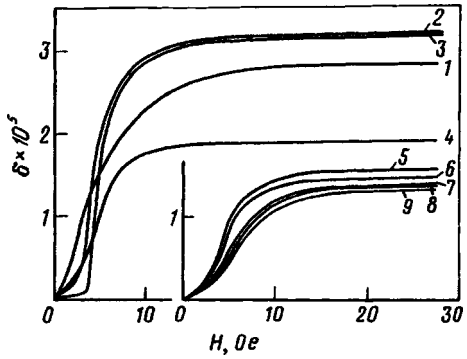

FIG. 1. Typical local magnetization curves for a Au/Cu-wedge/15-Å-NiFe sandwich. The curves were obtained by displacing a light spot over the central section of a wedge along the length of the wedge ($\hbar\omega = 2.7$ eV).

In the present letter we report the results of an investigation of the influence of quantum size effects on the magnetic and magnetooptical properties of Au/Cu-wedge/15-Å-$Fe_{80}Ni_{20}$ sandwiches.

The experimental samples were prepared by molecular-beam epitaxy with a base pressure of 10^{-10} torr in the chamber. Polished MgO (001) crystals were used for substrates. To remove the absorption gases and relieve stress, the substrates were first annealed at 950 °C for 1 min. After cooling to room temperature, a quite thick Cu layer was deposited. A 15-Å thick permalloy film was deposited on the Cu layer and a 20 mm long Cu wedge with a 1.35 Å/mm slope and minimum and maximum thicknesses of 4 and 31 Å, respectively, 20 mm was deposited on the permalloy layer. To prevent oxidation the Cu wedge was coated with a 20 Å thick Au layer. A transverse section of the sandwich is shown in the inset in Fig. 2 (see below).

The measurements were performed on a magnetooptic micromagnetometer, a detailed description of which is given in Ref. 17. Investigation of the hysteresis and magnetooptical properties of the experimental sample were performed with the aid of an equatorial Kerr effect — δ (the external magnetic field is perpendicular to the plane of incidence of the light and parallel to the surface of the magnet). In this case the ac magnetic field H with frequency $f = 80$ Hz was applied in the plane of the sample along the length L of the wedge. The magnetooptical signal δ was detected in the reflection of light from a microsection with diameter $D = 30$ μm of the surface. The local magnetization curves $\delta(H) \sim M(H)$ (M — magnetization of the sample) and the dependence $\delta(L)$, which is equivalent to $\delta(t_{Cu})$, were obtained in a recording regime on an automatic recorder. The measurements of $\delta(H)$ were performed with a step D with the light beam displaced along the length of the wedge. The photon energy $\hbar\omega$ of the incident light was fixed.

Figure 1 displays typical local magnetization curves $\delta(H) \sim M(H)$ measured for the experimental sample with $\hbar\omega = 2.7$ eV. The curve *1* was obtained on a microsection with $t_{Cu} \sim 4$ Å. The curves *2*, *3*, and so on were obtained with the light beam displaced by 1 mm along the central section of the wedge. It is evident from the figure that the local magnetization curves for the experimental sample are substantially different. At the same

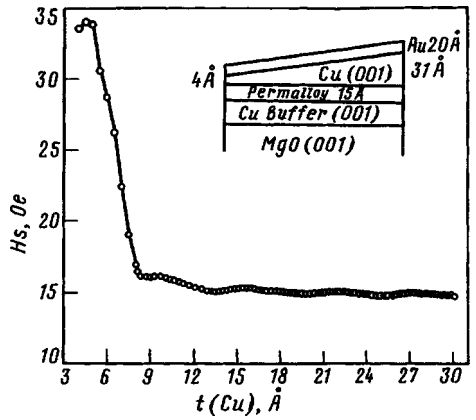

FIG. 2. Local values of the saturation field in the experimental sample versus copper wedge thickness. Inset: Transverse section of the sample.

time, there exists on all curves $\delta(H)$ a field H in which δ no longer varies in magnitude. This value of H corresponds to the technological saturation field Hs of the given local microsection of the sample. By analyzing curves of this type it is possible to construct the dependence $Hs(t_{\mathrm{Cu}})$ and to determine the maximum value $Hs^{\max}$ for the experimental sample (see Fig. 2). Curves of the equatorial Kerr effect as a function of the thickness of the copper wedge were measured for $H>Hs^{\max}$ and fixed $\hbar\omega$. Figure 3 displays a typical curve $\delta(t_{\mathrm{Cu}})$ obtained with $\hbar\omega=2.7$ eV. One can see from the figure that δ has a maximum value at $t_{\mathrm{Cu}}\sim 5.5$ Å. The value of δ drops sharply in the region $6<t_{\mathrm{Cu}}<8$ Å. For $t_{\mathrm{Cu}}>8$ Å δ decreases continuously with increasing thickness of the copper wedge; in the process, δ is observed to oscillate with a small amplitude. The period of these oscillations equals $\sim 5-6$ Å. For clarity, a section of $\delta(t_{\mathrm{Cu}})$ for $t_{\mathrm{Cu}}>8$ Å is presented on

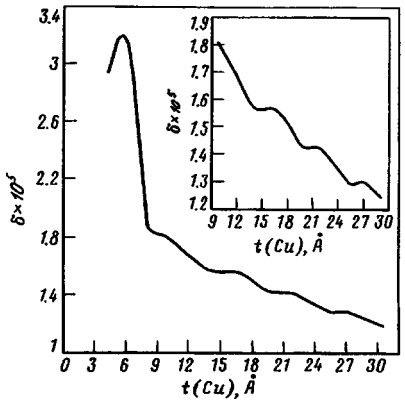

FIG. 3. Equatorial Kerr effect in the experimental sample versus the copper wedge thickness.

an enlarged scale in the inset in Fig. 3. Comparing Figs. 2 and 3 shows that the dependence of the local values of the saturation field Hs on the thickness of the copper wedge is similar to $\delta(t_{Cu})$.

Similar measurements were performed for other values of $\hbar\omega$ (2.5 and 3.2 eV) and on sandwiches with a permalloy layer thickness $t_{perm}=25$ and 35 Å. On account of the smallness of the amplitude of the oscillations of δ no appreciable changes in the period of the oscillations of δ as a function of $\hbar\omega$ were observed. It was established that the curves $\delta(t_{Cu})$ for samples with $t_{perm}=25$ and 35 Å are similar in form to $\delta(t_{Cu})$ obtained for a sample with $t_{perm}=15$ Å. The difference was that in the entire interval of copper wedge thicknesses the values of δ increased linearly with t_{perm} but the oscillations of δ were virtually unnoticeable.

The data obtained can be explained as follows. As already mentioned, the photoemission spectroscopy investigations confirmed the existence of QWS in ultrathin layers of precious metals (Ag, Au, Cu) on magnetic substrates. Thus, it was observed in Refs. 2 and 4 that the strongest changes, consisting of the appearance of the first additional peak in the photoemission spectrum, are observed for a Cu layer on a Co(001) substrate with $t_{Cu}\sim 2$ monolayers, and for a Cu layer on a Fe(001) substrate with $t_{Cu}\sim 1.5$ monolayers. As t_{Cu} increased, the intensity of this peak decreased and the position of the peak shifted toward the Fermi level. It was established that the photoemission intensity at the Fermi level oscillates in magnitude as a function of the thickness of the Cu film. The period of these oscillations equals ~ 4.5–6 monolayers (1 monolayer ~ 1.8 Å). The periodic variation of the photoemission spectrum as a function of the Cu layer thickness proves the existence of QWS.[18] In Ref. 2 and 4 it is shown that on account of the spin-dependent boundary conditions at the copper/ferromagnet interface QWS in Cu films are spin-polarized. This feature of QWS remains in Cu films all the way up to $t_{Cu}\sim 30$ monolayers thick. The presence of spin-polarized QWS in ultrathin Cu films attests to the fact that the copper atoms carry a small magnetic moment, which changes as t_{Cu} increases and which is impossible to estimate from photoemission spectra. At the same time, there is no doubt that the experimentally observed strong change, as compared with bulk samples, in the electronic structure of ultrathin Cu films on magnetic substrates and the consequent appearance of a small magnetic moment in the copper atoms should influence the magnetic and magnetooptical properties of the magnet bordering the Cu film. In the case of sandwiches with a wedge-shaped Cu layer, the local magnetic and magnetooptical properties of the layer should vary along the length of the wedge. On this basis, the Cu-wedge thickness dependences of the local magnetic and magnetooptical properties of the sandwich should have an oscillatory character and the strongest changes in these properties should be observed for small values of t_{Cu}. Our data for a Au/Cu-wedge/15-Å-$Fe_{80}Ni_{20}$ sandwich agree with this conclusion.

The decrease in the amplitude of the oscillations of δ for samples with $t_{perm}=25$ and 35 Å is apparently due to the fact that the maximum effect of the QWS on the magnetooptic properties of sandwiches will obtain for some thickness of the magnetic layer. In our case this optimal thickness was found to be 15 Å. Finally, the linear increase in δ with t_{perm} agrees with the calculations performed in Ref. 19.

So, we have observed in Au/Cu-wedge/15-Å-$Fe_{80}Ni_{20}$ sandwiches an oscillatory dependence of the equatorial Kerr effect and local values of the saturation field on the

thickness of the copper wedge. The data obtained were explained by the existence of spin-polarized QWS in the Cu layer and their effect on the sandwich properties which were studied.

[1] M. D. Stiles, Phys. Rev. B **48**, 7238 (1993).
[2] J. E. Ortega and F. J. Himpsel, Phys. Rev. **69**, 844 (1992); J. E. Ortega, F. J. Himsel, G. J. Mankey *et al.*, Phys. Rev. Lett. **47**, 1540 (1993).
[3] D. Hartmann, W. Weler, A. Rampe *et al.*, Phys. Rev. B **48**, 16937 (1993).
[4] K. Garrison, Y. Chang, and P. D. Johnson, Phys. Rev. Lett. **71**, 2801 (1993).
[5] C. Carbone, E. Vescovo, O. Rader *et al.*, Phys. Rev. Lett. **71**, 2805 (1993).
[6] R. Megy, A. Bounouh, Y. Suzuki *et al.*, Phys. Rev. B **51**, 5586 (1995).
[7] F. J. Himpsel, Phys. Rev. B **44**, 5966 (1991).
[8] W. Clemens, T. Kachel, E. Vescovo *et al.*, Solid State Commun. **81**, 739 (1992).
[9] D. M. Edwards, J. Mathon, R. B. Muniz *et al.*, Phys. Rev. Lett. **67**, 493 (1991).
[10] P. Bruno, J. Magn. Magn. Mater. **121**, 248 (1993).
[11] S. S. P. Parkin, N. More, and K. Roche, Phys. Rev. Lett. **64**, 2304 (1990).
[12] Y. Suzuki, T. Katayma, S. Yoshida *et al.* Phys. Rev. Lett. **68**, 3355 (1992).
[13] W. Geerts, Y. Suzuki, T. Katayma *et al.*, Phys. Rev. B **50**, 12581 (1992).
[14] S. D. Bader and Li Dongqi, J. Magn. Magn. Mater. **156**, 153 (1996).
[15] T. Katayma, W. Geerts, Y. Suzuki *et al.*, J. Magn. Magn. Mater. **156**, 171 (1996).
[16] E. E. Shalygina, A. V. Vedyaev, A. Marty *et al.*, Vest. Mosk. Gos. Univ. Ser. 3 Fiz. Astron. **6**, 102 (1996).
[17] G. S. Krinchik, E. E. Chepurova (Shalygina), N. N. Usov, and N. P. Samrov, Pis'ma Zh. Tekh. Fiz. **28**, 1372 (1981).
[18] F. J. Himsel, Phys. Rev. B **44**, 5966 (1991).
[19] G. Traeger, L. Wenzel, and A. Hubert, Phys. Status Solidi A **131**, 201 (1992).

Translated by M. E. Alferieff

Giant negative magnetoresistance in a composite system based on Fe_3O_4 nanocrystals in a polymer matrix

A. E. Varfolomeev,[a] D. Yu. Godovskiĭ, and G. A. Kapustin
Kurchatov Institute Russian Science Center, 123182 Moscow, Russia

A. V. Volkov and M. A. Moskvina
M. V. Lomonosov Moscow State University, 119899 Moscow, Russia

(Submitted 27 November 1997)
Pis'ma Zh. Éksp. Teor. Fiz. **67**, No. 1, 37–40 (10 January 1998)

Conducting polymer composites based on Fe_3O_4 nanocrystals in a polyvinyl alcohol matrix are synthesized. The current–voltage characteristics, the magnetization, and the magnetoresistance of the nanocomposites are investigated, and a giant negative magnetoresistance is observed. The decrease in the resistance at room temperature is found to reach 10% in a 10 kOe field. © *1998 American Institute of Physics.* [S0021-3640(98)00701-4]

PACS numbers: 81.05.Qk, 81.05.Ys, 75.80.+q, 72.80.Le

Giant negative magnetoresistance (GMR) was initially observed in multilayer magnetic structures.[1] Later it was also observed in granular magnetic films, consisting of particles of a magnetic metal (Fe, Co, Ni) in a nonmagnetic-metal matrix[2,3] or in a dielectric matrix (for example, SiO_2).[4,5] It is believed that in the case of a system of nanoparticles of a magnetic metal in a nonmagnetic-metal matrix the GMR is due to the additional scattering of spin-polarized charged carriers, which depends on the relative orientation of the magnetic moments of the nanoparticles.[6] In the case of a dielectric matrix the GMR is explained by spin-dependent tunneling between magnetic nanoparticles.[7] However, the nature of the GMR in granular systems has still not been completely elucidated.

The method for obtaining polymer composites containing iron oxide (magnetite Fe_3O_4 and Fe_2O_3) is based on performing *in situ* reactions in a volume of swollen polymer matrices. Magnetite contains iron with degrees of oxidation +2 and +3 in a 1:2 ratio, so that a mixture of salts of di- and trivalent iron must be used in order to obtain it. Polymer–iron oxide nanocomposites were obtained by treating polyvinyl alcohol (PVA) films, containing a mixture of $FeCl_2$ and $FeCl_3$ salts, with an alkali solution (4 N NaOH). The duration of the treatment was 12 h. To prepare PVA films containing iron salts water solutions of PVA and $FeCl_2$ and $FeCl_3$ salts were mixed in a 1:1 molar ratio. The PVA concentration in the resulting solution was equal to 4 wt.%. The films were obtained by pouring a PVA–$FeCl_2$/$FeCl_3$ solution onto a glass substrate. The reaction between the iron ions immobilized in the volume of the polymer matrix (coordination-linked with the hydroxyl groups of PVA) and the OH^- groups of the alkali results ultimately in the formation of nanoparticles of iron oxides. This is manifested externally in the appearance of intense film color, ranging from yellow-brown (characteristic for Fe_2O_3) to black

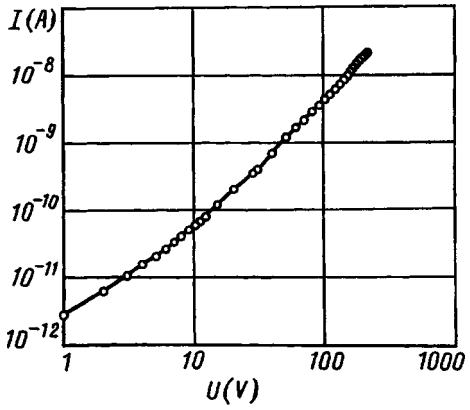

FIG. 1. Current–voltage characteristic.

(Fe_3O_4). The blackest samples (samples with the highest Fe_3O_4 content) were obtained using a mixture of $FeCl_2$ and $FeCl_3$ in a 1:1 molar ratio. The use of a stoichiometric mixture with a 1:2 molar ratio decreases the Fe_3O_4 content in the composite in connection with the oxidation of Fe^{2+} by oxygen in air to Fe^{3+} during the process of drying a sample (3–4 days at 20 °C). The iron oxide content in the composite was determined by a thermogravimetric method on a Mettler TA-4000 device. The Fe_3O_4 content in the experimental samples reached 150 wt.% (or 24 vol.%). At this concentration it was possible to observe conduction in the nanocomposite. The experimental samples consisted of 2×2 mm and 100 μm thick film with contacts deposited by means of silver paste. The average particle size in the composite, estimated according to the half-width of the x-ray reflection, was $\approx$100 Å. An estimate of the concentration of Fe_3O_4 particles in the experimental samples with a concentration of 24 vol.% gives 5×10^{17} cm^{-3}.

The current–voltage characteristic (IVC) was investigated with a V7-30 electrometer up to a voltage of 300 V (Fig. 1). The IVC on a double logarithmic scale can be approximated with two linear sections, corresponding to power-law functions of the current versus the voltage with exponents of 1 and 2.05 ± 0.02. Thus, the IVC is of a linear, Ohmic character on the initial section and quadratic at high voltages, as is characteristic for space-charge-limited injection currents, neglecting the effect of traps. The density n of equilibrium charge carriers and their effective drift mobility μ can be estimated from the magnitude of the voltage at which a transition occurs from Ohmic to injection conduction and according to the conductivity in the Ohmic region $\sigma=3\times 10^{-11}$ $(\Omega\cdot\text{cm})^{-1}$ (Ref. 8):

$$V_x=enL^2/\epsilon, \quad \sigma=\mu ne. \tag{1}$$

Here $V_s=10$ V is the voltage at which a transition occurs from Ohm's law to a trapless quadratic law; L is the distance between the contacts; and, ϵ is the permittivity of the nanocomposite. An estimate gives the equilibrium carrier density $n\approx 6\times 10^9$ cm^{-3} and the effective drift mobility $\mu\approx 0.1$ cm^2/V·s.

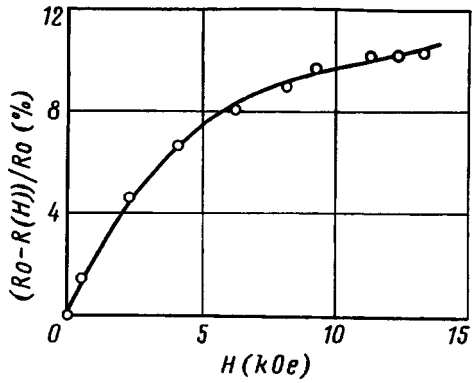

FIG. 2. Magnetoresistance versus magnetic field.

The magnetoresistance was investigated right up to fields 14 kOe with different orientations of the sample relative to the direction of the magnetic field and with a voltage of 100 V on the sample, which corresponds to the carrier-injection regime. The typical resistance of the samples was equal to $2\times10^9\ \Omega$. The sign of the variation of the resistance in the magnetic field was negative. The field dependence of the magnetoresistance determined as $[R(H=0)-R(H)]/R(H=0)$ is nonlinear and saturates in high fields (Fig. 2). The magnetoresistance reached 10–12% in a 10 kOe magnetic field and the absolute magnitude of the change in the resistance in the magnetic field was equal to $2\times10^8\ \Omega$. We note that this value is much larger than in granular systems based on Co and Ni nanoparticles in a SiO_2 matrix. The GMR in these systems in a 10 kOe field was equal to 4.5% and 0.6%, respectively.[4,5] The magnetoresistive sensitivity in our case in weak fields was equal to 2–3%/kOe. A weak anisotropy of the magnetoresistance was observed. In a magnetic field oriented in a direction perpendicular to the current the magnetoresistance saturated in weak fields, $\sim$6 kOe, and its magnitude was smaller. It is interesting that in a close to Ohmic regime (with a voltage of 15 V on the sample) the GMR was several times smaller ($\approx2\%$) than in the injection regime. The increase in the GMR with increasing voltage could be due to the fact that in the presence of injection the Fermi quasilevel shifts and the degree of carrier polarization $(D_\uparrow-D_\downarrow)/(D_\uparrow+D_\downarrow)$ increases, where $D_\uparrow$ is the density of states for carriers with the corresponding spin.

The magnetic-field dependence of the magnetization M was also investigated (Fig. 3). The measurements were performed in a pulsed magnetic field up to 70 kOe over a time $\approx10^{-2}$ s. The absence of hysteresis in the magnetization curve and the slow approach to saturation in fields >10 kOe indicate that in our case the Fe_3O_4 nanoparticles at room temperature are in a superparamagnetic state.[9] The magnetic moment per Fe_3O_4 ''molecule'' in a nanoparticle can be estimated from the saturation magnetization as $\approx1.98\mu_B$ (where μ_B is the Bohr magneton). For comparison, in bulk Fe_3O_4 the magnetic moment per ''molecule'' is $(4.03-4.08)\mu_B$.[10] Thus even in fields $\sim$70 kOe almost half the particles are in a superparamagnetic state during the observation time $\approx10^{-2}$ s.

The magnetization dependence of the magnetoresistance was constructed from the

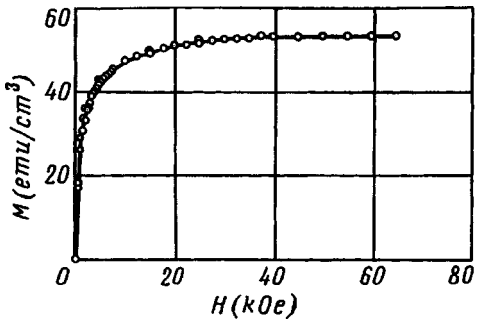

FIG. 3. Magnetization versus magnetic field.

magnetic field dependences of the magnetoresistance and magnetization. This dependence can be approximated by a quadratic function

$$[R(H=0)-R(H)]/R(H=0)=(60\pm 1.6)\cdot 10^{-6}\cdot M^2, \tag{2}$$

where M is the magnetization in CGSM units/cm^3. This character of the dependence agrees with the theoretical and experimental results on GMR in granular systems.[5,7]

As far as we know, the GMR effect in composites based on ferrite nanocrystals in a polymer matrix had never been observed prior to this. The nature of the GMR in our case can be explained, just as in the case of a system of nanoparticles of a magnetic metal in a dielectric matrix, by tunneling of charge carriers, which depends on the relative orientation of the magnetic moments of the nanoparticles of the ferromagnet.[7]

This work was supported by the Russian Fund for Fundamental Research (Grant 96-03-32397a).

[a)]e-mail: aev@oimrds.kiae.su

[1] M. N. Baibich, J. M. Broto, A. Fert *et al.*, Phys. Rev. Lett. **61**, 2472 (1988).
[2] A. E. Berkowitz, J. R. Mitchell, M. J. Cavey *et al.*, Phys. Rev. Lett. **68**, 3745 (1992).
[3] J. Q. Xioa, S. Jiang, and C. L. Chien, Phys. Rev. Lett. **68**, 3749 (1991).
[4] J. I. Gittelman, Y. Goldstein, and S. Bozovsky, Phys. Rev. B **5**, 3609 (1972).
[5] A. Milner, A. Gerber, B. Groisman *et al.*, Phys. Rev. Lett. **76**, 475 (1996).
[6] R. E. Camley and J. Barnas, Phys. Rev. Lett. **63**, 664 (1989).
[7] J. Inoue and S. Maekawa, Phys. Rev. B **53**, 927 (1996).
[8] M. A. Lampert and P. Mark, *Current Injection in Solids*, Academic Press, New York, 1970.
[9] S. Morup, H. Topsoe, and J. Lipka, J. de Physique **37**, 287 (1976).
[10] A. S. Pakhomov and N. A. Smol'kov, *Ferrites* [in Russian], Progress in Science, No. 4, Soviet Academy of Sciences Press, Moscow, 1962.

Translated by M. E. Alferieff

Electron g factor in quantum wires and quantum dots

E. L. Ivchenko and A. A. Kiselev
A. F. Ioffe Physicotechnical Institute, Russian Academy of Sciences, 194021 St. Petersburg, Russia

(Submitted 17 November 1997)
Pis'ma Zh. Éksp. Teor. Fiz. **67**, No. 1, 41–45 (10 January 1998)

A theory of the Zeeman effect for electrons in one- and zero-dimensional semiconductor heterostructures is developed. A relation is established between the number of linearly independent components of the g-factor tensor and the point symmetry of a low-dimensional system. A specific calculation is performed for a spherical quantum dot and a cylindrical wire. © *1998 American Institute of Physics.* [S0021-3640(98)00801-9]

PACS numbers: 73.61.Ey, 71.70.Ej

The effective Landé g factors for electrons in semiconductors with the zinc blende lattice vary as a function of the chemical composition over wide limits ($g \approx 2$ in wide-gap materials, $g = -0.44$ in GaAs, and $g \approx -50$ in InSb). This dependence is described well by the Roth formula,[1] introduced in second-order kp perturbation theory. In Ref. 2 we extended the g factor theory to structures with quantum wells and superlattices, and we calculated the dependence of the g factor on the width of the layers and predicted an anomalously high anisotropy of the Zeeman effect for electrons in the conduction band of the heterostructure. Experiments confirmed that the theory developed is applicable for structures grown on the basis of III–V and II–VI cubic semiconductors.[3–9] The first measurements of the g factor in structures with quantum dots have appeared.[10] In the present letter we construct a theory of the Zeeman effect for electrons in quasi-one- and quasi-zero-dimensional systems, i.e., in quantum wires and dots. The dependence of the g factor on the system size is calculated for a wire with a circular cross section and for a spherical quantum dot.

As in Ref. 2, to calculate the electron g factor we employ the Kane model, in which the kp mixing of the states in the conduction band Γ_6 and in the valence bands Γ_8 and Γ_7 is taken into account exactly but the effect of remote bands is neglected. Let us expand the electron wave function in terms of Bloch functions $c_s R_j(r)$, where the c_s ($s = \pm 1/2$) are $\uparrow$ and $\downarrow$ spin column matrices and the R_j are the coordinate functions S (Γ_1 representation of the point group T_d) and X, Y, Z (Γ_{15} representation). It is convenient to represent the eight envelopes in the form of a spinor $u(r)$ with the components $u_{1/2}$, $u_{-1/2}$ for the Bloch functions $S\uparrow$ and $S\downarrow$ and the vector spinor $v = (v_x, v_y, v_z)$, where v_x is a spinor with the components $v_{x,1/2}$ and $v_{x,-1/2}$ for the Bloch functions $X\uparrow$, $X\downarrow$, and so on.

The Schrödinger equation with the kp Hamiltonian $H(\hat{k})$ in the form of an 8×8 matrix can be reduced to the differential equation

$$\frac{\hbar^2\hat{k}^2}{2m_c(E)}u=Eu \tag{1}$$

for the spinor u, and the vector spinor v can be related with the gradient ∇u by the relation

$$v=\frac{1}{P}\frac{\hbar^2}{2m_c(E)}\nabla u-i\frac{1}{P}\frac{\hbar^2}{4m_0}[g(E)-g_0](\vec{\sigma}\times\vec{\nabla})u. \tag{2}$$

Here E is the electron energy measured from the bottom of the Γ_6 conduction band, $\hat{k}=-i\nabla$, $P=i(\hbar/m_0)\langle S|\hat{p}_z|Z\rangle$, m_0 and g_0 are the free-electron mass and Landé factor ($g_0\approx 2$), and

$$\frac{1}{m_c(E)}=\frac{2}{3}\frac{P^2}{\hbar^2}\left(\frac{2}{E_g+E}+\frac{1}{E_g+E+\Delta}\right),\quad g(E)=g_0-\frac{4}{3}\frac{m_0P^2}{\hbar^2}\frac{\Delta}{(E_g+E)(E_g+E+\Delta)}. \tag{3}$$

The boundary conditions are the requirement that the spinor $u(r)$ and the components of the vector $Pv(r)$ be continuous in a direction normal to the heterointerface.

We note that $m_c^{-1}(0)$ and the difference $g(0)-g_0$ are, respectively, the contribution of the valence band to the reciprocal of the effective mass and the g factor of an electron at the conduction band bottom, calculated to second order in the *kp* perturbation theory. If the wave function is localized in one of the directions ζ as a result of size quantization, then the first-order perturbation theory in the linear (in the magnetic field) correction to the electronic Hamiltonian can be used to find the g factor in a magnetic field $B\perp\zeta$. This device has been used previously to calculate the transverse g factor in quantum wells.[11] In a structure with a quantum dot, where the wave function is localized in all three directions, the first-order perturbation theory is applicable, and the g-factor tensor $g_{\alpha\beta}$ for the size-quantization ground state $e1$ is given by the expression

$$\frac{1}{2}\mu_B\sigma_{\alpha,ss'}g_{\alpha\beta}B_\beta=\frac{1}{2}g_0\mu_B\sigma_{\alpha,ss'}B_\alpha+\langle e1,s|\delta H|e1,s'\rangle. \tag{4}$$

Here μ_B is the Bohr magneton, σ_α ($\alpha=x,y,z$) are the Pauli matrices, the electron spin projection $s,s'=\pm 1/2$, $\delta H=(e/c)\hat{V}A$ is a perturbation linear in the vector potential $A(r)$, $-e$ is the electron charge, and in the Kane model the velocity operator $\hat{V}=\hbar^{-1}\partial H(k)/\partial k$ is an 8×8 matrix with components that do not depend on k. Formula (4) is also applicable for an electron state at the bottom of the subband $e1$ in a quantum wire if: a) the gauge of the vector potential is chosen so that the potential depends on the coordinates in a plane perpendicular to the principal axis z of the wire, and b) the diamagnetic term[11]

$$\frac{e}{c}\langle e1,s|\hat{v}_z|e1,s'\rangle\langle A_z(\mathbf{r})\rangle,$$

which can be nonzero in the case of low cross-sectional symmetry of the wire, is subtracted out. We note that the average $\langle A_z\rangle \equiv \langle e1,s|A_z|e1,s\rangle$ does not depend on the spin s. Using the explicit form of the matrix $\hat{V}$, we arrive at the basic formula for calculating the g factor:

$$\langle e1,s|\,\delta H|e1,s'\rangle = i\frac{e}{c\hbar}\int P[(\mathbf{A}\cdot\mathbf{v}_s^+)u_{s'} - u_s^+(\mathbf{A}\cdot\mathbf{v}_{s'})]d\mathbf{r}. \tag{5}$$

In the general case the spinor function $u(r)$ can be represented in the form

$$u(\mathbf{r}) = [f(\mathbf{r}) + i\sigma_\alpha h_\alpha(\mathbf{r})]c_s, \quad c_s = \uparrow \text{ or } \downarrow,$$

where $f(r)$ and $h_\alpha(r)$ are real functions. The symmetry of a quantum dot or wire imposes restrictions on the form of these functions. Specifically, in a quantum dot with D_{2d} symmetry (the symmetry of a rectangular parallelepiped or ellipsoid) we have for the electronic ground state $e1$: $f(\mathbf{r}) = f(x^2,y^2,z^2)$, $h_x(\mathbf{r}) = yzM_x(x^2,y^2,z^2)$, $h_y(\mathbf{r}) = zxM_y(x^2,y^2,z^2)$, and $h_z(\mathbf{r}) = xyM_z(x^2,y^2,z^2)$, where M_α are arbitrary functions of x^2, y^2, and z^2. The envelope of the electron wave function in a state with $k_z = 0$ in a quantum wire does not depend on z. For this reason, in a quantum wire with a rectangular cross section $h_x(\mathbf{r}) \equiv h_y(\mathbf{r}) \equiv 0$, $h_z(\mathbf{r}) = xyM_z(x^2,y^2,z^2)$. In a cylindrical wire $f(r) = f(\rho = \sqrt{x^2+y^2})$ and the three functions $h_\alpha(r)$ are identically equal to zero, since combinations which transform as components of a pseudovector under the group $D_{\infty h}$ cannot be constructed from powers of the coordinates x and y. For a similar reason $h_\alpha(r) = 0$ in a spherical quantum dot.

Substituting into Eq. (5) the expression for $u_s(r)$ in the form $f(r)c_s$, we find that the electron g factor is isotropic not only in a spherical quantum dot but also in a cylindrical wire. This unexpected result can be understood without detailed calculations. Indeed, let us choose the gauge $\mathbf{A} = (0,0,-xB_y)$ for the case $\mathbf{B}\perp z$ and the gauge $\mathbf{A} = (0, xB_z, 0)$ for the case $\mathbf{B}\parallel z$. In a cylindrical wire the functions h_α are identically equal to zero, the function f for the ground state does not depend on the azimuthal angle, and the velocity operator in the Kane model is a matrix with constant coefficients; for these reasons, both components of the g factor are proportional to the same integral $\int dxdy f(\rho)x(\partial/\partial x)f(\rho)$, and the coefficients of proportionality do not depend on the dimensions of the wire. Since the g factor is isotropic in the limit $R\to\infty$ (just as in a bulk semiconductor), it is also isotropic for any R.

Substituting the function f into Eq. (5) and integrating by parts, we obtain for a circular wire and a spherical dot

$$g = \eta g_0 + [g_B(E) - g_A(E)]V_{3-d}(R)f^2(R) + [g_A(E) - g_0]w_A + [g_B(E) - g_0]w_B, \tag{6}$$

where V_n is the volume of a n-dimensional sphere ($V_2 = \pi R^2$, $V_3 = 4\pi R^3/3$), $g_A(E)$ and $g_B(E)$ are determined in accordance with Eq. (3), w_A and w_B are integrals of the function f^2 over the region occupied by material A or B (for $v \neq 0$ the sum $w_A + w_B$ is different from 1). The coefficient $\eta \neq 1$ for $E > 0$ on account of mixing of the spin states $\uparrow$ and $\downarrow$, and it can be anisotropic in low-symmetry systems. However, estimates show that, as a rule, its difference from 1 can be neglected. As the radius R increases, the value of w_A approaches 1, and the energy E of the level $e1$, the product $V_{3-d}(R)f^2(R)$, and the

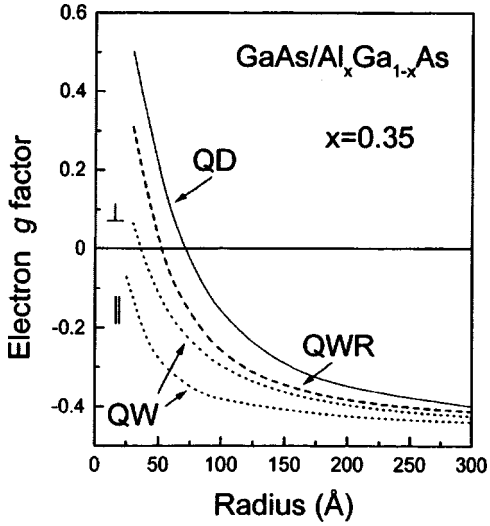

FIG. 1. Electron g factor versus the linear dimensions of a structure in the heterosystem GaAs/$Al_{0.35}Ga_{0.65}As$. The values for a spherical quantum dot and a cylindrical quantum wire with radius R are represented by the solid and dashed lines, respectively. For comparison, the longitudinal and transverse components of the electron g-factor tensor ($g_{\parallel}^{QW}<g_{\perp}^{QW}$) for a single quantum well of thickness $2R$ are also shown (dotted lines).

quantity w_B decrease to zero, so that in the limit $R\to\infty$ the g factor approaches the bulk value in material A according to the law $g(R)=g_A(0)+(R_d/R)^2$; here $R_1<R_0$.

In the present work we calculated the g factor in a spherical quantum dot and a cylindrical wire, where the envelope $f(r)$ for the level $e1$ has, respectively, the form $Cr^{-1}\sin kr$ for $r<R$, $Dr^{-1}\exp[-\kappa(r-R)]$ for $r>R$, and $CJ_0(k\rho)$ for $\rho<R$, $DK_0(\kappa\rho)$ for $\rho>R$. Here R is the radius, $k=[2m_A(E)E/\hbar^2]^{1/2}$, $\kappa[2m_B(E)(\Delta E_c-E)/\hbar^2]^{1/2}$, $J_0(x)$ and $K_0(x)$ are Bessel functions, ΔE_c is the offset of the conduction band at the heterointerface of the two materials (which are designated below as A and B), $m_A(E)$ is the mass $m_c(E)$ determined according to Eq. (3) for material A, the analogous mass $m_B(E)$ is determined for the parameters of material B with allowance for the offset of the bands, i.e., $m_B(E)=m_c(E-\Delta E_c)$, and the coefficients C and D are found from the boundary conditions: continuity of f and of the normal component of the vector $m_c^{-1}(E)\nabla f$, and from the normalization $\int(u^+u+v^+v)dV_{3-d}=1$, where $d=0$ or 1 and dV_n is the volume element in n-dimensional space.

Formula (6) is also applicable for calculating the transverse g factor $g_\perp=g_{xx}=g_{yy}$ for an electron in a quantum well of width $2R$, for which $d=2$, $V_{3-d}=2R$ and in which $f=C\cos kz$ for $|z|<R$ and $D\exp[-\kappa(|z|-R)]$ for $|z|>R$.

Figure 1 displays the electron g factor in a spherical quantum dot (g^{QD}) and a cylindrical wire (g^{QWR}) as a function of the radius R. For comparison, the figure also shows (dotted lines) the values of the longitudinal ($g_{\parallel}^{QW}$, $B\|z$) and transverse ($g_{\perp}^{QW}$, $B\perp z$) g factors for a quantum well of width $2R$. The model calculation was performed for the heterosystem GaAs/$Al_{0.35}Ga_{0.65}As$. The following values of the parameters were used in the calculation: $E_g=1.52$ eV, $\Delta=0.34$ eV, and $2p_{cv}^2/m_0=28.9$ eV for bulk GaAs

($p_{cv}=i\langle S|\hat{p}_z|Z\rangle$), $E_g=1.94$ eV, $\Delta=0.32$ eV, and $2p_{cv}^2/m_0=26.7$ eV for the barrier material, and a ratio of the band offsets at the heterointerface $\Delta E_v:\Delta E_c=2:3$. To take into account the contribution of remote bands, we added the constant $\Delta g=-0.12$ to the values of the g factor obtained in the Kane model. When this is done, the electron g factor reaches the bulk value -0.44 in GaAs as the size of the structure increases. As the linear dimensions of the structure decrease, the g factor increases, approaching in the limit $R\rightarrow 0$ the value 0.57 in the barrier material. Since size-quantization effects play an increasingly larger role as the dimension of the system decreases, the relations $g_{\parallel,\perp}^{QW}<g^{QWR}<g^{QD}$ hold (see Fig. 1). Estimates show that the contribution of the term in Eq. (6) that is proportional to $f^2(R)$ is not small, which rules out an approximation of $g(R)$ in the form $g_A(E)w_A+g_B(E)w_B$.

In summary, using the Kane model we have constructed a theory of the electron g factor in superconductor quantum dots and quantum wires; we have performed a symmetry analysis for a number of specific microstructures and have shown that in contrast to a quantum well, where $g_\parallel\neq g_\perp$, the g factor in a cylindrical wire (a system with the same point symmetry) is isotropic. We have carried out a model calculation for a spherical dot and a cylindrical wire.

We thank the Russian Fund for Fundamental Research and the Volkswagen Foundation for financial support.

[1] L. M. Roth, B. Lax, and S. Zwerdling, Phys. Rev. **114**, 90 (1959).
[2] E. L. Ivchenko and A. A. Kiselev, Fiz. Tekh. Poluprovodn. **26**, 1471 (1992) [Sov. Phys. Semicond. **26**, 827 (1992)].
[3] E. L. Ivchenko, V. P. Kochereshko, I. N. Uraltsev, and D. R. Yakovlev, in *High Magnetic Fields in Semiconductor Physics*, edited by G. Landwehr, Springer Series in Solid-State Science (1992), Vol. 101, p. 533.
[4] V. K. Kalevich and V. L. Korenev, JETP Lett. **56**, 253 (1992).
[5] B. Kowalski, P. Omling, B. K. Meyer *et al.*, Phys. Rev. B **49**, 14786 (1994).
[6] R. M. Hannak, M. Oestreich, A. P. Heberle *et al.*, Solid State Commun. **93**, 313 (1995).
[7] A. A. Sirenko, T. Ruf, K. Eberl *et al.*, in *High Magnetic Fields in Semiconductor Physics*, edited by G. Landwehr and W. Ossau, World Scientific, 1996, p. 561.
[8] P. Le Jeune, D. Robart, X. Marie *et al.*, Semicond. Sci. Technol. **12**, 380 (1997).
[9] A. A. Sirenko, T. Ruf, and M. Cardona, Phys. Rev. B **56**, 2114 (1997).
[10] A. A. Sirenko, T. Ruf, A. Kurtenbach, and K. Eberl, in *Proc. ICPS-23*, Berlin 1996, World Scientific, 1996, p. 1385.
[11] E. L. Ivchenko, A. A. Kiselev, and M. Willander, Solid State Commun. **102**, 375 (1997).

Translated by M. E. Alferieff

Self-organization of germanium nanoislands obtained in silicon by molecular-beam epitaxy

V. Ya. Aleshkin, N. A. Bekin, N. G. Kalugin, Z. F. Krasil'nik,[a)]
A. V. Novikov, and V. V. Postnikov
Institute of Physics of Microstructures, Russian Academy of Sciences, 603600 Nizhniĭ Novgorod, Russia

H. Seyringer
Institute for Semiconductor Physics, Johanes Kepler University of Linz, Linz, Austria

(Submitted 2 December 1997)
Pis'ma Zh. Éksp. Teor. Fiz. **67**, No. 1, 46–50 (10 January 1998)

Nanometer germanium islands in epitaxial layers of silicon are obtained by molecular-beam epitaxy. The dimensions and shapes of the islands are determined in an atomic-force microscope. The photoluminescence spectra are found to contain lines that can be interpreted as quasidirect optical transitions in the islands. It is concluded on the basis of optical and microprobe measurements and theoretical calculations of the energies of electronic states that silicon is dissolved in the germanium islands. Values of the germanium and silicon contents in the solid solution are presented. © *1998 American Institute of Physics.* [S0021-3640(98)00901-3]

PACS numbers: 81.15.Hi, 81.05.Cy, 78.55.Ap

In the present letter we study the physical properties of nanometer germanium islands obtained in silicon in the process of molecular-beam epitaxy. Island formation under certain conditions of epitaxial growth of elastically strained atomic layers of germanium on silicon is connected with the process of self-organization of islands in accordance with the Stranskiĭ–Krastanov mechanism.[1] In the last few years a large number of works have been devoted to the processes of self-organization of Ge islands in epitaxial layers of Si.[1–5] Such great interest in these objects has apparently been engendered, to some degree, by the rapidly developing investigations of quantum dots in strained heterostructures on the basis of III–V materials, as a result of which the understanding of the growth of self-organizing structures, the physical properties of objects with zero-dimensional density of states, and the applied aspects of the application of structures with arrays of quantum dots is now well developed.

The basic conditions for the formation of self-organizing islands of germanium in silicon in the process of epitaxial growth in a high vacuum[2,3] or in a gaseous medium at atmospheric or low pressure[4,5] have now been determined. In contrast to III–V quantum dots, germanium islands have large dimensions in the growth plane and the electronic spectrum of the charge carriers in them is two-dimensional. The dimensions of the islands and their packing density in the growth plane depend strongly on the substrate temperature and the Ge and Si deposition rates.[2] Questions concerning deformation and disloca-

tions in islands, the shape of the islands, the solubility of silicon and the formation of the solid solution SiGe in them, the spectra of electronic states and optical transitions, and other features remain open. The present letter is devoted to clarifying some of these questions.

The experimental structures were grown in a ''Balzers'' apparatus that had been modernized for molecular-beam epitaxy of Si/Ge heterostructures. The residual-gas pressure in the growth chamber did not exceed 5×10^{-10} mbar and the working pressure did not exceed 2×10^{-8} mbar. Silicon and germanium were evaporated from sources by electron beams. Plates of *p*-type Si(100) were used as substrates. The structures were grown at two substrate temperatures $T_g=550$ °C and 700 °C. The substrate surfaces were precleaned by thermal etching at $T=1150$ °C. Two types of structures were grown. Structures intended for analysis with an atomic-force microscope (AFM) contained a 225 nm thick silicon buffer layer on which a germanium layer, consisting of 2 to 10 monolayers (1 monolayer = 1.4 Å), and a 40–50 Å silicon layer were deposited successively. For photoluminescence measurements, a ten-period lattice of alternating germanium layers, consisting of 2–7.8 monolayers, and a 500 Å thick silicon layer was grown on a 500 nm thick buffer. The growth rates of the Si and Ge layers were equal to 2 Å/s and 0.05 Å/s, respectively. Prior to the Ge growth onset, the Si growth rate was decreased to 0.5 Å/s in order to decrease the roughness of the heterointerface. It will be shown below that as a result of internal elastic stresses, which arise as a result of the mismatch of the Si and Ge lattice periods, the germanium layer transformed into islands when the thickness exceeded of the order of 3–4 monolayers. For this reason, the germanium layer thicknesses $>3-4$ monolayers reported here and below are nominal values — a layer of such thickness would have been deposited on the substrate in accordance with the source evaporation rate and time if the islands had not formed.

Silicon structures with germanium were examined with a ''Park Scientific Instrument'' AFM under room conditions. Figure 1 displays an AFM photograph of a sample with Ge-layer thickness $d_{\mathrm{Ge}}=10$ monolayers, grown at $T_g=700$ °C. According to microprobe data, the critical Ge-layer thickness (d_c) above which self-organization of islands occurs is $d_c=4.5$ Å (3.2 monolayers) under our growth conditions. As the amount of Ge deposited increases, the sizes of the islands and their concentration increase. The islands can be divided into three groups according to the transverse dimensions D: $D\leqslant190$ nm, $200\leqslant D\leqslant300$ nm, and $D\geqslant350$ nm. Judging from the dimensions and shape of the islands in the first and second groups, these are apparently elastically strained dislocation-free islands, in which partial relaxation of elastic stresses has occurred as a result of local deformation of a surface layer of silicon[1] and relaxation of stresses on the free surface of the islands. The third group consists of islands which have undergone plastic relaxation of elastic stresses as a result of the formation of misfit dislocations in them. The size of the islands in the growth plane for which formation of dislocations occurs is close to the critical size of the elastically strained islands $D>300$ nm, measured in Ref. 5.

The surface density N_s of the islands depends on the Ge-layer thickness and for different amounts of deposited germanium fluctuates from 8×10^7 cm^{-2} to 2×10^9 cm^{-2}. Decreasing the growth temperature to 550 °C gives a more uniform size distribution of the islands, decreases their average size ($D\approx190$ nm), and increases the surface

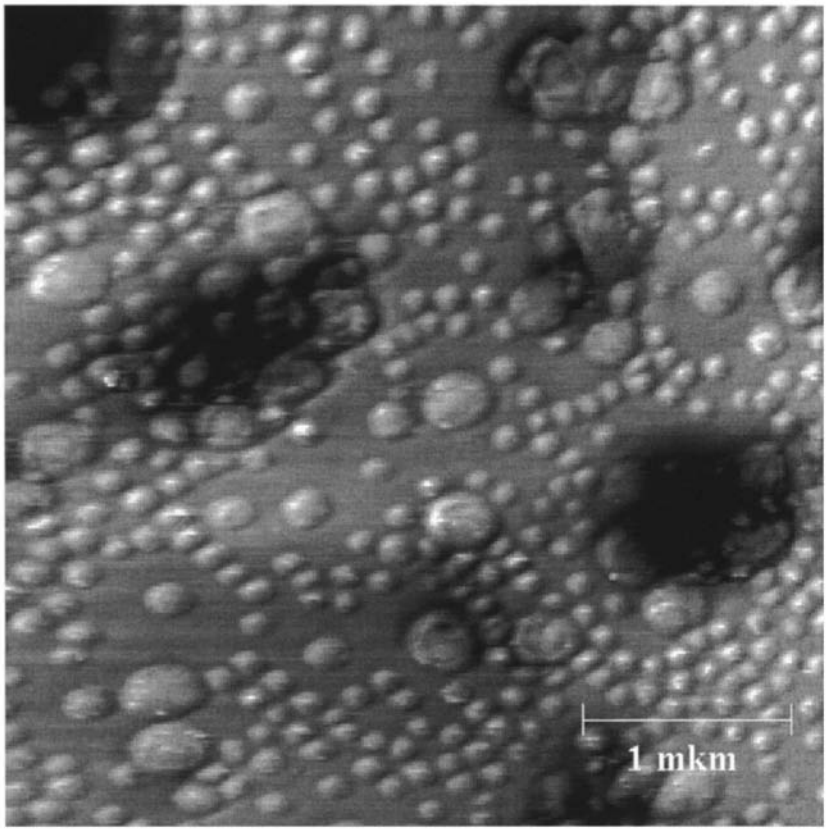

FIG. 1. AFM photograph of a sample grown at $T_g = 700$ °C with $d_{Ge} = 10$ monolayers.

density. The data on the sizes and density of self-organized islands agree with the results of Ref. 2.

The photoluminescence spectra of Si/Ge structures were measured at 4 K with a resolution of 0.5 meV on a ''Boem'' DA3-36 Fourier spectrometer with a cooled InGaAs photodetector (see Fig. 2). The spectra were obtained by excitation with a Kr^+ laser ($\lambda = 647$ nm). Besides the luminescence lines of the silicon substrate (phonon replicas with participation of optical TO and acoustic TA phonons (see Fig. 2)), luminescence associated with a wetting Ge layer (2D) is observed in the spectra of samples with an effective germanium layer $\leqslant 5$ monolayers (with participation of TO phonons — TO_{2D} and a phonon-free line NP_{2D}). For the $d_{Ge} = 2$ monolayers sample the NP_{2D} line falls in the range of the phonon lines $(TO + 2TA)_{Si}$ of the substrate luminescence. As the amount of deposited germanium increases, the photoluminescence lines associated with the germanium layer shift to lower energies as a result of the size-quantization effect. The position of the lines from the wetting layer agrees well with the computed values.

For Ge-layer thickness greater than a critical value, a wide peak is observed in the

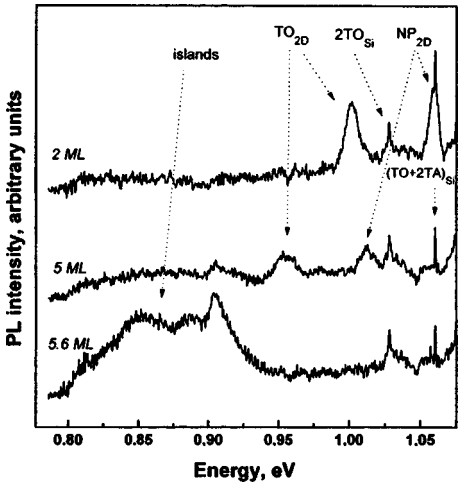

FIG. 2. Photoluminescence spectra of structures grown at $T_g = 700$ °C with different Ge-layer thicknesses.

critical region 0.8–0.925 eV. This emission band is attributed to the formation of Ge nanoislands.

The characteristic dimensions of the islands in the growth plane exceed 10^3 Å. Their height is approximately an order of magnitude smaller. For such dimensions, the energy associated with size-quantization effects for holes in Ge islands would no exceed 20 meV and therefore the strong shift in the energy range 800–925 meV of the wide photoluminescence band relative to the silicon radiation cannot be attributed unequivocally to purely germanium islands in silicon. It can be assumed that the islands consist of a solid solution of germanium with silicon,[2] and then the molar fraction of silicon in them can be estimated.

Figure 3 shows the positions of the band edges of the thin homomorphic solid solution $Si_{1-x}Ge_x$ on Si, calculated using the model of Ref. 6. The symbols *hh* and *lh* denote heavy- and light-hole bands; 2Δ denotes two delta valleys of the conduction bands where the electron masses are highest in the direction of growth; 4Δ are the remaining four delta valleys of the conduction band; and, L is a L valley. The calculations show that the photoluminescence in the energy range 800–925 meV in a homomorphically grown solution on a silicon substrate is possible if the germanium fraction in the islands ranges from 30 to 50%. The formation of a solution in islands is apparently associated with the segregation of germanium.

Since the structures possess *p*-type conductivity and the islands are potential wells for holes, the holes accumulate in the islands, charging them positively. The surface density of holes in islands for volume hole density in Si $\sim 10^{15}$ cm^{-3} can be estimated, just as for a quantum well with the same energy level of the heavy-hole ground state, as $\sim 4\times 10^{10}$ cm^{-2} (see, for example, Ref. 7). As a result of Coulomb repulsion, holes inside islands must concentrate along the heterointerfaces. The positive charge of the islands produces a quantum well for photoelectrons in silicon near a heterojunction (see inset in Fig. 3). In the case when the conduction band bottom in silicon is lower than in

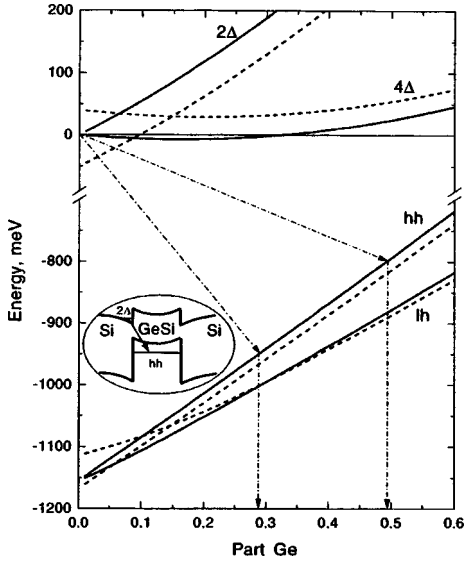

FIG. 3. Calculation of the conduction and valence bands of the solid solution $Si_{1-x}Ge_x$ grown homomorphically on a Si(100) substrate (lattice constant — 5.43 Å, solid lines). The dashed line corresponds to the elastically strained silicon (lattice constant — 5.46 Å). Inset: Band diagram for the case when $x>0.32$.

the islands (in Fig. 3 one can see that this occurs for $x>0.32$, the photoluminescence energy $E_{pl}<960$ meV), on account of size quantization in this well the ground states are the states of the 2Δ valleys because of the large, compared with the 4Δ valleys, masses in the (001) direction. Here, electrons located near the base and top boundary of the islands are primarily studied, since these electrons make the main contribution to the photoluminescence because of the large difference in the areas of the lateral sides and bases. As a result of size quantization, the electron quasimomentum perpendicular to the heterointerfaces is no longer conserved (the Brillouin zone is two-dimensional) and the states of electrons in the 2Δ valleys are displaced into the center of the two-dimensional Brillouin zone. In this case the interband optical transitions are direct in momentum space $(\mathbf{p}_{\text{final}}-\mathbf{p}_{\text{initial}}=0)$,[6] but in the coordinate space the transitions are indirect, since the electrons and holes are localized on different sides of the heterointerface. This is probably the reason why the photoluminescence is weak.

As to the influence of the island sizes, the large width of the luminescence line associated with the presence of islands is apparently determined not so much by the variance in the island sizes, as happens for self-organized InAs/GaAs quantum dots,[8] as by the nonuniform distribution of germanium and silicon valleys in the islands and the different degree of relaxation of elastic stresses. This is probably the reason why the position of the strongly broadened photoluminescence line associated with islands is insensitive to the island size.

If it is assumed that partial relaxation of elastic stresses in the solid solution has occurred as a result of the deformation of the surrounding silicon, then according to the calculations the fraction of the germanium in the islands whose photoluminescence falls

into the energy range 0.8–0.925 eV should decrease compared with the islands where such relaxation has not occurred. This conclusion can be drawn by analyzing Fig. 3, where the dashed lines represent the positions of the band edges in the solid solution in the case when the silicon layers surrounding it are deformed.

We thank A. Yu. Andreev for organizing the AFM measurements. This work was supported by Russian Fund for Fundamental Research Grant 96-02-16991 and Project 96-2011 of the Interdisciplinary Science and Technology Program ''Physics of Solid-State Nanostructures.''

[a)]e-mail: zfk@ipm.sci-nnov.ru

---

[1]G. Abstreiter, P. Schittenhelm, C. Engel *et al.*, Semicond. Sci. Technol. **11**, 1525 (1996).
[2]D. J. Eaglesham and M. Cerullo, Phys. Rev. Lett. **64**, 1944 (1990).
[3]D. J. Eaglesham, F. C. Unterwald, and D. C. Jacobson, Phys. Rev. Lett. **70**, 966 (1993).
[4]Y. Shiraki, H. Sunamura, N. Usami *et al.*, Appl. Surf. Sci. **102**, 269 (1996).
[5]G. Capellini, L. Di Gaspare *et al.*, Appl. Phys. Lett. **70**, 494 (1997).
[6]V. Aleshkin and N. A. Bekin, J. Phys.: Condens. Matter **9**, 4841 (1997).
[7]V. Ya. Aleshkin, A. A. Kostin, and Yu. A. Romanov, Fiz. Tekh. Poluprovodn. **26**, 318 (1992) [Sov. Phys. Semicond. **26**, 179 (1992)].
[8]M. Grundman, J. Christen, N. N. Ledentsov *et al.*, Phys. Rev. Lett. **74**, 4043 (1995).

Translated by M. E. Alferieff

Decay of mesoscopically localized vibrations in porous materials

V. L. Gurevich
Institut für Festkörperforschung, Forschungszentrum Jülich, D-52425 Jülich, Germany; A. F. Ioffe Physicotechnical Institute, 194021 St. Petersburg, Russia

H. R. Schober
Institut für Festkörperforschung, Forschungszentrum Jülich, D-52425 Jülich, Germany

(Submitted 2 December 1997)
Pis'ma Zh. Éksp. Teor. Fiz. **67**, No. 1, 51–56 (10 January 1998)

The low-temperature decay of a vibrational eigenstate of a crystalline mesoscopic particle surrounded by other such particles of approximately the same size is considered. The decay time is determined by the anharmonicity and the coupling between adjacent mesoscopic particles. Under some limiting conditions for particles of a typical size of 50 Å the decay time at low temperatures can be several milliseconds.
 [S0021-3640(98)01001-9]

PACS numbers: 63.20.Pw, 53.50.+x, 61.43.Gt

In a recent paper by Kaplyanskii, Feofilov, and Zakharchenya,[1] long-lived size-quantized vibrational states in porous Al_2O_3 were studied at low temperatures between 2 and 5 K. Nonequilibrium phonons were excited by ''optical heating'' with a laser pulse. The anti-Stokes spectrum was observed at long time delays of 2–4 ms, and a low-frequency maximum at $\omega_0 \approx 20$ cm^{-1} was found to decay for ~ 1 ms. The purpose of the present letter is to provide a theory of the decay rate of such vibrational states which might shed light on the origin of the exceptionally long decay times observed in the experiment.

The physics of the phenomenon can be described as follows. The sample of Al_2O_3 consists of particles of approximately (but not exactly) the same size, about 50 Å in diameter, and which are presumably only weakly connected, i.e., most of the bonds on the surface of a particle are dangling. Although some of the particles might constitute ''dead ends'' and others can be connected with several neighbors, most of the particles' surfaces can still be considered as free.

Due to the small dispersion of the mesoscopic crystal sizes and the comparatively large density, our system is distinct from typical aerogels.[2] In these the typical lengths may vary by some orders of magnitude, leading to fractal behavior.[3] It is equally distinct from a glass.[4] There one has only one length scale, the atomic one.

We consider porous materials, in which two length scales exist. In addition to the microscopic scale (set by the interatomic distance), the nanocrystal size provides a second, mesoscopic scale. We suggest that the novel type of solids investigated in Ref. 1 belongs to this type. We assume that there is nearly perfect order inside the single particles on atomic scales. On the mesoscopic scale, we envisage the material to be built

from single-crystal particles. The comparatively large density and the small variation of the particle sizes will ensure some interparticle short-range order. One should not expect any long-range order.

Corresponding to this structure we expect two types of vibrations. The intraparticle vibrations are determined by the interatomic forces, and their wavelengths are limited by the particle size. In first approximation these states can be described as isolated particles with free surface boundary conditions. We will provide an algorithm for the calculation of the lifetimes of the lowest-frequency modes. These can indeed be very long. In addition to these modes there are interparticle vibrations, whose wavelengths are larger than the typical particle size and whose frequencies are determined by the much weaker interparticle coupling. The two types of vibrations interact. The strength of the interaction is proportional to the ratio between interparticle and interatomic coupling. We consider the case where this is sufficiently small.

The material is characterized by a narrow distribution of particle diameters. We further assume a coupling between the crystallites so weak that there is a gap between the respective spectra of the intra- and interparticle vibrations. The average density is in the range of 30% to 50% of the crystalline density, and the typical diameter of the crystallites and the pores between them is 50 Å.

First we consider an isolated crystallite. There will be of the order of 1000–10000 atoms in a crystallite, which allows the use of continuum theory to estimate the lowest eigenfrequencies. The vibrations of a homogeneous spherical body were calculated by Lamb[5] and by Tamura *et al.*,[6] who give for the lowest eigenfrequency $\omega_{\min} \approx 2.5 v^{\text{crystal}}/R$. Here v^{crystal} is the average transverse sound velocity in the crystalline material and R the radius of the particle. The corresponding eigenmode is mostly concentrated on the surface of the particle. Such modes have been observed, e.g., by Raman scattering on nucleated glass.[7]

The long-wavelength dynamics and elastic behavior of polycrystalline and similar materials is a long-standing problem (see, e.g., Refs. 8–10). For our purpose a simple estimate is sufficient. In aerosols one observes a scaling of the sound velocity with the density ρ: $\overline{v} \propto \overline{\rho}^{1.4}$ (Ref. 11), where the bar indicates an average over the sample. We expect a similar dependence for the porous material considered here. Taking the relation $\overline{v} = \sqrt{\overline{C}/\overline{\rho}}$, we find $\overline{C} \propto \overline{\rho}^{3.8}$, where $\overline{C}$ and $\overline{\rho}$ are the averaged elastic constant and mass density, respectively. Since the interatomic bonds inside the crystallites will not be affected strongly by porosity, the elastic weakening reflects the weak bonding between the crystallites. The elastic constants are determined by the stiffness and number of bonds. The reduction of $\overline{C}$ by more than a factor 10 reflects a similar reduction in the number of bonds between the crystallites.

Regarding elastic waves (with wavelengths much larger than the interparticle distance) the porous material can be considered as an elastic medium whose properties are characterized by the average density $\overline{\rho}$ and average elastic moduli $\overline{C}_{ilmn}$, the averaging being over length scales much larger than the interparticle distance. Alternatively one can look upon the problem from an equivalent point of view. To a good approximation the harmonic dynamics of elastic waves in the porous material can be described by weakly coupled rigid particles. In this amorphous lattice of crystallites the diameter $2R$ will take

the role of the lattice constant inside the particles. The maximum frequency of the acoustic waves is then $\omega(q_{\max}) \approx \pi \overline{v}/R$.

We consider the case $\omega_{\min} > \omega(q_{\max})$ and further stipulate that the relative spread, due to variations of diameter and shape, of the lowest intra particle vibration frequencies is larger than the *linear* coupling between these modes in adjacent crystallites. This means that the modes in the adjacent crystallites are entirely *out of resonance*. Then the eigenmodes of the crystallites are localized in the true sense of harmonic lattice theory. Their amplitudes will decay exponentially in space into the adjoining material, and the larger the difference between the two eigenfrequencies, the faster this decay will be. As they are true eigenmodes their time dependence is harmonic. This means that if one neglects anharmonicity *they do not decay in time at all*. If one treats the site-diagonal disorder as a perturbation one can get a lifetime as the imaginary part of the phonon self-energy. As is well known, this lifetime would be spurious, as such an imaginary part would not correspond to any attenuation. It is due only to the fact that in the presence of disorder a phonon wave vector is a poor quantum number.

Thus the lifetimes of the local vibrations are determined by anharmonicity. We consider low temperatures, where in thermal equilibrium the occupation numbers of the phonons are essentially zero and transitions are dominated by phonon emission. We will show that, compared to typical crystalline samples, the anharmonic effects are so strongly reduced that the lifetimes of the low-frequency localized vibrations become extremely long.

The elastic displacement within an isolated particle ℓ corresponding to the lowest eigenstate is given by[12]

$$u_i(\mathbf{r}) = \sqrt{\frac{\hbar}{2\omega_\ell \rho \mathcal{V}}}(c_\ell + c_\ell^\dagger) f_i^{(\ell)}(\mathbf{r}), \tag{1}$$

where c_ℓ and $c_\ell^\dagger$ are the annihilation and creation operators of the lowest eigenmode in particle ℓ, and ρ is the mass density of the crystallites. The eigenfunctions $\mathbf{f}^{(\ell)}(\mathbf{r})$ satisfy the equations of elasticity theory and the normalization condition

$$\frac{1}{\mathcal{V}} \int_{\mathcal{V}} d^3 r [\mathbf{f}^{(\ell)}]^2 = 1 \tag{2}$$

with $\mathcal{V}$ the volume of the particle. The Hamiltonian of particle ℓ is

$$H_\ell = \hbar \omega^{(\ell)} (c_\ell^\dagger c_\ell + 1/2).$$

Consider two adjacent particles, 1 and 2, which are weakly harmonically coupled. The coupling Hamiltonian is

$$H_{12} = \eta \hbar \sqrt{\omega_1 \omega_2} (c_1^\dagger c_2 + c_2^\dagger c_1) \tag{3}$$

where $\eta \ll 1$. The eigenfrequencies of the two particles will not differ strongly and

$$|\omega^{(1)} - \omega^{(2)}| / \omega^{(1)} \ll 1. \tag{4}$$

In places such as Eq. (3) we need not discriminate between $\omega^{(1)}$ and $\omega^{(2)}$ and we will replace them by some average value $\tilde{\omega}$. In order to make perturbation theory applicable the interparticle coupling has to obey the inequality

$$\eta \frac{\tilde{\omega}}{|\omega^{(1)}-\omega^{(2)}|} \ll 1. \tag{5}$$

In this limit the localized vibrational states of the two particles mix only weakly. Indeed, the vibrational amplitude, which is normalized to unity within particle 1, acquires an extra small factor (5) in particle 2, etc.

We take $\omega^{(1)}>\omega^{(2)}$. Then an excitation in particle 1 can decay into one in particle 2 by passing the surplus energy to a traveling acoustic wave with frequency $\omega_{\mathbf{q}}=\overline{v}q$:

$$\omega^{(1)}=\omega^{(2)}+\omega_{\mathbf{q}}. \tag{6}$$

The energy density for the anharmonic interaction, $\mathcal{E}$ can be written as[6]

$$\mathcal{E}=\frac{1}{6}\sum_{\substack{abc\\ilm}} C^{(3)}_{ialbmc}u_{ai}u_{bl}u_{cm},$$

where $u_{ai}=\partial u_a/\partial x_i$ and $C^{(3)}_{ialbmc}$ is the tensor of anharmonic moduli of third order, which are usually somewhat larger numerically than the harmonic moduli.

The matrix element of the process described by Eq. (6) is

$$\langle(1)|\mathcal{E}|(2),\mathbf{q}\rangle=\frac{1}{6}\sum_{\substack{abc\\ilm}} C^{(3)}_{ialbmc}\int d^3r\langle(1)|u_{ai}u_{bl}u_{cm}|(2),\mathbf{q}\rangle, \tag{7}$$

where

$$|(1)\rangle=c_1^\dagger|0\rangle, \quad |(2),\mathbf{q}\rangle=c_2^\dagger c_{\mathbf{q}}^\dagger|0\rangle$$

and $|0\rangle$ is the vacuum state with no phonons excited. To estimate the anharmonic interaction within particle 1 we write

$$\mathbf{u}=\mathbf{u}^{(1)}+\mathbf{u}^{(2)}+\mathbf{u}^{(\mathrm{ph})},$$

where the displacement due to the traveling acoustic phonon is

$$\mathbf{u}^{(\mathrm{ph})}=\sqrt{\frac{\hbar}{2\overline{\rho}\mathcal{V}_N}}\sum_{\mathbf{q}}\frac{1}{\sqrt{\omega_{\mathbf{q}}}}\mathbf{e}(\mathbf{q})\exp(i\mathbf{q}\cdot\mathbf{r})(c_{\mathbf{q}}+c_{-\mathbf{q}}^\dagger). \tag{8}$$

Summation over the acoustic branches with polarization vectors $\mathbf{e}(\mathbf{q})$ is implied. Unlike the particle volume $\mathcal{V}$ in Eq. (1), $\mathcal{V}_N$ is a normalization volume which drops out of the final result.

The local displacement of particle 1 now has, in addition to Eq. (1), a term given by Eq. (3) describing the ''leakage'' of the vibrational state $\omega^{(2)}$ from particle 2 into particle 1:

$$\mathbf{u}^{(1)}=\sqrt{\frac{\hbar}{2\omega_1\rho\mathcal{V}_1}}\mathbf{f}^{(1)}(\mathbf{r})\left[(c_1+c_1^\dagger)+\eta\frac{\tilde{\omega}}{\omega^{(1)}-\omega^{(2)}}(c_2+c_2^\dagger)\right]. \tag{9}$$

For $\mathbf{u}^{(2)}$ we have the same equation with the replacement $1\leftrightarrow 2$. Inserting Eqs. (9) and (8) into Eq. (7), we get after the integration

$$\langle(1)|\mathcal{E}|(2),\mathbf{q}\rangle=i(\mathcal{E}^{(1)}+\mathcal{E}^{(2)})\langle(1)|c_1^\dagger c_2 c_{\mathbf{q}}|(2),\mathbf{q}\rangle, \tag{10}$$

where $\mathcal{E}^{(1)}$ and $\mathcal{E}^{(2)}$ are the results of integration over volumes $\mathcal{V}_1$ and $\mathcal{V}_2$, respectively, and

$$\mathcal{E}^{(1)}=\eta\frac{\hbar}{2\rho}\sum_{\mathbf{q}}\sqrt{\frac{\hbar}{2\overline{\rho}\omega_{\mathbf{q}}\mathcal{V}}}\frac{1}{\omega^{(1)}-\omega^{(2)}}\sum_{cm}b_{mc}^{(1)}e_c q_m$$

with

$$b_{mc}^{(1)}=\sum_{\substack{ab\\il}}\frac{1}{\mathcal{V}_1}C_{ialbmc}^{(3)}\int_{\mathcal{V}_1}d^3r\frac{\partial f_a^{(1)}}{\partial x_i}\frac{\partial f_b^{(1)}}{\partial x_l}\exp(i\mathbf{q}\cdot\mathbf{r}).$$

Again the equation for $\mathcal{E}^{(2)}$ is obtained by interchanging $1\leftrightarrow 2$. As qL (where L is the diameter of the particle) is assumed to be small, we replace the factor $\exp(i\mathbf{q}\cdot\mathbf{r})$ by 1.

Now the decay probability of the vibration in particle 1 can be calculated by Fermi's golden rule. Summing over $\mathbf{q}$ one gets

$$\Gamma=\frac{\pi\eta^2\hbar}{4\rho^2\overline{\rho}}\left\langle\left(\sum_{cm}b_{mc}n_m e_c\right)^2\right\rangle_\Omega\int\frac{d^3q}{(2\pi)^3}\frac{q^2}{\omega_{\mathbf{q}}^3}\delta(\omega^{(1)}-\omega^{(2)}-\omega_{\mathbf{q}}),$$

where $\mathbf{n}=\mathbf{q}/q$ and $\langle\ldots\rangle_\Omega$ denotes the average over the solid angle of directions $\mathbf{n}$.

Not knowing the exact dependence of the sound velocity $\overline{v}$ on the average density we assume as a rough estimate, in analogy to the aerogels,[11] that $\overline{\rho}\propto\overline{v}$, neglecting the observed small deviations from proportionality. Introducing the density ratio $\alpha=\overline{\rho}/\rho$, we get

$$\Gamma=\frac{\eta^2\hbar\omega_{\mathbf{q}}}{8\pi\alpha^6\rho^3 v^5}\left\langle\left(\sum_{cm}b_{mc}n_m e_c\right)^2\right\rangle_\Omega. \tag{11}$$

For the orientational average we apply the estimate

$$\left\langle\left(\sum_{cm}b_{mc}n_m e_c\right)^2\right\rangle_\Omega\approx\zeta^2\rho^2 v^4\left(\frac{\pi}{L}\right)^4.$$

Here we have made use of the fact that the cubic anharmonic moduli are roughly of the same order as the harmonic ones. The factor ζ represents their ratio, which may be several times unity. Finally we get the following approximate value for the decay constant:

$$\Gamma\approx\mathcal{N}\frac{\overline{\eta^2}\pi^3\zeta^2\hbar\overline{\omega_{\mathbf{q}}}}{8\alpha^6\rho v L^4}. \tag{12}$$

Here $\overline{\omega_{\mathbf{q}}}$ is the average positive frequency difference $\omega^{(1)}-\omega^{(2)}$, $\mathcal{N}$ is the number of neighbors to which the particle of interest is connected by chemical bonds and whose lowest eigenfrequencies $\omega^{(\prime)}$ are smaller than $\omega^{(1)}$, and $\overline{\eta^2}$ is the mean squared coupling constant to these neighbors. $\mathcal{N}$ can vary between 1 and a dozen.

From Eq. (12) one can get a rough estimate of the limits to be expected for the decay constant Γ. Let us assume the following values for the parameters: $\overline{\eta^2}=10^{-3}$; $\alpha^6=10^{-2}$ (cf. Ref. 1); $\overline{\omega_{\mathbf{q}}}=10^{11}\mathrm{s}^{-1}$; $\rho=5$ g/cm^3; $v=2\times10^5$ cm/s; $L=5\times10^{-7}$ cm, and ζ^2 can have a typical value of several times unity. In particular depending on the value of $\mathcal{N}$ we thus get Γ values of about 10^3–10^4 s^{-1} as observed in the experiment.[1]

There are some major sources of ambiguities in such an estimate. The relative interparticle strength $\overline{\eta^2}$ may be larger than 10^{-3}. It would be helpful to develop methods for its experimental determination. Measurements of the elastic constants and sound velocities of the porous sample would provide a more reliable estimate. The spread in the eigenfrequencies $\overline{\omega_{\mathbf{q}}}$ can, in principle, be determined by a careful optical investigation.

It is necessary to check the validity of the relation $\overline{\rho}\propto\overline{v}$. A lot could be learned from an investigation of the form of the particles constituting the sample and from their relative spatial arrangement. (We are not giving estimates for a rather rare case where all the adjacent particles have frequencies larger than $\omega^{(1)}$. For such particles the decay constant would be proportional to η^4 rather than to η^2.)

Simultaneous measurements of the average mass density $\overline{\rho}$ and the average sound velocity $\overline{v}$ should help towards an understanding of the weak attenuation of the eigenmodes in the mesoscopic crystallites. Each of these crystallites should have its own decay rate because of differences in the sizes and in the harmonic coupling constants, numbers of neighbors, etc. The observation of a nonexponential overall decay[1] is therefore not surprising.

In summary, we have calculated the low-temperature decay rate of an ultrasonic vibration in a mesoscopic crystalline particle weakly coupled to one or several other such particles of approximately the same size. The decay time depends on the width of the particle size distribution and on the strengths of the harmonic and anharmonic couplings. Under the given limiting conditions for particles of a typical size of 50 Å the decay times may be as large as several milliseconds.

We are grateful to A. A. Kaplyanskii for discussing his experimental work[1] and to U. Buchenau for very interesting comments. V. L. G. wishes to express his gratitude to the Institut für Festkörperforschung, Forschungszentrum Jülich for the hospitality extended to him while the work on this paper was done, and to the Alexander von Humboldt Foundation for financial support.

[1] A. A. Kaplyanskii *et al.*, Opt. Spektrosk. **79**, 709 (1995) [Opt. Spectrosc. **79**, 653 (1995)].
[2] J. Fricke (ed.), *Aerogels*, Vol. 6 of Springer Proceedings in Physics, Berlin: Springer, 1986.
[3] T. Nakayama and K. Yakubo, Rev. Mod. Phys. **66**, 381 (1994).
[4] *Amorphous Solids – Low Temperature Properties*, Ed. W. A. Phillips, Berlin: Springer, 1981.
[5] H. Lamb, Proc. Math. Soc. London **13**, 187 (1882).
[6] A. Tamura *et al.*, J. Phys. C **15**, 4975 (1982).
[7] E. Duval, A. Boukenter, and B. Champagnon, Phys. Rev. Lett. **56**, 2052 (1986).

[8] W. Voigt, Ann. Phys. **33**, 573 (1889).
[9] A. Reuss, Z. Angew. Math. Mech. **9**, 49 (1929).
[10] R. Zeller and P. H. Dederichs, Phys. Status Solidi B **55**, 831 (1973).
[11] E. Courtens, J. Pelous, J. Phalippou *et al.*, Phys. Rev. Lett. **58**, 128 (1987).
[12] A. A. Maradudin *et al.*, *Theory of Lattice Dynamics in the Harmonic Approximation*, New York: Academic Press, 1971.
[13] L. D. Landau and E. M. Lifshitz, *Theory of Elasticity*, 3rd Ed., New York–Oxford: Pergamon Press, 1986.

Published in English in the original Russian journal. Edited by Steve Torstveit.

RF-photon induced Mössbauer satellites in permalloy

A. Ya. Dzyublik,[a)] V. Yu. Spivak, R. A. Manapov, and F. G. Vagizov
Institute of Nuclear Studies, 252028 Kiev, Ukraine; Kazan Physicotechnical Institute, 420029 Kazan, Tatarstan, Russia

(Submitted 14 July 1997; resubmitted 2 December 1997)
Pis'ma Zh. Éksp. Teor. Fiz. **67**, No. 1, 57–61 (10 January 1998)

The Mössbauer spectra of a permalloy film placed in an rf magnetic field are measured. The film is so thin that transverse magnetostriction oscillations are not excited in it. This permits the observation of satellites that are due solely to periodic variations of the magnetic field at the nucleus. The data are in good agreement with calculations performed in the model of step-wise field reversals. On application of an additional static magnetic field the splitting of the satellites is observed, as predicted by the model of asymmetric step-wise field reversals. [S0021-3640(98)01101-3]

PACS numbers: 76.80.+y, 75.80.+q

Many Mössbauer experiments (see the reviews[1–4]) are devoted to the investigation of soft ferromagnets in a radio-frequency (rf) magnetic field with angular frequency Ω. Equidistant (separated by an interval Ω) satellites, which are split if the quadrupole interaction is also strong, were observed in these experiments. At high frequencies Ω these spectra collapse into a single line or doublet. The main idea forming the basis of the model of step-wise field reversals is that the magnetic field $\mathbf{h}(t)$ at a nucleus in a soft ferromagnet placed in an rf field $\mathbf{H}_{\rm rf}(t)$ jumps periodically between two values $+\mathbf{h}_0$ and $-\mathbf{h}_0$. The corresponding equations for the absorption cross section are derived in Refs. 5–7.

The reversals can be simply explained as follows (see also Ref. 8). It is known[9,10] that soft ferromagnets have a cluster structure. Such weakly interacting clusters behave similarly to superparamagnetic particles in which all spins are strongly coupled. The magnetization $\mathbf{M}_c$ of a cluster can be oriented along the easy-magnetization axis or in the opposite direction. Correspondingly, the potential energy $W_0(\varphi)$ of a cluster as a function of the angle between $\mathbf{M}_c$ and the easy-magnetization axis has two minima. In a field $\mathbf{H}_{\rm rf}(t)$ a cluster acquires the additional potential energy $V(t)=-\mathbf{M}_c\cdot\mathbf{H}_{\rm rf}(t)$. Then the total potential energy $W_0+V(t)$ will be a periodic function of time. Its oscillations force $\mathbf{M}_c$ to undergo periodic jumps between two opposite potential wells with a time interval $T/2$ between successive jumps, where $T=2\pi/\Omega$ is the period of the rf field. Application of an additional static magnetic field $\mathbf{H}_0$ gives another static contribution $-\mathbf{M}_c\cdot\mathbf{H}_0$ to the potential energy. This makes one potential well deeper than the other, even in the absence of $\mathbf{H}_{\rm rf}(t)$. The applied field $\mathbf{H}_{\rm rf}(t)$ with amplitude greater than $\mathbf{H}_0$ will once again give rise to jumps of the magnetization but in this case the time T_1 which a cluster spends in the potential well with magnetization $\mathbf{M}_c$ parallel to $\mathbf{H}_0$ will be greater than the time T_2 spent in a well with $\mathbf{M}_c$ antiparallel to $\mathbf{H}_0$. A nucleus interacting with a reversing field

$\mathbf{h}(t)$ exchanges with rf photons with frequency Ω with the field. Not having a definite energy, such a nucleus is characterized by infinite sets of quasi-energies separated by an interval $\hbar\Omega$. Transitions between such quasilevels lead to the appearance of a spectrum in the form of a central peak with equidistant satellites.

In addition, there also exists a phonon channel for energy exchange between a nucleus and the rf field $\mathbf{H}_{\rm rf}(t)$. An ac magnetic field excites magnetostriction oscillations in the ferromagnet. These forced oscillations with average amplitude $\overline{x_0}$ along the incident Mössbauer radiation beam also contribute to the intensity of the satellites.[1–4] The value of $\overline{x_0}$ is unknown, so that in Ref. 8, in explaining Pfeiffer's results,[11] we used this parameter only as an adjustable parameter. Therefore, to separate the photon channel in a pure form and check the model of step-wise reversals, it is desirable to quench the magnetostrictional oscillations. To this end, in our experiment, which we describe below, we chose as the absorber a very thin permalloy film with thickness $\mathcal{D}\ll\lambda_s/2$, where λ_s is the wavelength of the magnetostrictional oscillations. In such a film the conditions for a vibrational resonance are strongly degraded and $\overline{x_0}\approx 0$.

In the general case, when both a field $\mathbf{H}_{\rm rf}(t)$ and a field $\mathbf{H}_0$ which is parallel to $\mathbf{H}_{\rm rf}(t)$ are imposed, the magnetic field at a nucleus can be written in the form

$$\mathbf{h}(t)=\mathbf{h}_0 f(t), \quad f(t)=f(t+T), \quad f(t)=\begin{cases} +1, & -T_1<t<0, \\ -1, & 0<t<T_2, \end{cases} \tag{1}$$

where $T=T_1+T_2$. The asymmetry of the reversals is described by the parameter

$$R=\frac{T_1-T_2}{T_1+T_2}, \tag{2}$$

which assumes values in the interval $0\leqslant R\leqslant 1$. The Floquet wave function of a nucleus in the field $\mathbf{h}(t)$ has the form

$$\Psi^N_{I_\kappa M\kappa}(t)=|I_\kappa M_\kappa\rangle\Phi^N_{I_\kappa M_\kappa;n}(t)e^{-i\mathcal{E}^N_{M_\kappa;n}t/\hbar}, \tag{3}$$

where $|I_\kappa M_\kappa\rangle$ is the stationary function of a nucleus in state κ ($\kappa=g$ for the ground state and $\kappa=e$ for the excited state) with spin I_κ and the projection M_κ of the spin on the direction $\mathbf{h}_0$; $\Phi^N(t)=\Phi^N(t+T)$ is a periodic function of time.[8] The complete set of quasi-energies is determined by the expression

$$\mathcal{E}^N_{M_\kappa;n}=E^N_\kappa-\gamma_\kappa M_\kappa\langle h(t)\rangle+n\hbar\Omega, \tag{4}$$

where $E^N_g=0$ and $E^N_e=E'_0$ is the energy of the unsplit resonance level, γ_κ is the gyromagnetic ratio of the nucleus in the κth state, and $\langle h(t)\rangle$ is the time-averaged field $h(t)$ and is given by

$$\langle h(t)\rangle=h_0 R. \tag{5}$$

As the spin $\mathbf{I}_\kappa$ of the nucleus follows the reversals of the field $h(t)$, its direction of precession periodically changes. The average frequency of Larmor precession around the field $h(t)$ can be introduced as follows:

$$\langle \Omega_L^{\kappa} \rangle = \lim_{t \to \infty} \frac{\varphi_{\kappa}}{t}, \tag{6}$$

where φ_{κ} is the angle of rotation of the nuclear spin in the κth state over the time t. When $R \neq 0$, the preferred direction of precession around the field is $+\mathbf{h}_0$ and the average Larmor frequency equals the conventional precession frequency

$$\langle \Omega_L^{\kappa} \rangle = \gamma_{\kappa} \langle h(t) \rangle \tag{7}$$

in a constant magnetic field $\mathbf{h}_0 R$. Such averaged rotation of the spin with Larmor frequency $\langle \Omega_L^{\kappa} \rangle$ results in a splitting in the quasilevels (4) that depends on the magnitude of the time-averaged field $\langle h(t) \rangle$.

If it is assumed, as a simplification, that there is no quadrupole interaction, then the absorption cross section averaged over the energy distribution of the incident γ-rays is given by the equation[8]

$$\sigma_a(s) = \frac{\sigma_0 \Gamma^2}{2} e^{-2W_e - 2W_a} \sum_{n=-\infty}^{\infty} \sum_{M_e, M_g} \frac{J_{eg}(\vartheta) |a_{eg}(n)|^2}{(s - \Delta - \hbar \alpha_{eg} R - n\hbar\Omega)^2 + \Gamma^2}, \tag{8}$$

where $\Delta = E_0' - E_0$ determines the isomeric shift, σ_0 is the cross section at resonance, e^{-2W} are the Debye–Waller factors for the source (e) and absorber (a), Γ is the width of the resonance level, $s = (v/c)E_0$, v is the velocity of the source relative to the absorber, the functions $J_{eg}(\vartheta)$ determine the relative intensities of the lines $M_g \to M_e$, which depend on the angle ϑ between the wave vector $\mathbf{k}$ of the incident γ-rays and $\mathbf{h}_0$ (see, for example, Ref. 8).

Moreover, we have employed the notation

$$\hbar \alpha_{eg} = (\gamma_g M_g - \gamma_e M_e) h_0, \quad x_{eg} = \frac{\alpha_{eg} T}{2},$$

$$|a_{eg}(n)| = \frac{2x_{eg}}{[(1-R)x_{eg} - n\pi][(1+R)x_{eg} + n\pi]} \sin\left\{ \frac{1+R}{2} [(1-R)x_{eg} - n\pi] \right\}. \tag{9}$$

We can see from Eqs. (8) that if $R \neq 0$, each absorption line splits into a Zeeman sextet corresponding to interaction with a constant magnetic field $h_0 R$. This equation describes exchange of rf photons between a nucleus and a classical rf field $h(t)$. To study this process in a pure experiment without forced oscillations, we employed a thin absorbing permalloy (58% Fe-42% Ni) film with thickness $\mathcal{D} = 7$ μm. The Mössbauer spectrometer operated in a regime of constant acceleration with good linearity of the source motion. The sample was placed inside an inductance coil of a resonance loop of a high-power rf generator, generating the rf magnetic field $\mathbf{H}_{\mathrm{rf}}(t)$ in the plane of the absorbing film. Moreover, a Helmholtz coil was used to obtain a constant magnetic field $\mathbf{H}_0$ parallel to $\mathbf{H}_{\mathrm{rf}}(t)$. In all measurements the amplitude of the ac field $\mathbf{H}_{\mathrm{rf}}(t)$ was equal to 25 G. The wave vector $\mathbf{k}$ was always perpendicular to the surface of the film.

The experimental results are displayed in Figs. 1 and 2 (dots). They are presented in relative units with $N(\infty) = 100\%$, corresponding to the intensity of the transmitted radiation far from resonance. The solid lines in the figures represent our numerical calcula-

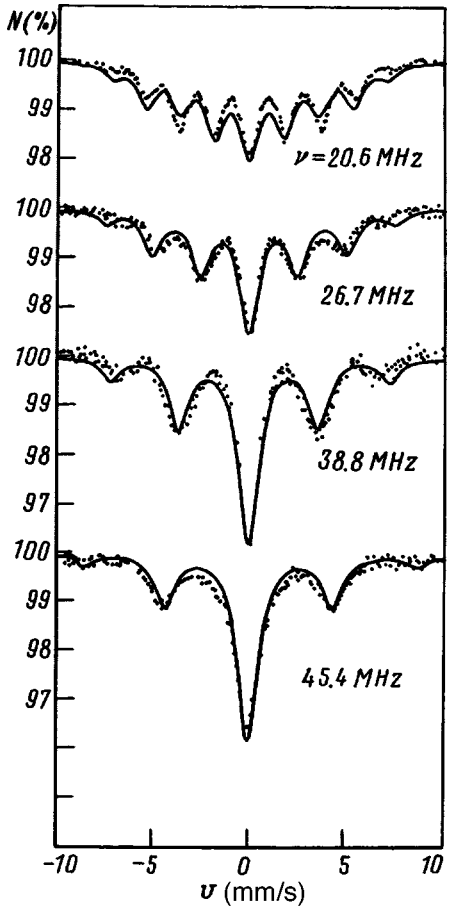

FIG. 1. Mössbauer spectra of nonvibrating permalloy film at different frequencies of the rf field.

tions, in which Eq. (8) was used. The results of measurements performed with $\mathbf{H}_0=0$ at different frequencies $\nu=\Omega/2\pi$ are presented in Fig. 1. We see here a rapid dropoff of the intensity of the satellites with increasing satellite number n. The more extended distribution of the satellite intensities that was observed earlier (see, for example, Refs. 1 –4) can be attributed to magnetostrictional oscillations. Here the standard rf collapse into an isolated line is also observed at high frequencies.

Figure 2 displays the results of measurements performed with a constant field $\mathbf{H}_0 \neq 0$, where the frequency ν of the ac field $\mathbf{H}_{\rm rf}(t)$ is fixed at 38.8 MHz. The data described by the curve *a* were obtained with $\mathbf{H}_0=0$; b — 7.5 G; c — 12 G; d — 16 G. The corresponding values of the adjustable parameter R are 0, 0.04, 0.1, and 0.13. Moreover, $\Gamma=0.5$ mm/s.

So, our data are described well by a simple model of step-wise field reversals. The observed splitting of the satellites confirms the reality of the nuclear quasi-energies (4) and the cluster structure of soft ferromagnets. Earlier, Kopcewicz *et al.*[12] observed a

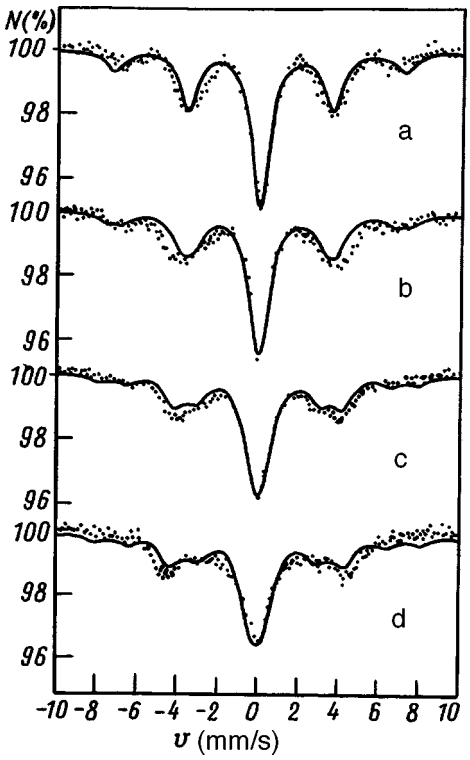

FIG. 2. Mössbauer spectra for different values of the additional constant magnetic field and fixed frequency 38.8 MHz of the rf magnetic field.

splitting of only the collapsed isolated line by superposing an additional constant magnetic field. They interpreted this effect as a destruction of the collapse due an increase in the anisotropy field. However, our observations attest to the fact that this splitting is caused by the asymmetry of the magnetic-field reversals. At high frequencies a nucleus feels only the time-averaged field $\langle h(t)\rangle$, which does not vanish if $R\neq 0$. For this reason, at high frequencies and $R\neq 0$, the spectrum collapses into a Zeeman sextet corresponding to the constant field $\langle h(t)\rangle$.

[a)]e-mail: dzyublik@kinr.kiev.ua

[1]L. Pfeiffer in *Mössbauer Effect Methodology*, edited by I. J. Gruverman, Plenum Press, New York, 1972, Vol. 7, p. 263.
[2]J. K. Srivastava in *Advances in Mössbauer Spectroscopy*, edited by B. V. Thosar, P. K. Iengar, J. K. Srivastava, and S. C. Bhargava, Elsevier, Amsterdam, 1983, pp. 761–813.
[3]M. Kopcewicz in *Mössbauer Spectroscopy Applied to Inorganic Chemistry*, edited by G. J. Long and F. Grandjean, Plenum Press, New York, 1989, Vol. 3, pp. 243–287.
[4]M. Kopcewicz, Struct. Chem. **2**(105), 313 (1991).
[5]Yu. V. Baldokhin, S. A. Borshch, L. M. Klinger, and V. A. Povitsky, Zh. Éksp. Teor. Fiz. **63**, 708 (1972) [Sov. Phys. JETP **36**, 374 (1972)].
[6]S. R. Julian and J. M. Daniels, Phys. Rev. B **38**, 4394 (1988).

[7] A. Ya. Dzyublik, Phys. Status Solidi B **194**, 699 (1996).
[8] A. Ya. Dzyublik and V. Yu. Spivak, Zh. Eksp. Teor. Fiz. **111**, 1438 (1997) [JETP **84**, 794 (1997)].
[9] D. G. Rancourt, S. R. Julian, and J. M. Daniels, J. Magn. Magn. Mater. **51**, 83 (1985).
[10] D. G. Rancourt, H. H. A. Smit, and R. C. Thiel, J. Magn. Magn. Mater. **66**, 121 (1987).
[11] L. Pfeiffer, J. Appl. Phys. **42**, 1725 (1971).
[12] M. Kopcewicz, H. G. Wagner, and U. J. Gonser, J. Magn. Magn. Mater. **51**, 225 (1985).

Translated by M. E. Alferieff

Effect of the coherence of free electron–hole pairs on excitonic absorption in GaAs/AlGaAs superlattices

K. L. Litvinenko[a)] and V. G. Lysenko
Institute of Problems of the Technology of Microelectronics and Ultrapure, Materials, Russian Academy of Sciences, 142432 Chernogolovka, Moscow Region, Russia

J. M. Hvam
Mikroelektronik Centrel, DTU, DK-2800 Lyngby, Denmark

(Submitted 4 December 1997)
Pis'ma Zh. Éksp. Teor. Fiz. **67**, No. 1, 62–67 (10 January 1998)

The effect of photoexcited free carriers on the absorption spectra dynamics of GaAs/$Al_xGa_{1-x}As$ superlattices is investigated experimentally by the pump–probe method. A sharp change in the shift of the excitonic resonance energy from the low- to the high-energy direction is found to occur at the moment that the electromagnetic radiation of the pump and probe beams overlap in the case of band–band excitation. This phenomenon is explained in a model of scattering of high-energy electron–hole pairs. The dephasing time of free high-energy particles is experimentally estimated to be several tens of femtoseconds. © *1998 American Institute of Physics.* [S0021-3640(98)01201-8]

PACS numbers: 71.35.Cc, 71.35.Ee, 42.50.Hz, 78.66.Fd

One of the phenomena arising when coherent polarization interacts with an exciting laser radiation is the optical Stark effect. The optical Stark effect in semiconductors is studied by the method of pumping and probing with subpicosecond laser pulses. Thus far, the situation when the spectral position of the pump beam is far below[1,2] or above[3] excitonic resonance has been well studied experimentally and theoretically.

The study of the interaction of excited states with coherent laser radiation in the case of resonant excitation is only now beginning. For this case it is still impossible to solve the complete semiconductor Bloch equation.[4–6] It has been shown in the theoretical works[1,7] that in the complete absence of free electron–hole pairs Rabi oscillations of the density of excitonic states should be observed in the case of resonant excitation. To study this phenomenon experimentally the duration of the laser pulses must be much shorter than the phase relaxation time of the excited states. But, quite short laser pulses have a large spectral width, which makes selective excitation of only excitonic states without excitation of the electron–hole plasma impossible. In the present investigation, despite the lack of the corresponding theoretical models we considered the problem of studying experimentally the effect of free electron–hole pairs on the coherent interaction of resonant laser radiation with excitonic states.

In the experimental part of this work we employed a multilayered 20-period quantum well (MQW) with 80 Å wide GaAs layers and 20 Å wide AlGaAs layers. Photoexcitation was performed with 120 fs laser pulses whose spectral position was 1–2 meV

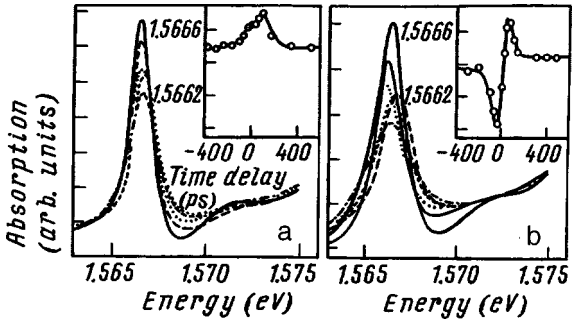

FIG. 1. Change in the shape of the heavy-exciton absorption spectrum for two excitation conditions and different delay times τ. The case of resonant excitation is presented in Fig. 1a: $\tau=-1$ ps (—), -300 fs (. . . .), 0 (-..-), 100 fs (. . . . . .), and 1 ps (- - -). The case of nonresonant excitation is presented in Fig. 1b: $\tau=-425$ fs (—), -85 fs (-.-.), -50 fs (. . . .), 0 (-..-), 70 fs (- - -), and 475 fs (. . . . .). Insets: Change in the energy position of the peak of the heavy-exciton absorption line for two conditions of excitation.

below (we shall call excitation with such pulses resonant excitation) and 10 meV above (nonresonant excitation) the excitonic resonance.

The changes occurring in the shapes of the heavy-exciton absorption spectra for different delays between the pump and probe beams and for two excitation conditions are presented in Fig. 1. The shift in the energy and the decrease in the peak absorption are several times smaller for resonant excitation than for nonresonant excitation. For this reason, in order to work with quantities of the same order of magnitude we chose the pump beam intensity to be lower for nonresonant excitation. Thus, the photoexcited quasiparticle density was 1.4×10^{11} cm^{-2} for the spectra displayed in Fig. 1a and 4.4×10^{10} cm^{-2} for Fig. 1b. This corresponds to a pump pulse area of approximately 1π and 0.6π, respectively. The change in the position of peak excitonic absorption on the energy scale is shown in the insets in Figs. 1a and 1b. A blue shift of the excitonic line is observed in the case of resonant excitation. Peak excitonic absorption in the case of nonresonant excitation shifts at first in the red direction and then rapidly in the blue direction.

The pronounced absorption determined by the continuous heavy-exciton states enabled us to separate the effects due to a change in the band gap and binding energy on the position of the heavy-exciton ground state on the energy scale. For this, we employed the generalized Elliott formula.[8] The results of an analysis of the experimental absorption spectra are displayed in Figs. 2 and 3. It was found that for our experimental conditions virtually no change in the oscillator strength is observed and that the decrease in absorption is caused primarily by broadening of the excitonic resonance. As shown in Ref. 9, the broadening is directly proportional to the quasiparticle density, so that the change in the density of photoexcited states can be determined unequivocally from the change in the broadening. Figure 2 shows the behavior of the broadening of the excitonic lines for two conditions of excitation.

In the case of resonant excitation by 1π laser pulses one Rabi oscillation of the density of excitonic states should be observed.[7] For resonant excitation we indeed de-

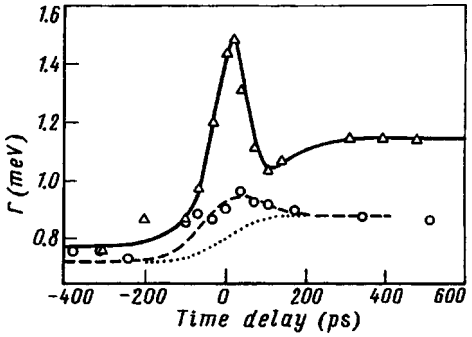

FIG. 2. Broadening Γ of the excitonic absorption line versus the delay time for two excitation conditions. Circles — resonant excitation. Triangles — nonresonant excitation. See text for explanations.

tected an increase in broadening and hence in the density of interacting particles at the moment when the pump and probe beams overlapped (see Fig. 2). After passage of the laser pump pulse, a nonzero density of excited states remains in the sample. This attests to the presence of scattering processes,[1] the effect of which is that the density of photoexcited quasiparticles now consists of a superposition of virtual and real excited states, the contribution of the real particles increasing monotonically and is proportional to the time integral of the intensity of the laser radiation which has passed through the sample. This monotonic increase is shown in Fig. 2 by the dotted line. The dashed line in the same figure takes account of the effect of both types of particles on the width of the excitonic absorption line and describes the experimental results quite well.

The behavior of the broadening in the case of nonresonant excitation is of the same character. This indicates that the density of the particles that participate in the interaction

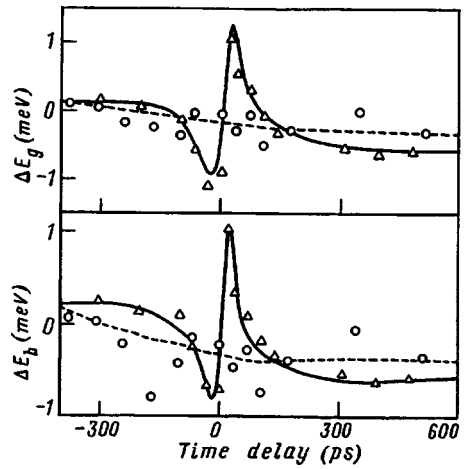

FIG. 3. Change in the band gap E_g and binding energy E_b of a heavy exciton versus the delay time for two excitation conditions. Circles — resonant excitation. Triangles — nonresonant excitation. The lines are drawn as an aid in following the change in the parameters shown.

is also a superposition of virtual and real states, a substantial fraction of which are now free electron–hole pairs. The presence of free excited states in the system explains the comparatively large difference of the amplitude of the change in the broadening of the excitation absorption line as compared with the case of resonant excitation, since the action of free electron–hole pairs on the width of the excitonic line is at least an order of magnitude more effective than in the case of exciton–exciton interaction.[9] In the case of resonant excitation, on account of the quite large spectral width of the exciting laser radiation in the sample, free electron–hole pairs are nonetheless created and thus it is impossible to determine unequivocally what causes the increase in the broadening of the excitonic line in this case — Rabi oscillations of the excitonic density or free carriers. A further increase of the density of the exciting laser radiation, which should lead to an increase in the number of Rabi oscillations,[7] results in a substantial increase in the saturation of excitonic absorption and can destroy the sample. Thus, we were not able unequivocally to detect Rabi oscillations by the pump–probe method in the superlattice under study.

However, we were able to detect the unique behavior of the resonance position of the excitonic absorption line in the case of nonresonant excitation. The familiar blue shift is observed in the case of resonant excitation (see inset in Fig. 1a). Its behavior is determined by two well-known effects: renormalization of the band gap[10] and change in the binding energy.[11] Both effects are presented in Fig. 3. In the case of nonresonant excitation, a red shift of the excitonic line is observed for negative time delays τ. As $\tau \rightarrow 0$ this shift decreases rapidly and changes sign when τ becomes positive. This change occurs during the temporal overlap of the pump and probe laser beams. At first glance it appears that the oscillations of the energy position of the excitonic line will be caused by the direct effect of Rabi oscillations of the density of excited states. However, as follows from Ref. 7, the 0.6π pump pulse does not give rise to density oscillations and therefore this phenomenon must be caused by something else.

Let us consider first the behavior of the binding energy of the excitonic ground state (see Fig. 3). As the modulus of the negative time delay between the pump and probe beams decreases, i.e., as the influence of the density of photoexcited particles increases, the binding energy decreases rapidly. This decrease is caused by the effect of the filling of the phase space (FPS), as predicted in the theoretical work Ref. 11. Since the particle density does not change abruptly when the sign of the shift in the position of the excitonic line changes rapidly (see Fig. 2), the jump in the binding energy should be due to scattering of the particles participating in the interaction. Indeed, after scattering the free electrons and holes will occupy different positions in wave-vector space and will no longer participate in the FPS effect, which ultimately can result in an increase of the binding energy on account of the correlation and exchange interactions. The time between the maximum shifts of the energy position of the excitonic absorption line in the red and blue directions changes from several tens to hundreds of femtoseconds and depends on the density of the exciting radiation.

When the excitonic absorption spectrum was approximated by a generalized Elliott formula,[8] the broadening of the continuous states varied in the range from 2.1 to 3.5 meV. This corresponds to a change in the phase relaxation time from 600 to 350 fs. These values agree well with our results: In the one-beam experiment (in preparation for pub-

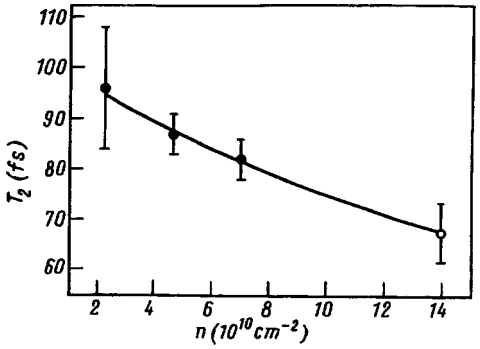

FIG. 4. Temporal distance between the maximum decrease and increase of the binding energy of an excitonic state in the case of nonresonant excitation versus the density of electron–hole pairs.

lication) and in the four-wave mixing experiment[12] (see also Ref. 13), however, they are much greater than the time interval between the maximum shifts of the excitonic resonance line in the red and blue directions. Indeed, the dephasing time of free excited states decreases substantially with increasing energy of these states.[12] This change is so large that free particles from only a narrow region (of the order of 2 meV wide) near the band gap participate in the destructive interference effect.[12] Higher-lying states lose coherence much earlier. Thus, in the case studied the behavior of the excitonic resonance is affected decisively by the loss of coherence between the exciting laser radiation and the high-energy electron–hole pairs. Figure 4 shows the particle-density dependence of the time T_2 required for a sharp change to occur in the binding energy. This time is directly proportional to the phase relaxation time. The simplest model describing this dependence is the Drude model of an electron gas, which neglects the Coulomb interaction. According to this model, the dephasing time is inversely proportional to the density of interacting particles and can be represented in the form

$$2\hbar/T_2(n) = 2\hbar/T_2(0) + \gamma^{\text{eff}} E_B^{\text{eff}} (a_B^{\text{eff}})^2 n_x , \tag{1}$$

where $\hbar$ is Planck's constant, E_B^{eff} is the effective binding energy ($E_B^{\text{eff}} = 5.6$ meV), a_B^{eff} is the effective Bohr radius ($a_B^{\text{eff}} = 100$ Å[14]), and n_x is the density of excited states. The theoretical dependence, shown by the solid line in Fig. 4, was obtained for the following values of the parameters: $T_2(0) = 102$ fs and $\gamma_{eh}^{\text{eff}} = 8.2$. The value that we obtained for T_2 equals in order of magnitude to the phase relaxation time of free electron–hole pairs, which varies from 30 to 160 fs and depends on the parameters of the specific quantum well.[15]

Let us now return to the change in the band gap E_g (see Fig. 3). As the overlapping between the pump and probe beams increases, the quasiparticles created start to have an increasingly larger effect on the behavior of E_g. The decrease in the band gap in both quasi-two- and three-dimensional media with increasing density of excited states is a well-known factor, which has been confirmed experimentally[16–18] and theoretically.[19,20] However, the answer to the question of why in the case of nonresonant excitation the band gap increases when the high-energy free carriers lose coherence remains open. To answer this question it is necessary to solve the complete semiconductor Bloch

equation.[4–6] We can say only that the unique band-gap behavior that we detected is due to the interaction: coherent excitons, coherent and incoherent free electron–hole pairs, as well as the pump and probe laser beams.

In summary, we have found experimentally that in the case of nonresonant excitation the position of the excitonic line on the energy scale shifts in the red direction for negative τ and the blue direction for positive τ. This behavior of the excitonic absorption line is explained by dephasing of the free electron–hole pairs created. The dephasing time of high-energy free carriers, equal in order of magnitude to several tens of femtoseconds, was estimated from the distance between the maximum shifts of the energy position of the excitonic resonance.

This work was supported by Russian Fund for Fundamental Research Grant 97-02-16833 and INTAS-94-0324 and INTAS-RFBR-95-0576.

[a)]e-mail: kostja@ipmt-hpm.ac.ru

---

[1] R. Binder, S. W. Koch, M. Lindberg *et al.*, Phys. Rev. Lett. **65**, 899 (1990).
[2] R. Binder, S. W. Koch, M. Lindberg *et al.*, Phys. Rev. B **43**, 6520 (1991).
[3] S. W. Koch, N. Peyghambarian, and M. Lindberg, J. Phys. C: Solid State Phys. **21,** 5229 (1988).
[4] W. Schafer, K. H. Schuldt, and R. Binder, Phys. Status Solidi B **150**, 407 (1988).
[5] I. Baslev, R. Zimmermann, and A. Stahl, Phys. Rev. B **40**, 4095 (1989).
[6] M. Lindberg and S. W. Koch, Phys. Rev. B **38**, 3342 (1988).
[7] S. W. Koch, A. Knorr, R. Binder, and M. Lindberg, Phys. Status Solidi B **173**, 177 (1992).
[8] P. Lefebvre, P. Christol, and H. Mathieu, Phys. Rev. B **48**, 17308 (1993).
[9] A. Honold, L. Schultheis, J. Kuhl, and C. W. Tu, Phys. Rev. B **40**, 6442 (1989).
[10] P. Vashishta and R. K. Kalia, Phys. Rev. B **25**, 6492 (1982); M. J. Godfrey, and V. Kubrak, Phys. Rev. B **52**, 17293 (1995).
[11] G. Dresselhaus, Phys. Chem. Solids **1**, 14 (1956).
[12] A. G. Gorshunov, V. I. Grinev, K. L. Litvinenko *et al.*, in preparation for publication.
[13] A. G. Gorshunov, K. L. Litvinenko, V. G. Lysenko *et al.*, Zh. Éksp. Teor. Fiz. **110,** 1464 (1996) [JETP **83**, 809 (1996)].
[14] J. Feldmann, T. Meier, G. von Plessen *et al.*, Phys. Rev. Lett. **70**, 3027 (1993).
[15] K. L. Litvinenko, V. G. Lysenko *et al.*, JETP Lett. **66**, 144 (1997).
[16] B. K. Ridley, Rep. Prog. Phys. **54**, 169 (1991).
[17] V. G. Lyssenko and V. I. Revenko, Fiz. Tverd. Tela (St. Petersburg) **20**, 2144 (1978) [Sov. Phys. Solid State **20**, 1238 (1978)].
[18] G. Trankle, H. Leier, F. Forchel *et al.*, Phys. Rev. Lett. **58**, 419 (1987).
[19] S. Das Sarma, R. Jalabert, and S.-R. Eric Yang, Phys. Rev. B **39**, 5516 (1989).
[20] S. T. Cundiff, A. Knorr, J. Feldmann *et al.*, *Semiconductor Optics*, Springer-Verlag, Berlin, 1995; Phys. Rev. Lett. **73**, 1178 (1994).
[21] S. Nojima, Phys. Rev. B **51**, 11124 (1995).

Translated by M. E. Alferieff

On the possibility of quantization of the conductance in the microwave-induced resistive state of layered superconductors

Yu. I. Latyshev
Institute of Radio-Engineering and Electronics, Russian Academy of Sciences, 103907 Moscow, Russia

(Submitted 5 December 1997)
Pis'ma Zh. Éksp. Teor. Fiz. **67**, No. 1, 68–71 (10 January 1998)

It was observed that a microwave field induces constant differential resistance steps, close in magnitude to the reciprocal of the conductance quantum $h/2e^2$, in the current–voltage characteristics (IVCs) of layered structures with an intrinsic Josephson effect under conditions of transport in a direction perpendicular to the layers. A qualitative explanation of this result is proposed. © *1998 American Institute of Physics.* [S0021-3640(98)01301-2]

PACS numbers: 74.80.Dm, 74.25.Nf, 74.50.+r

It is well known that in layered superconductors it is possible to observe an intrinsic Josephson effect on the natural layered crystalline structure of the material (for a review, see, for example, Ref. 1). Strictly speaking, to observe both Josephson effects (stationary and nonstationary) the size of the junction in the plane of the layers must be less than the characteristic Josephson length $\lambda_J = s(\lambda_c/\lambda_{ab})$, where s is the distance between the elementary superconducting layers and λ_c and λ_{ab} are anisotropic London penetration depths. In typical layered high-T_c materials of the BSCCO type one has $\lambda_J \sim 1-2$ μm. Recently, substantial efforts have been made to reduce the lateral dimensions of such structures. It has been shown that a stationary intrinsic Josephson effect first appears on junctions with dimensions <20 μm.[2] Attempts to observe a nonstationary intrinsic Josephson effect on samples with dimensions <10 μm nonetheless have been unsuccessful.[3,4] In many cases resistive features, whose position on the voltage scale depended on the microwave power, were observed, instead of the expected steps of constant voltage (Shapiro steps), on the IVCs of junctions in a microwave field. In the present letter reports the observation of microwave-induced steps of constant differential resistance R_d, close to the reciprocal of the conductance quantum, $R_d \approx h/2e^2$, on the IVCs.

The experiment was performed on overlap-type junctions, obtained by selective ion-plasma etching of high-quality single-crystalline BSCCO 2212 whisker crystals.[2] The main results will be presented for a junction with the dimensions $L_a \times L_b \times L_c = 4 \times 8 \times 0.12$ μm. The junction was placed at an antinode of the E field in a 3-cm waveguide. The IVCs were measured by a four-probe method. The measurements were performed mainly at liquid-helium temperatures. The critical current density along the c axis was equal to $3 \times 10^2 - 10^3$ A/cm^2 at 4.2 K, approximately three orders of magnitude less than the density measured on the same whisker crystals along the a axis.

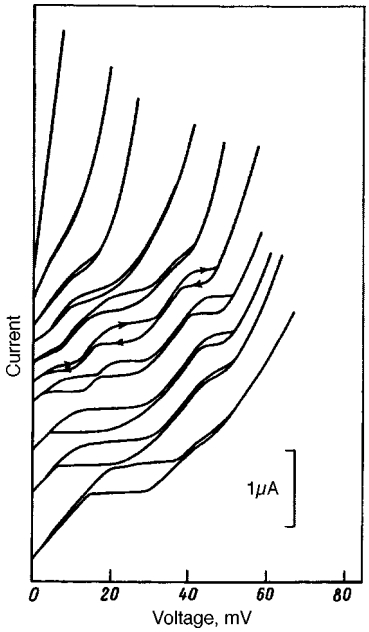

FIG. 1. Constant differential resistance steps produced in the IVCs of BSCCO 2212 layered structure by a 11.5 GHz microwave field. The curves correspond to following incident powers (from top to bottom): 0.20, 0.40, 0.63, 0.89, 1.26, 1.48, 1.59, 1.78, 1.87, and 2.19 mW. The dimensions of the structure were $4\times8\times0.12$ μm along the a, b, and c axes, respectively; $T=4.2$ K. The curves are shifted along the current axis, so that the zero of each curve in terms of current corresponds to the zero in terms of voltage.

Figure 1 shows a family of IVCs for a sample in a resistive state induced by a microwave field with microwave power $W>200$ μW incident on the sample. In the absence of the microwave radiation the critical current I_c of the sample equals ≈100 μA. The critical current was suppressed to zero at $W\approx20$ μW. As one can see from Fig. 1, the effect of the microwave field is to produce resistive features (steps) in the IVCs. We note the characteristics of the observed features: 1) The steps correspond to approximately the same slope (differential resistance) of magnitude 13–14 kΩ, irrespective of the radiation power (Fig. 2); 2) the steps appear with approximately constant spacing

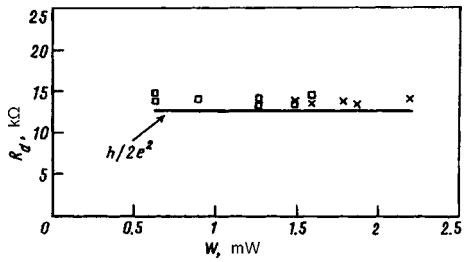

FIG. 2. Differential resistance of the first (□) and second (×) steps as a function of microwave power. The solid curve corresponds to the quantity $R=h/2e^2$.

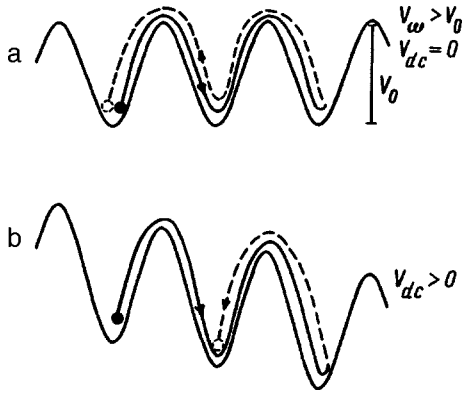

FIG. 3. Schematic diagram of the trajectory of a charge under the action of a microwave field with a sufficiently high amplitude in a periodic potential over the first half period (solid curve) and over the second half period (dashed curve) in the presence of only a microwave field (a) and under the combined effect of a microwave field and a constant field (b).

$\Delta V \approx 10$ mV on the V axis; 3) the current amplitude of the steps depends nonmonotonically on W; and, 4) the steps occur in the range of currents ≈ 1 μA and in terms of the current the first and second steps ≈ 0.5 μA.

The most noteworthy result is that the magnitude of the differential resistance on a step is close to the reciprocal of the conductance quantum, $h/2e^2$ (Fig. 2a).

The proposed interpretation is based on the fact that a layered superconductor can be regarded as a system with a modulated potential along the c axis (see Fig. 3), for example, because of the fact that the modulus of the order parameter is modulated in a direction perpendicular to the layers.[1] In this case the potential can treated in the quasiclassical sense. Let a charge $q=ne$ be placed at a minimum of the potential, and let an external high-frequency field E_ω with amplitude large enough to transfer the charge from one potential well into another be applied. This will induce an ac current in the system, but the dc current $\langle I_{dc} \rangle$ averaged over one period obviously equals zero. Let us now imagine that a constant field E is applied in addition to an ac field (Fig. 3b). Then it is possible to have a situation in which during the first half period the charge will move in a higher average field in the forward direction than in the backward direction and the charge can move forward by two (n) wells and backward by one $(n-k)$ well (Fig. 3b), i.e., during one period of the oscillations of the external field the charge is displaced by one (k) well. In other words, a nonzero average (over one period) dc current associated with these processes will appear

$$\langle I_{dc} \rangle = knef. \tag{1}$$

This situation is known as ac–dc interference in systems with a charge-density wave (CDW) in a model where the motion of the CDW is regarded as a motion of a charged particle in a periodic potential (see, for example, Ref. 5). At the same time charge displacement can occur by means of subbarrier Josephson tunneling. In this case, under the action of a voltage V_{dc} ac currents, whose frequency is proportional to V_{dc}, arise in the system:

$$V_{dc} = pNh\nu/2e, \tag{2}$$

where p is the number of the harmonic and N is the number of elementary junctions in the contact. In the case when both processes have the same frequency ($f = \nu$) a resonance observed in some region of frequency lock-in $\delta f = \delta\nu$ can be expected, whence

$$\frac{dV}{dI} = \alpha \frac{h}{2e^2}, \tag{3}$$

where $\alpha = pN/kn$. Thus, the resonance steps are reminiscent of Shapiro steps, but with a finite slope determined by the quantity $\alpha h/2e^2$.

The quantity $h/2e^2$ equals ≈ 12.7 kΩ. The value ≈ 13.5 kΩ is observed experimentally (Fig. 2). In the present model this should correspond to the condition $\alpha \approx 1$. An estimate of the parameter α for the experiment gives the following. For our sample $N \approx 80$, the position of the first current step corresponds to ≈ 0.5 μA, which gives for $f = 11.5$ GHz $kn \approx 300$. The quantity p can be estimated from Eq. (2), assuming the position of the first step in V equals $\Delta V \approx 10$ mV. This gives $p = 4$. Finally, we have $\alpha = pN/kn \approx 1$, in good agreement with the model.

Estimates of the microwave fields at which steps first appear give an amplitude ~ 20 mV for the microwave potential on an individual junction, which is comparable to a degree of modulation of the potential V_0 across the layers $\sim \Delta = 15$–30 mV.

Two steps were clearly seen in the experiments. Their amplitudes in terms of the current depended nonmonotonically on the power of the radiation, and the peak amplitude of the first step approximately corresponded in terms of power to the appearance of a second step and the peak amplitude of the second step corresponded to vanishing of the first step. The steps exhibit hysteresis as a function of the current. This behavior is in many ways reminiscent of the behavior of the Shapiro steps in the underdamped regime. In all probability, the second step corresponds to a resonance at the second harmonic relative to the first step.

In summary, the proposed model describes the observed phenomenon qualitatively. It is still unclear how the system adjusts, preserving under resonance conditions the parameter $\alpha \approx 1$, and how this parameter will depend on the dimensions of the junction, the number of elementary layers, and other characteristics of the system.

This work was reported in part at the 1st International Conference on the Internal Josephson Effect and Terahertz Plasma Oscillations, Sendai, 1997. I wish to thank the participants of the conference S. N. Artemenko, I. Bozovich, N. Ong, P. Müller, and A. Ustinov as well as P. Monceau and O. Buisson for a discussion of the results. This work was supported by the Russian State Program on High-T_c Superconductivity (Project 95028). I am grateful to the Center for Low-Temperature Research (CRTBT–CNRS), Grenoble, where part of this work was performed.

[1] P. Müller, in *Intrinsic Josephson Effects in Layered Superconductors*, edited by R. Helbig, Festkörperproblem, *Advances in Solid State Physics*, Vieuweg Braunschweig/Wiesbaden, 1994, Vol. 34, p. 1.
[2] Yu. I. Latyshev, J. E. Nevelskaya, and P. Monceau, Phys. Rev. Lett. **77**, 932 (1996).
[3] Yu. I. Latyshev, P. Monceau, and V. N. Pavlenko, in *Proceedings of International Symposium on the Intrinsic*

Josephson Effect and Terahertz Plasma Oscillations in High-T_c Superconductors, Feb. 23–25, 1997, Sendai; Pub. Physica C **293**, 174 (1997).
[4]W. Prusseit, M. Rapp, K. Hirata and T. Mochiku, *ibid*., p. 25.
[5]For a review see G. Gruner (ed.), *Density Waves in Solids*, Addison-Wesley, Reading, Mass., 1994.

Translated by M. E. Alferieff

Spectrum of flexural oscillations of a domain wall with drifting Bloch lines

A. B. Shumm, L. M. Dedukh,[a)] and Yu. P. Kabanov
Institute of Solid-State Physics, Russian Academy of Sciences, 142432 Chernogolovka, Moscow District, Russia

(Submitted 5 December 1997)
Pis'ma Zh. Éksp. Teor. Fiz. **67**, No. 1, 72–75 (10 January 1998)

It is observed that in single-crystalline yttrium iron garnet the amplitude of characteristic flexural oscillations of a 180° domain wall containing Bloch lines increases sharply when drift of the Bloch lines is excited. The resonance frequencies of these oscillations are virtually identical to those of flexural oscillations of a monopolar wall. It is shown experimentally that this phenomenon is most likely caused by a magnetic aftereffect. © *1998 American Institute of Physics.* [S0021-3640(98)01401-7]

PACS numbers: 75.60.Ch, 75.50.Cc

It is now well known that the dynamic properties of domain walls (DWs) in ferromagnetic crystals depend strongly on the state of the DW structure. For example, an expression for DW mobility in a ferromagnet was derived on the basis of a specific spin distribution in the wall.[1] The ''low mobility'' paradox, which subsequently existed for a long time, for DWs in single crystals of yttrium iron garnet (YIG)[2,3] was explained by taking account of Bloch lines in the DW structure.[4] In addition, it was found that the Bloch lines strongly decrease not only the DW mobility but also the amplitude of the characteristic flexural oscillations of a DW.[5] The effect of the dynamic transformation of DW structure on the DW velocity in uniaxial garnet films has also been well studied.[6] It has been established that the initiation of dynamic conversion of DW structure as a result of the creation, motion, and vanishing of Bloch lines sharply decreases the DW velocity in these materials in an external magnetic field which exceeds some critical field. In the present letter we report the results of investigations in which the opposite effect was observed: It is shown experimentally that when drift of Bloch lines[7] is excited in DWs in YIG the influence of Bloch lines on the amplitude and frequency of the flexural oscillations of DWs sharply diminishes.

The investigations were performed on single-crystalline YIG plates cut out in the form of a $3.2\times0.7\times0.03$ mm rectangular prism extended along the [111] axis. The sample contained one 180-degree DW, separating domains magnetized in the (112) plane of the plate. The DW in the initial state contained vertical Bloch lines. When required, a monopolar state of the DW was produced and maintained, by means of a constant magnetic field H_z oriented perpendicular to the plane of the plate, in the course of the measurements of the spectra. The magnetic fields were produced with Helmholtz coils with a radius of 6 mm. When the spectral curves were recorded, the amplitude of the current in the coil producing the excitation field was not stabilized and, for this reason,

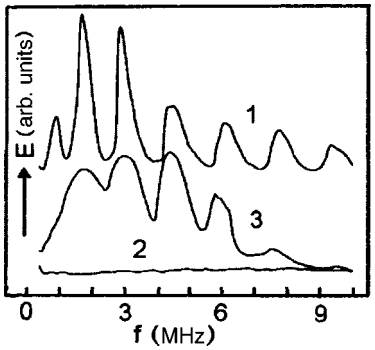

FIG. 1. Curves of the amplitude E of the induction signal as a function of the frequency f of the exciting field H_x. The curves were recorded for monopolar (*1*) and demagnetized (*2*,*3*) DWs. The amplitude $H_x = 0.48$ A/m (*1*,*2*) and 2.38 (*3*), $H_z = 2.07$ kA/m (*1*).

decreased slightly with frequency. The motion of the DW was detected on a SK4-59 spectrum analyzer with the aid of a compensated detection coil wound directly on the sample.

Curve *1* in Fig. 1 characterizes the excitation spectrum of a DW in a monopolar state. The spectrum was recorded in a relatively weak exciting field H_x acting along the magnetization in the domains. The curve shows resonance peaks corresponding to the appearance in the DW of flexural standing waves with wave vector **k** perpendicular to the magnetization in the domains.[4] Resonance flexural oscillations of the DW are not observed in curve *2* (in Fig. 1), which was recorded in the same excitation field for a DW containing Bloch lines. Under these conditions, as direct observations of DWs showed, the Bloch lines fluctuated near the positions of equilibrium. However, as the amplitude of the exciting field increased up to a value producing drift of the Bloch lines[7] resonance peaks associated with flexural oscillations of the DW appeared in the spectrum of the received signal (curve *3* in Fig. 1). One can see that the resonance frequencies of the flexural oscillations of the DW in both states are practically identical. However, the width of the peaks in the spectrum of the demagnetized DW is much larger than in the case of a monopolar DW. This can be due to the additional energy losses occurring with stronger excitation of the spin system.

Curve *1* in Fig. 2 shows an example of a spectrum of oscillations of a demagnetized DW. The spectrum was recorded in an exciting field whose amplitude was close to the critical value. Only two resonance peaks due to flexural oscillations of the DW are clearly shown in it. Direct observation showed that under these conditions the drift of Bloch lines is irregular and it is stable only at frequencies at which the high-amplitude resonance peaks are observed. In repeated measurements the spectra had a different form: The resonance peaks could arise and vanish, but they arose precisely at the resonance frequencies at which drift of the Bloch lines occurred. When an additional constant field H_y was applied perpendicular to the plane of the DW, influencing the drifting of the lines,[8] the behavior of the Bloch lines and the form of the spectrum changed as a function of the magnitude and polarity of H_y. For one polarity of this field, increasing the field stabilized

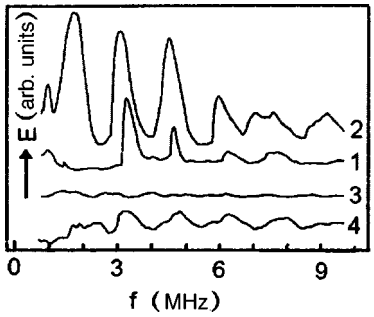

FIG. 2. $E(f)$ curves recorded with field amplitude $H_x = 1.2$ A/m. Curves *2*, *3*, and *4* were recorded in the presence of the additional field $H_y = 0.48$ kA/m (*2*), -0.64 (*3*), and -1.12 (*4*).

the drift of the Bloch lines and simultaneously intensified the flexural oscillations of the DW (curve *2*, Fig. 2). Drift of the lines occurred at all resonance frequencies. When the polarity of the field H_y was reversed and the field was subsequently increased, at first the drift of the Bloch lines completely stopped and, at the same time, the flexural oscillations of the wall vanished (curve *3*, Fig. 2), after which both the drift of the Bloch lines and the flexural oscillations of the DW reappeared (curve *4*, Fig. 2). These data show that when drift of Bloch lines along the DW is initiated, the resonance flexural oscillations of the wall intensify. In addition, it follows from these measurements that an effective field H_{y0} of the order of 0.65 kA/m is present in the experimental sample; this field was observed in YIG single crystals and in earlier experiments.[8]

Figure 3 shows single oscillograms of the magnetooptical signal, which were recorded using a photomultiplier and a storage oscillograph in a local section of the DW at the resonance (1) and intermediate (2) frequencies of the field H_x. The wide and narrow peaks in these oscillograms reflect the passage of subdomains, separated by Bloch lines, through the photometric measurement section.[7,8] Comparing these oscillograms shows that the drift of the Bloch lines is more intense in the case of the resonance oscillation of the DW than at intermediate frequencies.

In summary, the results presented above show that the excitation of drift of Bloch lines results in an effective intensification of resonance oscillations of a DW as compared with DW oscillations under conditions when the Bloch lines fluctuate about the positions of equilibrium. This behavior of a DW can be explained by taking into account the

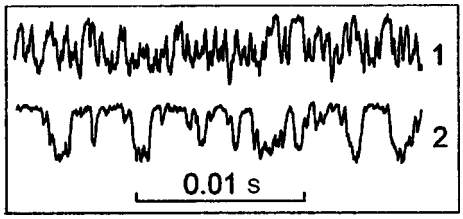

FIG. 3. Magnetooptical single oscillograms reflecting the successive passage of Bloch lines along a DW through the photometric measurement section with $H_x = 5.0$ A/m, $f = 1.8$ MHz (*1*) and 1.1 (*2*).

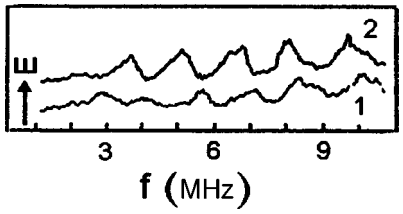

FIG. 4. $E(f)$ curves recorded with a higher sensitivity of the SK4-59 oscillograph than in preceding cases for a demagnetized DW in a field H_x. The amplitude $H_x = 0.04$ A/m. Curve *2* was recorded in the presence of an additional field H_z with amplitude 120 A/m and frequency 100 kHz.

magnetic aftereffect phenomenon, determined by the interaction of Bloch lines with point defects, whose state depends on the direction of the magnetization.[9] According to the theory of this phenomenon, both DWs[9] and Bloch lines,[10] interacting with point defects, produce a potential relief whose height is all the smaller the higher the amplitude of their oscillations and the velocity of their motion. Drifting Bloch lines do not have enough time to produce a potential relief for their own motion, so that their effect on the motion of DWs should diminish substantially. To check this conjecture, we performed an experiment in which in the course of recording the spectrum of oscillations of a wall an additional low-frequency field H_z was applied to the crystal, giving rise to forced oscillations of the lines along the wall. An example of such measurements is shown in Fig. 4. Curve *1* in Fig. 4 represents the spectrum of oscillations of a DW with Bloch lines. The spectrum was recorded with a higher sensitivity of the SK4-59 oscillograph than in the case of the curves presented above. In contrast to curve *2* in Fig. 1, curve *1* in Fig. 4 shows peaks with a complicated shape which are associated with the flexural oscillations of a demagnetized DW.[5] Curve *2* in Fig. 4 was recorded in the presence of an additional field H_z. One can see that in the case when low-frequency oscillations of Bloch lines are excited along the DW by a field H_z, the characteristic oscillations of the wall intensify and the resonance frequencies decrease. Such measurements showed that the characteristic oscillations of a DW are intensified all the more the higher the amplitude and frequency of the field H_z and the lower the amplitude of the exciting field H_x. In other words, the effect of the field H_z on the oscillations of a DW is strongest when the wall oscillates in the deepest potential relief, determined by the interaction of the wall with point defects. However, when the lines start to drift the intensification of flexural oscillations of the DW is an order of magnitude greater.

This work was supported by the Russian Fund for Fundamental Research, Grant 97-02-16879.

[a)]e-mail: dedukh@issp.ac.ru

[1]L. D. Landau and E. M. Lifshiz, Sow. Phys. **8**, 153 (1935).
[2]F. Hagedorn and E. Gyorgy, J. Appl. Phys. **32**, 282S (1961).
[3]R. W. Teale, J. Phys. C: Sol. Stat. Phys. **13**, 2061 (1980).
[4]L. M. Dedukh, V. I. Nikitenko, and V. T. Synogach, Zh. Eksp. Teor. Fiz. **94**, 312 (1988) [Sov. Phys. JETP **67**, 1912 (1988)].
[5]L. M. Dedukh and Yu. P. Kabanov, J. Magn. Magn. Mater. **147**, 355 (1995).

[6] A. Malozemoff and J. Slonczewski, *Magnetic Domain Walls in Bubble Materials*, Academic Press, New York, 1979 [Russian translation, Mir, Moscow, 1982].
[7] V. S. Gornakov, L. N. Dedukh, and V. I. Nikitenko, Zh. Éksp. Teor. Fiz. **86**, 1505 (1984) [Sov. Phys. JETP **59**, 881 (1984)].
[8] V. S. Gornakov, L. N. Dedukh, and V. I. Nikitenko, Zh. Éksp. Teor. Fiz. **94,** 245 (1988) [Sov. Phys. JETP **67**, 570 (1988)].
[9] A. Hubert, *Theorie der Domänenwände in Geordneten Medien*, Springer-Verlag, Berlin, 1974 [Russian translation, Mir, Moscow, 1977].
[10] A. F. Khapikov, Fiz. Tverd. Tela (St. Petersburg) **36,** 2062 (1994) [Phys. Solid State **36**, 1126 (1994)].

Translated by M. E. Alferieff

Forward coherent inelastic Mössbauer scattering of synchrotron radiation

V. A. Belyakov[a)]

L. D. Landau Institute of Theoretical Physics, Russian Academy of Sciences, 117334 Moscow, Russia

(Submitted 10 November 1997)
Pis'ma Zh. Éksp. Teor. Fiz. **67**, No. 1, 9–14 (10 January 1998)

A theoretical analysis is presented of the possibilities of satisfying the conditions of phase matching (PM) in the coherent inelastic Mössbauer scattering (CIMS, which is scattering accompanied by the creation or annihilation of phonons) of synchrotron radiation (SR) and the conditions under which the maximum intensity of CIMS obtains are studied. Of the two types of CIMS — 1) participation of phonons in a scattering event only in the stage of absorption or only during re-emission of a photon, and 2) participation of phonons in both stages of scattering — PM is possible only in the first. The process in which phonons participate only at the photon absorption stage leads to efficient conversion of the SR from a wide spectral line into a narrow line, determined by the width of the Mössbauer transition. Photons of this type of CIMS effectively possess a higher penetrating power than the standard Mössbauer radiation, and their spectral distribution is shifted somewhat in the direction of low frequencies. [S0021-3640(98)00201-1]

PACS numbers: 76.80.+y, 41.60.Ap

Rapid progress in Mössbauer spectroscopy using synchrotron radiation[1] (SR) has led to a new type of spectroscopy with a uniquely high energy resolution, limited only by the width of the Mössbauer line (for example, 10^{-8} eV for the most popular Mössbauer isotope F^{57}). Recent experiments in this field have made it possible to measure directly phonon spectra for condensed media, specifically, for crystalline materials[2] and liquids[3] and to measure inelastic scattering spectra of gases.[4] Forward Mössbauer scattering of SR is important in this field.[5]

The present letter is devoted to a detailed theoretical analysis of the CIMS of SR and it shows a number of specific properties of the forward CIMS that have not been previously investigated.[6] Attention is focused mainly on investigating the possibilities of achieving phase matching (PM) in forward CIMS of SR and the relation between the maximum achievable intensity of forward CIMS in samples of finite thickness and the degree of deviation from PM. Specifically, it is shown that on account of CIMS the maximum intensity of the resonant-energy fraction of the scattered SR obtains for sample thicknesses much greater than the absorption length of the Mössbauer photons. This is explained by the ''pumping'' of nonresonant SR photons into the Mössbauer line. It is shown that a shift (by an amount of the order of the width of the Mössbauer line) of the spectral distribution of the resonant fraction of the CIMS in the direction of lower ener-

gies with respect to the resonance energy occurs as a result of coherence effects.

BASIC EQUATIONS

Let us consider CIMS processes occurring during the propagation of a SR pulse in a sample containing nuclei of a Mössbauer isotope. Since the Mössbauer scattering occurs in two distinct stages — the absorption of a γ ray by a nucleus and subsequent re-emission of the γ ray, there exist three different possibilities for CIMS: 1) absorption or creation of a phonon only at the γ-ray absorption stage, 2) absorption or creation of a phonon only at the γ-ray re-emission stage, and 3) absorption or creation of a phonon at both the γ-ray absorption are re-emission stages. Following the terminology of Ref. 6, we shall call these possibilities CIMS1 — from a nonresonant component of SR into a resonant component, CIMS2 — from a resonant component of SR into a nonresonant component, and CIMS3 — from a nonresonant component of SR into a nonresonant component.

In a typical Mössbauer experiment with SR, the SR pulse duration (of the order of 10^{-12} s) is much shorter than the duration of the Mössbauer scattering process (of the order of 10^{-5}–10^{-9} s), so that the SR pulse can be assumed to be a delta function in time, propagating in the sample with the group velocity of the SR pulse. For the CIMS1 and CIMS3 processes the interaction of the SR with the Mössbauer nuclei in the sample can be regarded as a perturbation, and the electromagnetic field in the sample can therefore be represented as a sum of two components $\mathbf{E}=\mathbf{E}_0+\mathbf{E}_1$, where $\mathbf{E}_0$ is the unperturbed SR field and $\mathbf{E}_1$ is the perturbation due to the interaction of the SR with the Mössbauer nuclei. The equation for $\mathbf{E}_1$ assumes the form

$$-\nabla\times\nabla\times\mathbf{E}_1=c^{-2}(\epsilon_0+\epsilon_1)\partial^2\mathbf{E}_1/\partial t^2+c^{-2}\epsilon_1\partial^2\mathbf{E}_0/\partial t^2, \tag{1}$$

where ϵ_0 is the dielectric constant in the absence of nuclear interaction and ϵ_1 is the correction to the dielectric constant due to the nuclear interaction. The explicit form of ϵ_1 depends on the type of process, among the processes indicated above, and is determined by the corresponding Mössbauer scattering amplitude.

Since the SR pulse can be regarded as a delta function in time, the last term on the right-hand side of Eq. (1) can be represented in the form $(\omega_s/c)^2\epsilon_1\mathbf{E}_0(\omega_s,z)\delta(z-v_g t)$, where ω_s is the SR frequency, v_g is the group velocity of the SR pulse, and z is the coordinate in the direction of propagation of the pulse. Representing the solution of Eq. (1) in the form $\mathbf{E}_1=\mathbf{E}^N\exp[i(kz-\omega t)]$, we obtain for $\mathbf{E}^N$ the equation

$$\mathbf{E}^N[k^2-(\epsilon_0+\epsilon_1)(\omega/c)^2]=(\omega_s/c)^2\chi^N E_0\delta(\omega/v_g-k), \tag{2}$$

where χ^N is the analog of the familiar nonlinear susceptibility in nonlinear optics.[1] Equation (2) implies the condition

$$\omega/v_g\equiv k_p=k, \tag{3}$$

which can be regarded as the phase matching (PM) condition.

COHERENCE LENGTH

Let us examine CIMS in a plane-parallel plate, assuming that the SR propagates in a direction perpendicular to the surface of the plate. According to Ref. 6, the solution of

equation (2) can be represented as a sum of the particular solution of the inhomogeneous equation and a solution of the homogeneous equation. The coefficient in front of the homogeneous solution in this superposition is determined from the boundary conditions, which require that the CIMS intensity vanishes on the entrance surface. As a result, we have for the CIMS amplitude

$$\mathbf{E}_1=(\omega_s/c)^2\chi^N E_0[k^2-(\epsilon_0+\epsilon_1)(\omega/c)^2]^{-1}\{\exp[i(k_p z-\omega t)]-\exp[i(kz-\omega t)]\}, \tag{4}$$

where $k_p=\omega/v_g$. The quantity in braces in Eq. (4) is proportional to $\sin[(k-k_p)z/2]$, so that growth of the CIMS intensity in the sample is limited to the distance $l_c=\pi(k-k_p)^{-1}$, called the coherence length. If the PM condition (3) is satisfied, then the coherence length diverges and the CIMS amplitude at the exit surface increases in proportion to the thickness of the plate. In a real situation, absorption is very strong and limits the unbounded growth of the CIMS intensity with sample thickness.

CONDITIONS OF MAXIMUM CIMS INTENSITY

Let us consider the case of CIMS1 — scattering from a nonresonant into a resonant component. In this case the factor $\epsilon_0+\epsilon_1$ in Eqs. (1) and (2) assumes the form $\epsilon_0+\epsilon_1=1-\Delta\epsilon_{el}+\Delta\epsilon_M$, where $\Delta\epsilon_{el}$ and $\Delta\epsilon_M$ are the electronic and Mössbauer contributions to the dielectric constant. The quantity $\Delta\epsilon_M$ deriving from the Mössbauer interaction depends in a resonance manner on the frequency, and its real part changes sign at the resonance frequency of the Mössbauer transition, thereby opening up the possibility for satisfying the PM condition (3). To obtain a quantitative description of the corresponding possibility, we employ expressions for $\Delta\epsilon_{el}$ and $\Delta\epsilon_M$. The expression for the electronic contribution is well known:

$$\Delta\epsilon_{el}=(\omega_p/\omega)^2, \tag{5}$$

where ω_p is the plasma frequency for the sample. The explicit form of $\Delta\epsilon_M$ depends on the characteristics of the Mössbauer transition (see, for example, Refs. 1 and 6) and will be presented below in the form

$$\Delta\epsilon_M=-f\Gamma_i N(E_S-E_R+i\Gamma/2)^{-1}, \tag{6}$$

where f is the Lamb–Mössbauer factor, Γ_i and Γ are the natural and total widths of the Mössbauer transition, N depends on the characteristics of the Mössbauer transition,[1] and E_S and E_R are the SR and resonance energy, respectively. Now it is easy to find k_p and k for all the specific cases listed above. For example, for the case of CIMS1, scattering from a nonresonant into a resonant component, one has

$$k_p=(\omega/c)(\epsilon_{el})^{-1/2}=(\omega/c)(1+\Delta\epsilon_{el}/2), \quad k=(\omega/c)(1-\Delta\epsilon_{el}/2+\Delta\epsilon_M/2), \tag{7}$$

and the PM condition (3) can be represented in the form

$$\mathrm{Re}(\Delta\epsilon_{el}+\Delta\epsilon_M/2)=0. \tag{8}$$

It follows from the form of $\Delta\epsilon_M$ (Ref. 1) that PM for case 1 can be achieved at a frequency close to and somewhat below the resonance frequency. If condition (8) holds, an expression for the sample thickness corresponding to maximum intensity of the resonant CIMS component can be found from Eq. (4):

$$h_m = (1/\mu_{Mp})\ln[(\mu_{Mp}+\mu_e)/\mu_e], \tag{9}$$

where μ_e is the absorption coefficient for SR (without the nuclear interaction) and μ_{Mp} is the absorption coefficient for the Mössbauer radiation (without the interaction with electrons) at a frequency satisfying PM.

It follows from Eq. (9) that in a typical situation the sample thickness h_m corresponding to the maximum of the resonant component of CIMS is greater than the absorption length $1/\mu_M$ (where μ_M is the value of the Mössbauer absorption coefficient at exact resonance). For this reason, it follows from Eq. (9) that in case 1 the penetrating power of the effectively resonant CIMS component is greater than that of the ordinary Mössbauer radiation, and the maximum of the intensity of this component is shifted to lower frequencies.

For case 3, PM requires that $\Delta\epsilon_{el}=0$, which cannot be satisfied exactly. For this reason, there exist beats and limits on the intensity as a function of sample thickness even if there is no absorption. Now the maximum intensity corresponds to the following thickness:

$$h_m = (1/\Delta k)\tan^{-1}(\Delta k/\mu_e), \tag{10}$$

where $\Delta k = (\omega/c)\mathrm{Re}(\Delta\epsilon_{el})$.

INTENSITY OF THE RESONANT COMPONENT OF CIMS

The expression for the absolute intensity of CIMS in a sample of finite thickness can be obtained from expression (4) by squaring its modulus and integrating over the SR frequencies. The corresponding range of integration around the Mössbauer resonance frequency is estimated as $2T_D$, where T_D is the Debye temperature of the sample. However, it is difficult to perform such an integration. For this reason, we shall estimate the intensity of the resonant component of the CIMS under the simple assumption that scattering occurs with the participation of phonons. We shall assume that the cross section σ_{ph} for such scattering does not depend on the phonon energy and is constant in an integration interval of $2T_D$ around the resonance frequency. Then, we obtain for the cross section for scattering into the resonant component with phonon participation

$$\sigma_{ph} = \sigma_0(\Gamma/2T_D)f(1-f), \tag{11}$$

where σ_0 is the maximum Mössbauer elastic scattering cross section. Since the typical value of the ratio $\Gamma/2T_D$ is very small (of the order of 10^{-6} for the case of Fe^{57}), the effect of this scattering channel on SR absorption in the sample is negligible.

On this basis, we obtain for the intensity I_r of the resonant component of CIMS generated under the phase-matching conditions (8) the following equation describing the variation of the intensity with sample thickness:

$$dI_r(x)/dx = f(\sigma_p/\sigma_0)(\mu_{ph})(\alpha+1)^{-1}I_s(x) - (\mu_{Mp}+\mu_e)I_r(x), \tag{12}$$

where σ_p is the Mössbauer absorption cross section at the phase-matching frequency, α is the internal conversion coefficient, $I_s(x)$ is the SR intensity as a function of penetration depth in the sample, and $(\mu_{ph})^{-1}$ is the SR absorption length with respect to nuclear absorption with phonon participation.

Since the CIMS intensity at the entrance surface of the sample equals zero, taking into account relation (11) for the cross sections of the process with and without phonon participation, we obtain from Eq. (12) the following expression for the thickness dependence of the spectral intensity of the resonant component of the CIMS integrated over the SR frequency:

$$I_r(x)_t=(\sigma_p/\sigma_0)f(1-f)(\alpha+1)^{-1}I_s(0)(1-\exp(-\mu_{Mp}x))\exp(-\mu_e x), \tag{13}$$

where $I_s(0)$ is the spectral density of the SR at the entrance surface of the sample.

The maximum of expression (13) is reached at a depth determined by relation (9). For this thickness of the sample, the ratio of the number of photons of the resonant component of CIMS in an energy interval of the order of Γ to the number of photons in the same energy interval in the initial SR beam is estimated as

$$N_r/N_{sM}=f(1-f)(\alpha+1)^{-1}. \tag{14}$$

According to Eq. (14), the maximum number of resonant phonons that can be obtained on account of the resonant component of CIMS is less than their number in the initial SR beam. However, the ratio of their number to the number of resonant photons that have penetrated through the sample can be much greater than 1:

$$N_r(x)/N_M(x)=f(1-f)(\alpha+1)^{-1}(1-\exp(-\mu_{Mp}x))\exp(-\mu_e x+\mu_M x). \tag{15}$$

The ratio of their number to the number of resonantly elastically scattered photons is estimated as

$$N_r(x)/N_{Ms}(x)=(1-f)f^{-1}(1-\exp(-\mu_{Mp}x))\exp(\mu_M x)/(1-\exp(-\mu_M x)), \tag{16}$$

where at thicknesses greater than $(\mu_M)^{-1}$ relation (16) approaches $(1-f)f^{-1}\exp(\mu_M x)$, i.e., it becomes exponentially large.

COMPUTATIONAL RESULTS

In the present section the results of the general analysis are illustrated by calculations for specific values of the parameters of the problem. The parameters employed in the calculations correspond approximately to the interaction of SR with a sample of iron highly enriched with ^{57}Fe. The corresponding Mössbauer transition energy equals 14.4 keV.

The following values of the other parameters were used in the calculations: $\mathrm{Re}(\Delta\epsilon_{el})=10^{-5}$, $\mathrm{Im}(\Delta\epsilon_{el})=2\times10^{-7}$, and $\mathrm{Max\ Re}(\Delta\epsilon_M)=10\ \mathrm{Re}(\Delta\epsilon_{el})$.

As was mentioned above, for the case of CIMS1 the closeness to the PM conditions (3) and (8) depends on the shift of the frequency relative to the Mössbauer resonance. Figure 1 displays curves of the amplitude of the resonant component of the CIMS versus the penetration depth of this component in the sample for several values of the deviation of the frequency from resonance.

Since the spectral distribution of the resonant component of CIMS changes as the component propagates in the sample, the spectral distributions of the resonant component of the CIMS at the exit surface are presented in Fig. 2 for samples of different thickness.

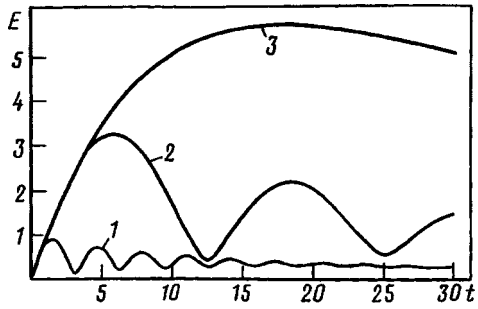

FIG. 1. Amplitude of the resonant component of CIMS (arbitrary units) versus the dimensionless sample thickness $t=h(\omega/c)\mathrm{Re}(\Delta\epsilon_{el})$ for different deviations of the frequency from resonance: curve *1* — $\Delta\omega/\Gamma=5$; curve *2* — $\Delta\omega/\Gamma=-10$; curve *3* — $\Delta\omega/\Gamma=-5$ — a frequency satisfying the PM conditions.

Figure 3 makes it possible to compare the ordinary decay of the intensity of Mössbauer radiation in the sample with the behavior of the amplitudes of different components of CIMS.

DISCUSSION OF THE RESULTS

As the results of our analysis show, forward CIMS exhibits many characteristic features, the most pronounced of which are an effective increase in the penetrating power of the resonant component of the CIMS and a shift of its spectral distribution to below the resonance frequency. The amplitude of forward CIMS for frequencies close to PM would increase linearly with sample thickness if there were no nonresonant absorption. However, since nonresonant absorption is present, this linear growth is limited by the electron absorption length $1/\mu_e$. The physics of the increase in the penetrating power of the resonant component of CIMS is related with the pumping of the nonresonant component of the SR into the resonant component.

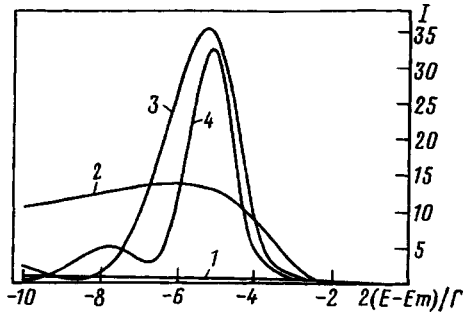

FIG. 2. Spectral distribution (arbitrary units) of the intensity of the resonant component of CIMS versus dimensionless sample thickness $t=h(\omega/c)\mathrm{Re}(\Delta\epsilon_{el})$: curve *1* — $t=1$; curve *2* — $t=5$; curve *3* — $t=15$; curve *4* — $t=25$.

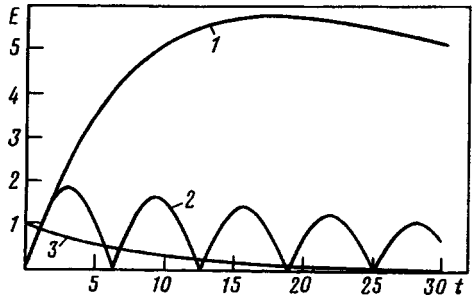

FIG. 3. Amplitude of the resonant component of CIMS (arbitrary units) (curve *1*), nonresonant component of CIMS (2), and ordinary Mössbauer radiation incident on the sample (3) versus the dimensionless sample thickness $t=h(\omega/c)\mathrm{Re}(\Delta\epsilon_{ei})$ (curves *1* and *3* pertain to the same frequency $\Delta\omega/\Gamma=-5$, which satisfies the PM conditions).

The nonresonant component of CIMS undergoes beats as a function of sample thickness, and it reaches its maximum value when the thickness equals the corresponding coherence length. On the whole, however, the nonresonant components of CIMS are smeared over an energy of the order of $2T_D$, and their spectral density is much lower than the corresponding spectral density in the initial SR beam.

There are several possibilities for observing experimentally the above-discussed properties of forward CIMS. An increase in the penetrating power of the resonant component of the CIMS can be observed directly by observing forward CIMS for samples whose thickness is greater than the Mössbauer absorption length $1/\mu_M$. The transformation of the spectral distribution of the resonant component of CIMS with sample thickness can be observed by the traditional Mössbauer spectroscopy combined with the time-delay technique. An obvious way of changing the effective sample thickness is to change the angle of incidence of the beam.

This work was supported by Russian Fund for Fundamental Research Grant No. 96-02-18812 and a Grant from the Russian State Science Program ''Fundamental Metrology in the Synchrotron Radiation Project.''

[a)]e-mail: bel@landau.ac.ru

[1] V. A. Belyakov, *Diffraction Optics of Complex-Structured Periodic Media*, Springer, New York, 1992, Chaper 10, p. 333, supplemented translation of the Russian edition [Russian original, Nauka, Moscow, 1988].
[2] M. Seto, Y. Yoda, S. Kikuta *et al.*, Phys. Rev. Lett. **74**, 3828 (1995).
[3] X. W. Zhang, Y. Yoda, M. Seto *et al.*, Jpn. J. Appl. Phys. **34**, L330 (1995).
[4] A. I. Chumakov, A. Q. R. Baron, R. Rüffer *et al.*, Phys. Rev. Lett. **76**, 4258 (1996); A. I. Chumakov, R. Rüffer, A. Q. R. Baron *et al.*, Phys. Rev. B **54**, R9596 (1996).
[5] J. B. Hastings, D. P. Ṣiddons, U. van Bürck *et al.*, Phys. Rev. Lett. **66**, 770 (1991).
[6] V. A. Belyakov, Zh. Éksp. Teor. Fiz. **108**, 741 (1995) [JETP **81**, 405 (1995)].

Translated by M. E. Alferieff

Interaction of Anderson impurities with high orbital angular momenta: non-RKKY behavior and instability of Kondo lattice

A. S. Ioselevich

Landau Institute of Theoretical Physics, Russian Academy of Sciences, 117940 Moscow, Russia; Institut für Theoretische Physik, RWTH Aachen, D-52056 Aachen, Germany

(Submitted 10 December 1997)
Pis'ma Zh. Éksp. Teor. Fiz. **67**, No. 1, 76–81 (10 January 1998)

The hybridization-induced interaction of Anderson impurities with orbital angular momentum l is revisited. At short distances $R<R_c \propto (l+1)/k_F$ the interaction has antiferromagnetic sign and decays as $(R_c/R)^{4l}$. At larger distances $R>R_c$ the RKKY-like oscillatory interaction sets in. As l increases, the system will sooner or later enter the ''short-distance'' domain, where the intersite magnetic interaction dominates over the screening processes. This means that, contrary to previous expectations, the nonmagnetic state of the Anderson lattice is unstable at $l\to\infty$. © *1998 American Institute of Physics.* [S0021-3640(98)01501-1]

PACS numbers: 75.30.Mb

The steady interest of theorists in the Anderson lattice model[1] is due to a nontrivial nonmagnetic ground state (Kondo lattice), which is expected to occur in this model under certain conditions (see reviews[2,3]). Initially such a nonmagnetic state was viewed as a simple collection of basically independent Kondo ions, but it was quickly understood that the situation is not that simple. At any reasonable concentration of magnetic ions the Kondo clouds strongly overlap, so that the nonmagnetic state (if any) could only be a result of some sophisticated collective screening effect. A severe limitation on the nonmagnetic scenario[4] is imposed by the conduction-electron-mediated magnetic interaction of Anderson ions,[5–8] tending to form a magnetically ordered state. The magnetic interaction energy E_{mag} is proportional to the fourth order of the hybridization matrix element V, while the ''Kondo energy'' E_K, characteristic for screening processes, is exponentially small in $|V|^{-2}$. This means that a controlled theoretical analysis of the nonmagnetic state can only make sense if there is an additional parameter in the model, which can help to overcome the tendency to the magnetic order formation. It is widely believed now that the degree of ''orbital'' degeneracy N of the Anderson ion may be such a parameter. It was first argued by Coleman[9] and Read, Newns, and Doniach[10] that the screening processes can dominate over the intersite interaction for the Anderson ions with high $N\gg 1$. The nonmagnetic state itself was extensively studied both for the so-called $SU(N)$ Anderson lattice model[11,2] with unspecified external origin for the degeneracy, and for a more realistic model with genuine orbital degeneracy related to the orbital angular momentum l of a magnetic ion.[12,3] For the former model the energy E_{mag} of the competing magnetic state is easy to find, and the criterion of stability of the Kondo lattice can be

easily checked: it is indeed fulfilled at large N. For the latter model only tentative estimates of E_{mag} have been found (see Refs. 12,3,8); they also seemed to favor a nonmagnetic state. In Refs. 12 and 8, however, only the angular dependence of the matrix elements was taken into account, while, as we will see below, the dependence on $|\mathbf{k}|$ is of crucial importance for high angular momenta l.

The goal of this paper is: (i) to study the dependence of the effective magnetic interaction of Anderson ions on the distance between ions, and (ii) to reconsider the question of stability of the nonmagnetic state of the Anderson lattice at high degeneracy N.

A mechanism of indirect interaction of magnetic atoms, originating from the hybridization of localized and delocalized electrons was proposed in the pioneering paper[5] by Coqblin and Schrieffer (see also Ref. 6). This interaction is presumably essential (i.e., it can dominate over the conventional exchange-induced RKKY interaction[13]) in the resonant case, when the localized level ϵ_0 is situated only slightly below the Fermi level ϵ_F, which is supposedly the case for the metals with considerable valence fluctuations (e.g., cerium). The original derivation[5,6] of the interaction, based on the repeated application of the second order Schrieffer–Wolff transformation,[14] was, however, incomplete. A straightforward fourth-order Schrieffer–Wolff transformation (see Refs. 7,8), gives rise to, besides the RKKY-like (though highly anisotropic) Coqblin–Schrieffer interaction, an additional important term which is reminiscent of ordinary superexchange.[15] This term alters the interaction quite dramatically, especially at short distances, where it dominates and changes the sign of the interaction to antiferromagnetic.

In this letter we restrict consideration to the case of one electron in the magnetic shell (e.g., one f electron for cerium ions) and consider only the lower spin–orbital multiplet, characterized by the total angular momentum $J=l-1/2$ or $l+1/2$, the degeneracy of the localized state being $N=2J+1$. We describe a system of two magnetic ions (a and b) by the Anderson Hamiltonian $\mathcal{H}=\mathcal{H}_0+\mathcal{H}_{hyb}$, where

$$\mathcal{H}_0=\sum_{\mathbf{k}\sigma}\epsilon_{\mathbf{k}}c^{\dagger}_{\mathbf{k}\sigma}c_{\mathbf{k}\sigma}+\epsilon_0\sum_{M,i=a,b}n_{iM}+\frac{U}{2}\sum_{i,M\neq M'}n_{iM}n_{iM'},$$

U is the energy of the Hubbard repulsion (we set $U=+\infty$ for simplicity); $n_{iM}=f^{\dagger}_{iM}f_{iM}$, $f^{\dagger}_{iM}$ creates an electron with $J_z=M$ in the unclosed shell of the ith magnetic ion; $c^{\dagger}_{\mathbf{k}\sigma}$ creates a conduction electron with momentum $\mathbf{k}$ and spin projection $\sigma=\pm 1/2$. The hybridization Hamiltonian is

$$\mathcal{H}_{hyb}=\sum_{i\mathbf{k}M\sigma}e^{i\mathbf{k}R_i}V_M(\mathbf{k}\sigma)c^{\dagger}_{\mathbf{k}\sigma}f_{iM}+\text{ h.c.}$$

The initial Hamiltonian $\mathcal{H}$ can be reduced to an effective interaction $\hat{H}$ of magnetic moments, by means of a fourth-order Schrieffer–Wolff transformation (see Ref. 8). Consider degenerate ground states of the unperturbed Hamiltonian $\mathcal{H}_0$, characterized by quantum numbers $\nu\equiv\{M_a,M_b\}$. Then, specifying all possible intermediate states $|i\rangle$, we obtain composite fourth-order matrix elements between states $|\nu\rangle$ and $|\nu'\rangle$:

$$\hat{H}=\sum_{i_1 i_2 i_3 \neq \nu,\nu'} \frac{\langle \nu'|\mathcal{H}_{hyb}|i_3\rangle\langle i_3|\mathcal{H}_{hyb}|i_2\rangle\langle i_2|\mathcal{H}_{hyb}|i_1\rangle\langle i_1|\mathcal{H}_{hyb}|\nu\rangle}{(E_\nu - E_{i_3})(E_\nu - E_{i_2})(E_\nu - E_{i_1})}$$

$$= -\sum_{\mathbf{k}\mathbf{k}'\sigma\sigma'} \hat{\Phi} \frac{\theta(\epsilon_{\mathbf{k}}-\epsilon_F)}{(\epsilon_{\mathbf{k}}-\epsilon_{\mathbf{k}'})(\epsilon_{\mathbf{k}}-\epsilon_0)^2}, \tag{1}$$

$$\Phi^{M'_a M'_b}_{M_a M_b} \equiv \cos\{(\mathbf{k}-\mathbf{k}')\mathbf{R}\}\{V_{M'_a}(\mathbf{k}'\sigma')V^*_{M_a}(\mathbf{k}\sigma)V_{M'_b}(\mathbf{k}\sigma)V^*_{M_b}(\mathbf{k}'\sigma') + (a \leftrightarrow b)\}.$$

Note that expression (1) comprises both usual RKKY-like indirect exchange processes with electron–hole excitation in the intermediate state ($k > k_F$, $k' < k_F$), and the superexchange-like processes with two-electron excitations in the intermediate state ($k, k' > k_F$).

In order to proceed with the calculation of the matrix elements $\hat{H}$ described by the general formula (1), we adopt the ''free electron'' model (see Ref. 3), in which the conduction electrons are described by plane waves, and $\epsilon_{\mathbf{k}} = k^2/2m$. Having in mind an application to rare earths, we assume that the spatial size of the localized state r_0 is small (see Ref. 16), much less than both R and k_F^{-1}, so that only the contributions of leading order in kr_0 should be kept. Then the matrix elements of the hybridization Hamiltonian are

$$V_M(\mathbf{k}\sigma) = C^{lJ}_{M\sigma} \int d^3\mathbf{r}\psi^*_l(r) Y^*_{lM-\sigma}(\Omega_{\mathbf{r}}) V(r) e^{i\mathbf{kr}},$$

$$C^{lJ}_{M\sigma} = \frac{1}{\sqrt{2}}\left(1 + \frac{4(J-l)\sigma M}{l+1/2}\right)^{1/2},$$

where $V(r)$ is the hybridization potential, which is spherically symmetric at the relevant small distances $r \sim r_0$, and $\psi_l(r)$ is the radial part of the localized wave function. Performing the angular integration, we get at $kr_0 \ll 1$

$$V_M(\mathbf{k},\sigma) = C^{lJ}_{M\sigma}(k/k_F)^l V_{k_F} \sqrt{4\pi} Y^*_{lM-\sigma}(\Omega_k), \tag{2}$$

where $V_{k_F} \propto (k_F r_0)^l$ is a constant. The factor $(kr_0)^l$, very important in the case of high l, arises due to tunneling under the centrifugal barrier. Choosing the quantization axis parallel to $\mathbf{R}$, we can now rewrite (1) in a form

$$\hat{H} = -\frac{2}{\pi}\hat{P} I_0 \int_{k_F}^{\infty} g_{JM_a}(kR) \frac{(k/k_F)^{2l} k^2 dk}{(k^2 - 2m\epsilon_0)^2}$$

$$\times \mathcal{P}\int_0^{\infty} g_{JM_b}(k'R) \frac{(k'/k_F)^{2l} k'^2 dk'}{(k^2 - k'^2)} + (a \leftrightarrow b), \tag{3}$$

where $I_0 = |V_{k_F}|^4 (m/\pi)^3$, the symbol $\mathcal{P}$ means the principal value of the integral, and $\hat{P} \equiv \delta_{M'_a M_b}\delta_{M'_b M_a}$ is the ''exchange operator.'' The real function

$$g_{JM}(x)=\sum_{\sigma}\,(C^{lJ}_{M\sigma})^2\int d\Omega|Y_{lM-\sigma}(\Omega)|^2\cos(x\,\cos\,\theta),$$

depends only on J and $|M|$, not on l, and not on the sign of M. It is convenient to represent $g_{JM}(x)$ as the real part of a complex function $\tilde{g}_{JM}(x)$ with appropriate analytical behavior

$$\tilde{g}_{JM}(x)=-\frac{(J-|M|)!}{(J+|M|)!}\int_1^{\infty}\{(J+|M|)^2|P^{|M|-\frac{1}{2}}_{J-\frac{1}{2}}(t)|^2+|P^{|M|+\frac{1}{2}}_{J-\frac{1}{2}}(t)|^2dte^{it(x+i0)},$$

where P^m_n are associated Legendre polynomials. For the nondegenerate Anderson model ($J=1/2$) one gets $\tilde{g}_{\frac{1}{2}\frac{1}{2}}(x)=e^{ix}/ix$. In general, $\tilde{g}_{JM}(x)=e^{ix}Q_{JM}(1/x)$, where Q_{JM} are polynomials of degree $2J$. Their explicit form for not very high J (e.g., for $J=5/2$ in case of cerium) can be easily found using a program of analytical calculations. The study of properties of $\tilde{g}$ for general J,M is a quite involved mathematical exercise; here we give only a few asymptotic forms without derivation:

$$\tilde{g}_{JM}(x)\approx\frac{B_{JM}e^{ix}}{(ix)^{|M|+1/2}},\quad B_{JM}=\frac{(J+|M|)!}{2^{|M|-1/2}(|M|-1/2)!(J-|M|)!},\quad \text{for } x\gg J, \tag{4}$$

$$\tilde{g}_{JM}(x)\approx J_0[x\sqrt{1-(M/J)^2}]-i\frac{A_{JM}}{x^{2J}}\exp\left(\frac{D_{JM}x^2}{8J}\right), \tag{5}$$

for $x\ll J$, where J_0 is a standard Bessel function, and

$$A_{JM}=\frac{(-1)^{J+M}M(2J)![(2J)!!]^2}{2J^2(J-M)!(J+M)!},\qquad D_{JM}=\frac{J(J-2)+M^2}{(J-1)^2}.$$

Comparison of the asymptotic forms (4) and (5) shows that they match at $x\sim J$ for all values of M and J.

Since $\tilde{g}_{JM}(x)$ is an analytic function in the upper half plane, one can perform the integration over k' in Eq. (3) by the residue theorem; introducing the dimensionless variable $z=kR$, we arrive at

$$\hat{H}=-\frac{\hat{P}I_0}{(k_FR)^{4l}}\,\mathrm{Im}\int_{k_FR}^{\infty}\frac{z^{4l+3}dz}{(z^2-2m\epsilon_0R^2)^2}\,\tilde{g}_{JM_a}(z)\tilde{g}_{JM_b}(z). \tag{6}$$

Let us start the discussion with the case of the nondegenerate Anderson model: $l=0$, $J=1/2$, where the interaction is isotropic: $\hat{H}=(\mathbf{J}^{(a)}\cdot\mathbf{J}^{(b)})I(R)$. In the nonresonant case (when ϵ_0 is not especially close to ϵ_F) there is only one spatial scale, viz., $R_c\sim\pi/k_F$, and the ''exchange constant'' $I(R)$ has the following asymptotic behavior for $R\ll R_c$:

$$I(R)=\frac{I_0}{k_FR}\left\{\frac{1}{\sqrt{\varepsilon}}\ln\frac{1+\sqrt{\varepsilon}}{1-\sqrt{\varepsilon}}+\frac{2}{1-\varepsilon}\right\}>0,$$

where $\varepsilon = \epsilon_0/\epsilon_F$. This asymptotic behavior is dominated by the antiferromagnetic contribution of the superexchange processes. For $R \gg R_c$ we get $I = I_0(\epsilon_F/\Delta)^2(k_F R)^{-3} \times \cos 2k_F R$, which coincides with the asymptotic behavior of the conventional RKKY interaction.

In the resonant case, when $\Delta \equiv \epsilon_F - \epsilon_0 \ll \epsilon_F$, the main contribution to the interaction comes from a narrow strip of width $< \Delta$ above the Fermi surface. As a consequence, a new spatial scale $R_{\text{res}} = \epsilon_F/k_F\Delta \gg R_c$, and a new intermediate asymptotic form $I = I_0(\epsilon_F/\Delta)(k_F R)^{-2}\sin 2k_F R$, valid in the range $R_c \ll r \ll R_{\text{res}}$, arises. This asymptotic form has a shifted phase of oscillations and a slower decay of the amplitude in comparison to the RKKY behavior.

Let us now discuss the general case: $l > 0$, $J > 1/2$. It can be shown that, at ''short'' distances $k_F R \ll J$, the main contribution to (6) comes from the residues of the integrand, so that

$$\hat{H} = A_{JM_a} A_{JM_b} \frac{\pi I_0 \Lambda \hat{P}}{(k_F R)^{4l}} \exp\left\{ \frac{m\epsilon_0 R^2}{4J} (D_{JM_a} + D_{JM_b}) \right\}, \tag{7}$$

where $\Lambda = 2mR^2\epsilon_0$ for $J = l - 1/2$ and $\Lambda = (D_{JM_a} + D_{JM_b})/16J$ for $J = l + 1/2$. Note that the interaction does not start to oscillate at $R \sim \pi/k_F$, as in the conventional RKKY interaction, but decreases monotonically, without changing its (antiferromagnetic) sign, up to $R \sim R_c \sim J/k_F$.

The physical interpretation of this result is as follows: The main contribution to the interaction comes from electrons which pass by the magnetic ions with impact parameters $\rho_a \sim \rho_b \sim R$. On the other hand, these electrons should have angular momentum l, and therefore their momenta $k \sim k^* = l/R$. The composite matrix element $\hat{H} \propto |V(k^*)|^4 \sim (l/k_F R)^{4l}$, which explains the principal features of (7). Note that for short distances, when $k^* \gg k_F$, the only processes in which both electrons involved may have such high momenta are the superexchange processes. Note also that the position of the Fermi level does not appear in expression (7). For large distances ($k_F R \gg J$), all factors in the integrand of (6), except the oscillating ones, can be replaced by their value at $z = k_F R$. Then, using (4), we get

$$\hat{H} \approx -\hat{P}\left(\frac{\epsilon_F}{\Delta}\right)^2 \frac{I_0 B_{JM_a} B_{JM_b}}{2(k_F R)^{|M_a|+|M_b|+2}} \sin\left(2k_F R - \frac{\pi}{2}(|M_a| + |M_b|)\right). \tag{8}$$

For $|M_a| = |M_b| = 1/2$ it matches with the result of Ref. 6.

In the resonant situation we obtain, as in the nondegenerate case, an additional intermediate asymptotic form: $\hat{H} \propto \text{Im}\{\tilde{g}_{JM_a}(k_F R)\tilde{g}_{JM_b}(k_F R)\}$. In particular, at $R_c \ll R \ll R_{\text{res}}$ it leads to a phase shift of $\pi/2$ and to an additional factor $(k_F R)\Delta/\epsilon_F$ in the amplitude of oscillations, exactly as in the nondegenerate case.

At moderate distances the spatial form of interaction differs considerably from the RKKY form even in the nonresonant case, though in the resonant case the difference is, of course, stronger. We have calculated the largest matrix element of interaction, $H^{1/2,\,1/2}_{1/2,\,1/2}(x = 2k_F R)$, numerically for two systems: the nondegenerate Anderson model,

and f levels (cerium). The complete plots will be published elsewhere; here we only mention that the resulting dependences approach the standard one $F_{\mathrm{RKKY}}(x) = x^{-3}\cos x - x^{-4}\sin x$ only for $x > 15$ (for $l=0$) and for $x > 30$ (for $l=3$). In rare earths, however, typically $2k_F R \approx 10$ for nearest neighbors, and at these distances the spatial shape of the interaction is quite far from the RKKY form, even without resonance. Thus neither the long-distance asymptotic form (8) nor the simple RKKY function may be used for interpretation of experimental data on cerium compounds; the k—dependence of matrix elements is essential for all practically important distances. Note, that this k-dependence arises here already in the leading order in $kr_0 \ll 1$, contrary to the case of the standard exchange-induced RKKY interaction, where the k-dependence of matrix elements occurs only due to corrections of higher order in kr_0 (see Ref. 13).

There is an important message concerning the stability of the nonmagnetic Kondo-lattice state in the above results. Since $A_{JM} \sim (4l/e)^{4l}$ at large l (and small M), we can conclude from (7) that the energy (per site) in the magnetic state of a lattice of Anderson impurities is

$$E_{\mathrm{mag}} \propto -|V_{k_F}|^4 (R_c/a_0)^{2N}, \quad R_c = 2N/ek_F, \tag{9}$$

provided that the distance between nearest neighbors $a_0 \ll R_c$. The energy of the non-magnetic (Kondo) state is $E_K \propto -\epsilon_F \exp(-\Delta/N\rho|V_{k_F}|^2)$, where ρ is the density of states at the Fermi surface.[9] Which energy is lower at high degeneracy $N \equiv 2l \to \infty$? To answer this question one rescales the parameters V_{k_F} and $k_F a_0$ so that E_K does not change with N, and then looks to see whether E_{mag}/E_K goes to zero or to infinity at $N \to \infty$. It was argued[12,3] that in order to get a proper nonmagnetic state, the rescaling should be done in such a way that both the effective coupling constant $N|V_{K_F}|^2/\Delta$ and the number of conduction electrons ''per subband per site'' $(k_F a_0)^3/N$ remain fixed. The latter means that R_c/a_0 scales as $N^{2/3}$ and, consequently, the condition $a_0 \ll R_c$ of the non-RKKY behavior is fulfilled at large N, so that one should indeed use Eq. (9) for E_{mag}. Then one obtains $E_{\mathrm{mag}}/E_K \propto N^{4N/3} \to \infty$, which means that the magnetic state, not the Kondo lattice, is preferable at large N, and the large-N Kondo-lattice scenario is inconsistent in a model in which the physical origin of the large N is the *orbital* degeneracy.

The author is indebted to H. Capellmann for discussions.

[1] P. W. Anderson, Phys. Rev. **124**, 41 (1961).
[2] A. C. Hewson, *The Kondo Problem to Heavy Fermions*, Cambridge University Press, 1993.
[3] D. M. Newns and N. Read, Adv. Phys. **36**, 799 (1987).
[4] R. Jullien, J. M. Fields, and S. Doniach, Phys. Rev. B **16**, 4889 (1977).
[5] B. Coqblin and J. R. Schrieffer, Phys. Rev. **185**, 847 (1969).
[6] R. Siemann and B. R. Cooper, Phys. Rev. Lett. **44**, 1015 (1980).
[7] J. M. Wills and B. R. Cooper, Phys. Rev. B **36**, 3809 (1987).
[8] L. C. Andreani and H. Beck, Phys. Rev. B **48**, 7322 (1993).
[9] P. Coleman, Phys. Rev. B **28**, 5255 (1983).
[10] N. Read, D. M. Newns, and S. Doniach, Phys. Rev. B **30**, 3841 (1984).
[11] A. J. Millis and P. A. Lee, Phys. Rev. B **35**, 3394 (1987).
[12] S. Doniach, Phys. Rev. B **35**, 1814 (1987).
[13] T. Kasuya, in *Magnetism*, edited by G. T. Rado and H. Suhl, Academic Press, New York, 1966, Vol. IIB, p. 215.

[14] J. R. Schrieffer and P. A. Wolff, Phys. Rev. **149**, 491 (1966).
[15] P. W. Anderson, in: *Magnetism*, Ed. G. T. Rado and H. Suhl, Academic Press, New York, 1963, vol. I, p.25.
[16] B. Coqblin, *The Electronic Structure of Rare-Earth Metals and Alloys*, Academic Press, New York, 1977.

Published in English in the original Russian journal. Edited by Steve Torstveit.

Does the phase transition exist in the one-component plasma model?

S. M. Stishov
Institute of High Pressure Physics, 142092 Troitsk, Moscow Region, Russia

(Submitted 25 November 1997)
Pis'ma Zh. Éksp. Teor. Fiz. **67**, No. 1, 82–85 (10 January 1997)

Explanations are given for why there is no real first-order phase transition in the one-component plasma (OCP) model. The fluid (liquid) and crystalline states of the OCP observed in computer experiments are not in equilibrium, on account of instability of the system. However, specific features of the free energy suggest that some sort of a ''virtual'' phase transition occurs in the model. Such a transition can be turned real by choosing the right form of the background energy. [S0021-3640(98)01601-6]

PACS numbers: 52.25.Kn

The purpose of this note is to clarify some subtle questions concerning the existence and properties of the phase transition in the so called one-component plasma (OCP) model. The OCP is a system of identical charged point particles, immersed in a homogeneous neutralizing background of opposite charge. The properties of the classical OCP can be described in terms of a single dimensionless parameter $\Gamma=(Ze)^2/r_sT$, where Ze is the charge of a particle, r_s is the radius of a sphere containing one particle, and T is the temperature. In the quantum case one more parameter, r_s or T, is needed to characterize the system.

The first indications of the existence of a crystalline phase in the quantum OCP model were obtained by Wigner in his classical paper devoted to correlation effects in an electron gas.[1] The terms ''Wigner solid'' and ''Wigner crystallization'' have become common in physics since that time. Later on, Brush, Sahlin, and Teller[2] in their pioneering Monte Carlo simulation of the OCP discovered that the radial distribution function $g(r)$ indicates the existence of crystalline structure in the classical OCP at $\Gamma>120$. Brush, Sahlin, and Teller were probably the first to use the term ''phase transition'' in discussing two states of the OCP: liquid and solid. Then Hansen[3] and Pollock and Hansen[4] carried out an extensive study of the OCP using an improved Monte Carlo technique, and again they observed existence of liquid and solid states in the OCP model and announced that the liquid–solid transition in the OCP model occurred at $\Gamma=155\pm10$. It should be emphasized here that by this time nobody doubted the existence of the phase transition in the OCP, and most of the subsequent papers have been devoted to determination of a more precise value of Γ_m, to quantum effects, etc. Current estimates of Γ_m are confined to the interval 172–178.[5] Quantum Monte Carlo simulations of the OCP should be mentioned here.[6,7] In general their results are considered to have confirmed the expectation of so-called ''cold'' melting in quantum Coulomb systems.[1,8] The result of the latest simulation data of this sort[7] is shown in Fig. 1. It would seem that

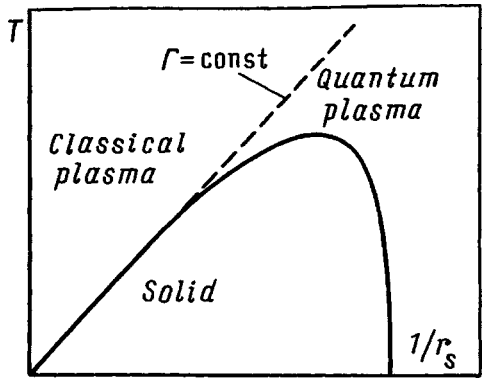

FIG. 1. The ''phase'' diagram of the OCP after Jones and Ceperly.[7] The condition $\Gamma = \text{const}$ corresponds to the classical ''transition.'' The strong deviation of the ''transition'' curve from the $\Gamma = \text{const}$ line at high density is a result of quantum effects. It follows from the numerical data[7] that $\lambda_T/L \approx 0.5$ at the maximum of the curve, where λ_T is the thermal de Broglie wavelength and L is the average interparticle distance.

all the OCP calculation and simulation data that have been obtained create very reliable grounds for discussing numerous problems of condensed matter physics connected in various ways with the existence of a solid and a liquid phase in the OCP. The state of the plasma in the interior of white dwarfs is one of the most intriguing problems.[8,9] But first we should have better understanding of what actually occurs in the OCP at the critical value Γ_m. Let's see how the numbers for Γ_m are being obtained. Normally all calculations in the OCP model are carried out in the canonical ensemble, and the natural output is the Helmholtz free energy F for various values of Γ. The intersection of two branches of the Helmholtz free energy is taken as the phase transition coordinate Γ_m (Fig. 2). Actually this procedure is incorrect: a phase transition occurs when the Gibbs free energies of two phases are equal, and one has to use the double-tangent construction in the

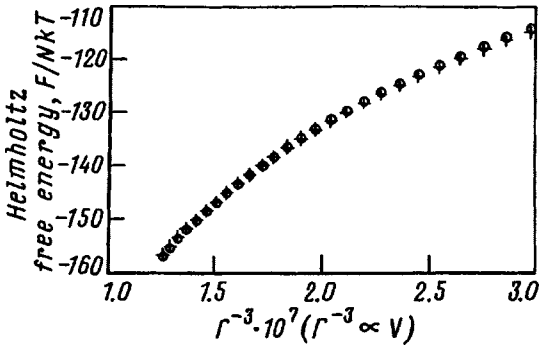

FIG. 2. The Helmholtz free energy F divided by NkT as a function of Γ^{-3} ($\Gamma^{-3} \propto V$) for the OCP, as follows from Monte Carlo calculations (H. E. DeWitt — private communication). V is the specific volume. The plot contains two systems of data which are almost on top of each other. The crosses and circles correspond to the fluid phase and solid phase, respectively. The intersection point occurs at $\Gamma \approx 175$ (H. E. DeWitt — private communication).

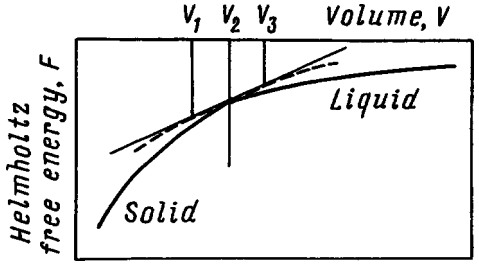

FIG. 3. An exaggerated version of the diagram of Fig. 2. It is seen that a correct double-tangent construction is impossible for convex potentials.

$F-V$ plane or an equivalent to get a correct result (Fig. 3). But usually it has been said that the volume change at the transition is too small to distinguish between the two procedures mentioned. Moreover, the subsequent claim that volume change at the liquid–solid transition in the OCP always equals zero eliminated any potential inquiry.[10]

Meanwhile, the fact that the double-tangent construction is wrong in principle in the case of the OCP was missed by a whole generation of researchers in the field. Figure 3, where the ''impossible'' double-tangent construction is depicted, illustrates the situation. The point is that the OCP is thermodynamically unstable at $\Gamma \geqslant 3$, and the pressure and compressibility of the system are negative (Figs. 2 and 3).[11] Due to the negative value of the compressibility the free energy F of the OCP is a convex function of the volume V, and hence a common tangent to two branches of the free energy does not make any sense. The conclusion is that there is not any kind of first-order phase transition in the system, at least for the reason that one of the necessary conditions, which is equality of pressure in coexisting phases, cannot be satisfied. So a question arises what does take place at the intersection point, where $F_{\rm liq}=F_{\rm sol}$ (see Figs. 2 and 3). A slope change is obvious at this point, and because $(\partial F/\partial V)_T=-p$, where p is the pressure, the liquid and solid at the intersection point have different pressures and cannot be in equilibrium. But for the reason that will be explained below, the intersection point under discussion may be called the point of a ''virtual'' phase transition. Note that the density is by definition unchanged at the intersection point, and the long discussion of this problem in Ref. 10 is senseless.

From the equality $F_{\rm liq}=F_{\rm sol}$ one can get an analog of the Clausius–Clapeyron equation in the form $dT/dV=\Delta P/\Delta S$, which describes behavior of the intersection point in the $T-V$ plane. This equation is applicable to the quantum case as well, where a temperature maximum is observed (Fig. 1). As follows from the above equation, the temperature maximum is reached when the pressure difference in the liquid and solid $\Delta P=0$, provided, of course, that one assumes that the corresponding entropy difference ΔS is finite at finite temperatures. This situation is illustrated by Fig. 4, where the temperature of the virtual phase transition as a function of pressure, which is of course negative, is shown in qualitative way.

It is obvious that the OCP model is not quite physical, but as was emphasized earlier, if one would think of the neutralizing background as a degenerate electron gas and would add the corresponding Fermi energy to the total energy of the system, then the situation would change drastically.[4] The pressure and the compressibility would become

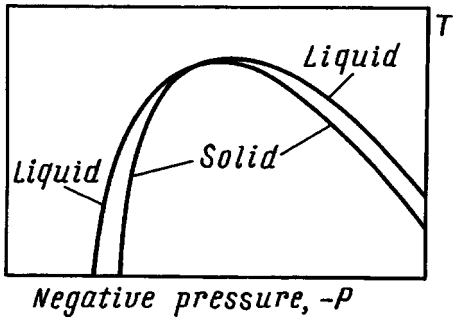

FIG. 4. The ''phase'' diagram of the OCP in the $P-T$ plane (compare with Fig. 1).

positive and the tangent construction would be feasible. That is why we may call the transition in the OCP a virtual phase transition. Figure 5 illustrates the transformation of the compression isotherm of the OCP with the quantum effects taken into account, when the Fermi energy of the background is added. However one should keep in mind that in the given case the role of the electronic background is restricted to charge neutralization, and Fig. 5b is drawn under the assumption that there is no other interaction between the point charges, which could be ions, and the electrons. We also assume that the quantum kinetic energy of the ions is not influenced by the nature of the background. As a result, the intersection points of the free energy curves do not change their volume coordinates (Fig. 5).

Both of the assumptions are valid in the high-density limit, which almost exactly corresponds to the interior of white dwarfs. However, the free energy difference of the

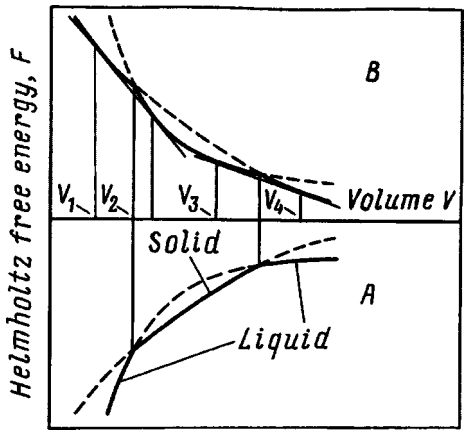

FIG. 5. The double crossing of free energy curves in case of strong quantum effects in the OCP model: a — standard OCP model (see Fig. 1), b — OCP model with a realistic background; the double-tangent constructions reveal two phase transitions with volume changes V_1-V_2 and V_3-V_4. The second, high-density crossing is due to the fact that the quantum contribution turns out to be structure-sensitive and increases the energy of the solid as compared to the liquid.

liquid and solid in the OCP is so small (see Fig. 2) that hardly any certain prediction about quantum (cold) melting at very high positive pressure can be made on the basis of OCP calculations that do not take into account the realistic structure of the background. In this connection it is instructive to refer to Refs. 12 and 13, where proofs were found that in case of metallic hydrogen the zero-point energy favors highly symmetrical structures in a certain density range. In other words, one may expect that the quantum effects not necessarily decrease the melting temperature of a Coulomb system on compression, and further and more-sophisticated studies are needed to reach a definite conclusion.

I acknowledge emphatically the discussions I had directly or indirectly with Hugh De Witt, David Kirzhnits, David Young, Francis Ree, Gilles Chabrier, Neil Ashcroft, and Efim Katz. I am specially thankful to Hugh De Witt for sending me some results of his calculations.

[1] E. Wigner, Phys. Rev. **46**, 1002 (1934).
[2] S. G. Brush, H. L. Sahlin, and E. Teller, J. Chem. Phys. **45**, 2102 (1966).
[3] J. P. Hansen, Phys. Rev. A **8**, 3096 (1973).
[4] E. L. Pollock and J. P. Hansen, Phys. Rev. A **8**, 3110 (1973).
[5] G. S. Stringfellow, H. E. DeWitt, and W. L. Slattery, Phys. Rev. A **41**, 1105 (1990).
[6] D. M. Ceperley and B. J. Alder, Phys. Rev. Lett. **45**, 566 (1980).
[7] M. D. Jones and D. M. Ceperly, Phys. Rev. Lett. **76**, 4572 (1996).
[8] D. A. Kirzhnits, Zh. Éksp. Teor. Fiz. **38**, 503 (1960) [Sov. Phys. JETP **11**, 365 (1960)].
[9] G. Chabrier, N. W. Ashcroft, and H. E. DeWitt, Nature (London) **360**, 48 (1992).
[10] J. D. Weeks, Phys. Rev. B **24**, 1530 (1981).
[11] M. Baus and J-P. Hansen, Phys. Rep. **59**, 1 (1980).
[12] D. M. Straus and N. W. Ashcroft, Phys. Rev. Lett. **38**, 415 (1976).
[13] V. Natoli, R. M. Martin, and D. M. Ceperly, Phys. Rev. Lett. **70**, 1952 (1993).

Published in English in the original Russian journal. Edited by Steve Torstveit.

Comment on the paper: Does the Unruh effect exist?

A. A. Grib
A. A. Friedman Theoretical Physics Laboratory, 191023 St. Petersburg, Russia

(Submitted 25 November 1997)
Pis'ma Zh. Éksp. Teor. Fiz. **67**, No. 1, 86–86 (10 January 1998)

[S0021-3640(98)01701-0]

PACS numbers: 03.70.+k, 04.60.−m

An article with the above title by V. A. Belinskiĭ, B. M. Karnakov, V. D. Mur, and N. B. Narozhnyĭ was published in a recent issue of JETP Letters.[1] The authors make the following assertion in the article: ''It is shown that quantization on the Fulling modes presupposes that the field vanishes on the spatial boundaries of the Rindler manifold. For this reason, Rindler space is physically unrelated with Minkowski space and the state of a Rindler observer cannot be described by the equilibrium density matrix with the Fulling-Unruh temperature. Therefore it is pointless to talk about the Unruh effect.'' Later in the text of the article (page 906) the authors talk about a boundary condition that ''corresponds to the presence of an impenetrable wall.'' I wish to make some brief remarks concerning these assertions.

The boundary conditions in the Unruh effect and their difference from the boundary conditions in the Casimir effect or in the problem of a mirror, where an ''impenetrable wall'' is actually present, have been analyzed by N. Sh. Urusova.[2] Urusova[2] noted that in the Unruh effect these boundary conditions are, as is well known,[3,4] conditions on the light cone (on the left half of the cone for the right-hand Rindler angle and vice versa for the left-hand angle), which in turn is a characteristic surface for the wave equation. A characteristic surface, by virtue of the definition of its properties (see, for example, Ref. 5), is not an ''impenetrable wall,'' and conditions on it do not violate the equation. I note, in passing, that the conditions (7) presented in Ref. 1 likewise are conditions on the light cone and not on a ''time-like surface,'' since there are no other conditions in the problem of the Unruh effect. Thus in my opinion the Unruh effect does exist and its generally accepted interpretation is correct, and the criticism in Ref. 1 is based on a misunderstanding.

[1] V. A. Belinskiĭ, B. M. Karnakov, V. D. Mur, and N. B. Narozhnyĭ, JETP Lett. **65**, 902 (1997).
[2] N. S. Urusova, ''Boundary conditions and the Unruh effect,'' Friedman Lab. Preprint FL040692 (1992).
[3] A. A. Grib, S. G. Mamaev, and A. M. Mostepanenko, *Vacuum Quantum Effects in Strong Fields* [in Russian], Énergoizdat, Moscow, 1988.
[4] V. N. Lukash and O. A. Kompaneets, Preprint IKI-570 [in Russian] (1981).
[5] V. I. Smirnov, *Higher Mathematics* [in Russian], Gostekhizdat, 1957, Vol. 4.

Translated by M. E. Alferieff

The authors reply

V. A. Belinskiĭ, B. M. Karnakov, V. D. Mur, and N. B. Narozhnyĭ

(Submitted 17 December 1997)
Pis'ma Zh. Éksp. Teor. Fiz. **67**, No. 1, 87–88 (10 January 1998)

[S0021-3640(98)01801-5]

PACS numbers: 03.70.+k, 04.60.−m

The boundary condition (7) of our paper[1] is not a condition on the light cone. To see this it is sufficient to glance at Eqs. (8) of that paper,[1] which relate the Minkowski and Rindler coordinates. It follows from these equations that the time axis in Rindler space ($\rho=0$, η finite and arbitrary) maps into a single point in Minkowski space, specifically, the origin of coordinates $t=z=0$.

The point $\rho=0$ is a boundary point in Rindler space for any Cauchy surface, for which one can take, for example, the ''space-like'' surface $\eta=$ const. In Minkowski space, to such a surface there corresponds a ray emanating from the origin of coordinates and lying outside the light cone. Light-cone surfaces in Minkowski space $z^2-t^2=0$, $z\neq 0$, $t>0$ (<0) correspond in Rindler space to the points $\rho=0$, $\eta=\pm\infty$, and the boundary conditions at these points are not important for our analysis.

As was shown in our paper,[1] the condition (7) arising at the apex of the light cone ensures that the operator $G(\rho)$ in Eq. (2) of Ref. 1 is self-adjoint (the case of a limit point[2]), as is required in order to solve the Cauchy problem by the Fourier method and therefore in quantizing the field (see Eq. (6) of Ref. 1). We shall clarify this assertion on a specific example.

The condition (7) for the quantized field $\phi_R(\rho,\eta)$ should be understood, strictly speaking, as an assertion concerning the matrix elements of this operator, for example, for the single-particle amplitude $\phi_f(\rho,\eta)=\langle 0_R|\phi_R(\rho,\eta)|f\rangle$, where $|f\rangle=c^+(f)|0_R\rangle$ and $c^+(f)=\int_0^\infty d\mu f(\mu)c_\mu^+$.

Let us examine the single-particle amplitude for which $\mathrm{Re}\phi_f(\rho,\eta)=m^{1/2}e^{-m\rho\cosh\eta}$. It satisfies the Klein–Fock–Gordon equation but it does not satisfy the boundary condition. The weight function f_μ, which is a Kontorovich–Lebedev transform of this amplitude, equals $f_\mu=2m^{1/2}/(\sinh\mu)^{1/2}$. Therefore $\int_0^\infty|f(\mu)|^2d\mu$ diverges at the lower limit, so that the single-particle state $|f\rangle$ is physically unrealizable. If, however, the boundary condition $\phi_f(0,\eta)=0$ is satisfied, then Parseval's equation[3] holds,

$$\int_0^\infty|\phi_f(\rho,\eta)|^2\frac{d\rho}{\rho}=\frac{1}{2}\int_0^\infty|f_\mu|^2\frac{d\mu}{\mu},\tag{1}$$

and the corresponding single-particle state is certainly normalizable.

Finally, following the logic of Sec. 12 of Ref. 4, we calculate the matrix element

$$\langle 0_M|c^+(f)c(f)|0_M\rangle = \int_0^\infty \frac{d\mu}{(e^{2\pi\mu}-1)}|f_\mu|^2. \tag{2}$$

If this matrix element is finite, then according to Eq. (1) the boundary condition $\phi_f(0,\eta)=0$ should be satisfied. This means that Rindler and Minkowski spaces are in no way physically related, so that the calculation of the matrix element in Eq. (2) is meaningless. The latter assertion is a central point of our paper[1] and justifies its title and results.

[1] V. A. Belinskiĭ, B. M. Karnakov, V. D. Mur, and N. B. Narozhnyĭ, JETP Lett. **65**, 902 (1997).
[2] V. A. Ditkin and A. P. Prudnikov, *Integral Transforms and Operational Calculus* [in Russian], FM, Moscow, 1961.
[3] R. D. Richtmyer, *Principles of Advanced Mathematical Physics*, Springer-Verlag, New York, c1978–1981 [Russian translation, Mir, Moscow, 1982].
[4] A. A. Grib. S. G. Mamaev, and V. M. Mostepanenko, *Vacuum Quantum Effects in Strong Fields* [in Russian], Énergoatomizdat, Moscow, 1988.

Translated by M. E. Alferieff